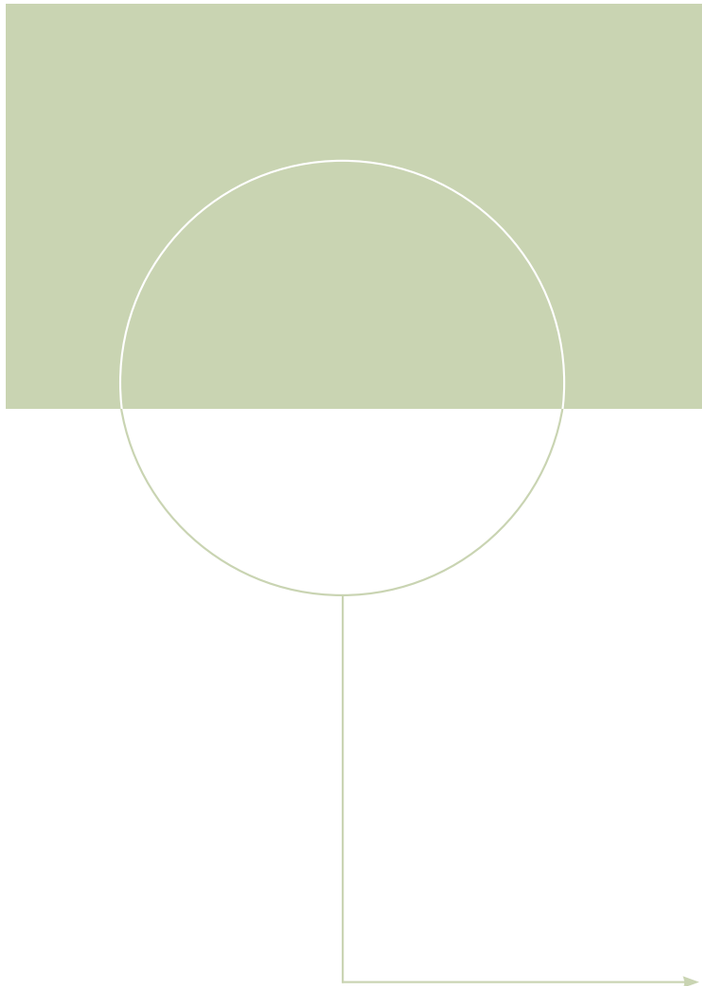

Master's thesis

2021

Ida Seip Gundersen

NTNU
Norwegian University of
Science and Technology
Faculty of Engineering
Department of Energy and Process Engineering

Ida Seip Gundersen

Optimisation of inversion methods for near-surface current measurements in regions with strong horizontal shear

February 2021

NTNU
Norwegian University of
Science and Technology

NTNU
Norwegian University of
Science and Technology

NTNU
Norwegian University of
Science and Technology

Optimisation of inversion methods for near-surface current measurements in regions with strong horizontal shear

Ida Seip Gundersen

Energy and Environmental Engineering
Submission date: February 2021
Supervisor: Simen Andreas Ådnøy Ellingsen
Co-supervisor: Benjamin Keeler Smeltzer

Norwegian University of Science and Technology
Department of Energy and Process Engineering

Acknowledgements

This master thesis finalises the work of the M.Sc. programme Energy and Environmental Engineering at the Department of Energy and Process Engineering, Norwegian University of Science and Technology (NTNU). I would like to thank my supervisor, Professor Simen Andreas Ådnøy Ellingsen, for his guidance and for letting me be a part of his research group, it has inspired me greatly. I would also like to thank my co-supervisor Benjamin Keeler Smeltzer for invaluable help and guidance throughout this project.

I wish to thank my family and friends for their advice and support.

Ida Seip Gundersen
Trondheim, February 2021

abstract

Upper-ocean processes are one of the key factors in the climate system, and suitable methods for measuring currents in the upper part of the water column is needed to understand the patterns and driving forces. Current measurements using inversion methods enables the use of remote sensing and has the potential to map currents over multiple km^2. Inversion methods can measure either the surface current or a depth-dependent current profile. Velocities are derived by analysing the wave dispersion within defined spatial windows. The size and placement of these windows determine the horizontal and vertical resolution of the current profiles. The purpose of this thesis is to explore whether there is an optimal window size for capturing horizontal shear and vertical shear, and whether there is a window size that successfully captures both. Measurements of the wave surface were performed with Free Surface-Synthetic Schlieren and the current velocity calculated with three inversion methods. The Effective Depth Method derives a linear, depth-dependent velocity, the Polynomial Effective Depth Method derives a polynomial current profile and the last method derives the near-surface current velocity. Three options for window placement were explored and the calculated currents were evaluated with Particle Image Velocimetry used as truth measurement. The study shows that high horizontal resolution is achieved for small and closely spaced windows, whereas high vertical resolution and large depth-range is achieved by analysing the wave dispersion in large windows. A small range of window sizes that provided a good compromise between the needs of horizontal and vertical resolution was identified. For these window sizes both the surface and depth resolution could be derived with relatively low Root-Mean-Square errors. The results demonstrates how the window size and window spacing can be adjusted in regions of strong horizontal shear in order to optimise the horizontal and vertical accuracy.

sammendrag

Havprosessene som finner sted i sjiktet nær overflaten er en av nøkkelfaktorene i klimasystemet, og egnede metoder for å måle strømninger i den øvre delen av vannsøylen er nødvendig for å forstå mønstrer og drivkrefter. Bruk av inversjonsmetoder for å måle strømningshastighet gjør det mulig å bruke fjernmåling, og har potensial til å kartlegge strømninger over flere km^2. Inversjonsmetoder kan enten kan måle overflatehastighet eller en dybdeavhengig strømningsprofil. Hastigheter blir avledet ved å analysere bølgespredningen innenfor definerte romlige vinduer. Størrelsen og plasseringen av disse vinduene bestemmer den horisontale og vertikale oppløsningen til strømningsprofilene. Formålet med denne oppgaven er å undersøke om det finnes en optimal vindusstørrelse for å fange opp horisontalt skjær og vertikal skjær, og om det finnes en vindusstørrelse som lykkes i å fange opp begge deler. Målinger av bølgeoverflaten ble utført med Free Surface-Synthetic Schlieren og strømningshastigheten ble beregnet med tre inversjonsmetoder. Effective Depth Method gir en lineær, dybeavhengig strømningsprofil, Polynomial Effective Depth Method gir en polynomisk dybdeavhengig strømningsprofil og den siste metoden måler strømningshastigheten nær overflaten. Tre alternativer for vindusplassering ble undersøkt, og de beregnede strømningshastighetene ble evaluert opp mot hastighetsmålinger utført med Particle Image Velocimetry. Studien viser at høy horisontal oppløsning oppnås for små, tett plasserte vinduer, mens høy vertikal oppløsning og stort rekkevidde på dybden oppnås ved å analysere bølgedispersjonen i store vinduer. Det ble identifisert et lite utvalg av vindusstørrelser som ga et godt kompromiss mellom behovene til horisontal og vertikal oppløsning. For disse vindusstørrelsene kan både overflate- og dybdeoppløsningen utledes med relativt lave kvadratisk gjennomsnitts-feil. Resultatene viser hvordan vindusstørrelse og vindusavstand kan justeres i områder med sterkt horisontalt skjær for å optimalisere den horisontale og vertikale nøyaktigheten.

Contents

Abbreviations

3D Three Dimensional

ADCP Acoustic Doppler Current Profiler

CC Copter Currents

CFD Computational Fluid Dynamics

DIC Digital Image Correlation

EDM Effective Depth Method

FFT Fast Fourier Transform

FS-SS Free Surface-Synthetic Schlieren

HF High Frequency

NTNU Norwegian University of Science and Technology

PIV Particle Image Velocimetry

PEDM Polynomial Effective Depth Method

RMS Root-Mean-Square

SNR Signal-to-Noise Ratio

UAV Unmanned Aerial Vehicle

List of Tables

List of Figures

Chapter 1

Introduction

The ocean and the climate are inextricably linked, and upper-ocean processes are one of the key factors in climate change. A complex system of ocean currents circulates the water around the globe and influences the global weather patterns. Currents of warm water is transported from the tropics towards the poles, making the climate of the surrounding land masses warmer, and deep ocean currents of cold water is returned from the poles towards the warmer regions. As well as working as a mean of transportation of hot and cold water, the upper part of the ocean plays a major role in the transfer of heat, mass and momentum between the ocean and the atmosphere. The near-surface currents are responsible for the horizontal advection of pollution and nutriments that takes place at the ocean-air interface [Campana et al., 2017] and knowledge of the near-surface current is also relevant for practical applications such as operational safety on ships and material transport of oil spill and plastic waste [Ha, 1979]. To build understanding of the underlying mechanisms, patterns and driving forces of the ocean currents, suitable methods for measuring currents both at the upper and lower part of the water column is needed. Today's standard method of measuring currents, Acoustic Doppler Current Profiler (ADCP), yields good accuracy in the lower layers, but measures the current only in a single point and struggles to capture the currents in the upper few meters of the water column. Accurate measurements of the current in the upper layer is difficult due to the presence of wave-induced platform motions, surface gravity waves, air bubbles and other sources of noise [Lund et al., 2015]. To measure the surface velocity over a large area drifters can be used, but in areas of large horizontal current gradients a large number of drifters must be deployed to obtain statistically significant measures [Ha, 1979].

1.0.1 Motivation

An alternative way to measure surface-currents and current-profiles is to use inversion methods, which is based on the measurement of wave dispersion. By measuring changes in wave frequency due to dispersion it is possible to reconstruct the current velocity. The inversion methods enable the use of remote sensing such as radar or optical based detection and has the potential to measure large areas of multiple km^2 at a time. Remote sensing eliminates the negative effect of wave motion in the upper layer of the water column, and as waves are most sensitive to currents near the surface, wave-based measuring methods are a good supplement

to ADCP to fill the lack of data near the surface.

One of the first attempts at measuring near-surface current shear was done in the 70s by Stewart and Joy [1974]. They derived a relationship between current and the current induced change in the phase velocity of the wave which has set the basis for much of the later research in this area. Wave-based, remote sensing, measuring methods has been in use since the 70s to derive the surface velocity. As well as measuring surface velocity, inversion methods can also give detailed measurements of the depth dependent current-profile. The state-of-the-art inversion method dealing with depth-dependent velocities are called the Effective Depth Method (EDM) and is based on assigning effective depths to measured wave-number-dependent Doppler shift velocities. However, the development of full depth-profile inversion methods has been limited due to two main challenges. The first challenge is related to the validation of new methods. It has been difficult to obtain in situ measurements of the actual current profile, leading to a lack of truth-measurements to validate the methods. The second challenge is related to the algorithms solving the depth-dependent current velocity. The algorithms are typically dependent on parameters and assumptions which are not known *a priori*, mainly related to the functional form of the current profile [Smeltzer et al., 2019].

As a part of an ongoing research project on shear currents a new inversion method that reconstructs the depth-dependent current profile called the Polynomial Effective Depth Method (PEDM) has been developed by Smeltzer et al. [2019]. The method is based on the EDM, but where the EDM is limited by the second challenge of a need for a priori knowledge of the functional shape of the current profile, the PEDM is solely based on measured data and without any free parameters.

1.0.2 Goal

In areas of large horizontal current gradients, the surface velocity derived from inversion methods can be presented as a horizontal vector field. This is done by separately analysing the wave dispersion in several defined spatial windows in a sub-set of the entire domain. For each spatial window a single current vector is derived. The size of this sub-set window determines the resolution and accuracy of the results. For inversion methods that derive a depth-profile, such as the PEDM and EDM, the size of the spatial window also determines the depth-range the method can resolve. The choice of window size affects several parameters such as the horizontal resolution, sensitivity, depth-range, depth resolution and homogeneity within the window. The resolving of vertical current gradients requires resolution of longer wavelengths which means that a large spatial area needs to be analysed, whereas the horizontal current gradient requires a finer horizontal spatial resolution, i.e. smaller spatial areas should be analysed. With this in mind, this project aims to further explore the potential of the PEDM method with focus on resolving current velocities in areas of strong vertical and horizontal current gradients by adjusting the size and placement of the spatial window that is analysed. The PEDM is compared with two other inversion

methods; the EDM that resolves a linear depth current profile and the Copter Currents method that measures the near-surface velocity.

1.0.3 Research questions

Research Question 1 What is an optimal spatial window size and window placement for capturing horizontal surface current gradients?

Research Question 2 What is an optimal spatial window size for capturing vertical current gradients?

Research Question 3 Is there an optimal window size that will resolve both horizontal and vertical current gradients?

1.0.4 Research method

In order to investigate the outlined research question, experimental data from spatially inhomogeneous shear flow was analysed. The data set consists of Free Surface-Synthetic Schlieren measurements performed in the small wave-current laboratory in the Fluid Mechanics facility at NTNU. Measurements of flows with different horizontal and vertical shear were taken for four flow profiles, referred to as profiles a)-d).

The following three inversion methods for calculating the current velocity was compared and contrasted: the first, referred to as the Copter Currents method (CC method), assumes a uniform depth-profile of the current velocity. The second and third, the linear Effective Depth Method (EDM_{lin}) and the Polynomial Effective Depth Method both give a depth-dependent current velocity. All inversion methods were implemented into the same MATLAB toolbox, Copter Currents, that originally only solved the Copter Currents method. All inversion methods evaluated three different options of window placement and window numbers to best capture the surface current gradient, as well as investigating how the size of the windows affected the results within each option. The ability to capture the currents depth profile was also analysed with The Effective Depth Method and the Polynomial Effective Depth Method. The error statistics and validations of the methods was analysed using Particle Image Velocimetry as "truth" measurements.

1.0.5 Scope

This paper investigates shear flows with linear and curved vertical shear profiles which are flow types that EDM and PEDM are well suited for. The CC method on the other hand, is built on the assumption of a uniform depth profile, not taking vertical shear into account. There are other interesting aspects that could have been explored but are not in this paper, due to time constraints. Among these, the performance of the methods at different wave-conditions, with a uniform depth profile and at varying water depths.

1.0.6 Thesis structure

The paper is divided into seven chapters. Chapter 2 gives an overview of inversion methods and a brief summary of current research in this field. Chapter 3 describes the theory behind inversion methods; linear wave theory, wave dispersion, the linear Effective Depth Method and the Polynomial Effective Depth Method. Chapter 4 is the methodology describing the Free Surface-Schlieren method used to measure the wave surface and the Particle Image Velocimetry, as well as introducing the MATLAB toolbox that is used to carry out the inversion process. Chapter 5 outlines the experimental setup and the experiments and in chapter 6 the results of the experiments are presented and discussed. Chapter 7 contains the conclusion of this project as well as suggestions for further work in this area.

Chapter 2

Background

This chapter will give a brief overview of the steps involved in the inversion process, the development of inversion methods and the latest research in the area.

2.0.1 The inversion process

Inversion methods have been used for decades to infer the surface velocity. Inversion methods have also been used for resolving the depth-profile, but the research in this area is more limited. The inversion process consists of four steps, as seen in figure 2.1, and results is the current velocity. First, wave measurements are carried out in the time-space domain. Then, the wave-data is transformed into the wave spectrum domain with a 3D Fast Fourier Transform (FFT). Thirdly, Doppler shift velocities are derived from the wave spectrum. Finally, an inversion method is applied to the Doppler shift velocities resulting in the final surface velocity for the CC method and the depth current profile for EDM and PEDM. Most of the research in the area focuses on either the remote or optical based sensing techniques used for wave measurements in step 1 or on the inversion method that is applied in step 4.

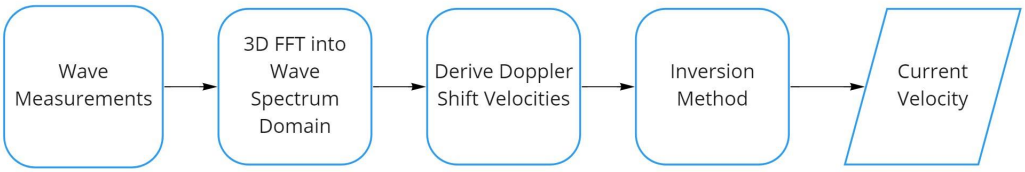

Figure 2.1: The four steps of the inversion process for inferring current velocities from surface wave measurements.

2.0.2 Challenges

Although wave-based current measurements offer several advantages compared to other current measurement methods, there are some challenges linked to these methods. One of the main challenges is the depth-dependence of the current

profile. Most of the inversion methods are based on an *a priori* assumption of the functional shape of the current depth profile. The shape of the current profile can be assumed to be uniform, such as in Horstmann et al. [2017*b*], and linear or logarithmic, as in the EDMs used by Stewart and Joy [1974], Ha [1979], Lund et al. [2015], and Teague et al. [2001]. In flows with varying vertical shear these assumptions of the functional form of the current profile does not always hold, causing the deduced current velocity to differ from the actual velocity. To be able to determine the current profile as a function of depth without any *a priori* assumptions one needs to measure waves over a wide range of wavelengths and directions [Smeltzer et al., 2019]. In a laboratory setting the spectrum of wavelengths can be controlled to a certain degree, but field measurements are dependent on the sea state to achieve good results [Campana et al., 2017]. The newly developed PEDM has been able to overcome this challenge by relying only on measured Doppler shift data and no user-input parameters or *a priori* functional shape assumptions. Another more fundamental problem with wave-based measuring methods is that current inferred from the wave dispersion measurements is not mathematically unique, there can be infinite possible solutions, making it an ill-posed inverse problem.

2.0.3 Wave-based measuring methods

In the first step the signal of the waves are measured in space and time. A spatial area is chosen and within this area the development of the wave dispersion is measured over a time period. There are several possible alternatives for remote or optical sensing of the surface waves. Inversion methods reconstruct the near-surface current from measured alterations of the wave frequency and require a signal that has the same periodicity in space and time as the wave signal. Both radar and optical based methods meet this requirement. The measuring method should ensure a signal with a high Signal-to-Noise ratio (SNR) in time and space. The choice of wave measurement method affects the range of wave numbers retrieved, hence it is important to choose a measuring method that covers a relevant range of wave numbers, has a suitable spatial resolution and covers an area of relevant size.

The majority of wave-based near-surface current measurements in the literature have used radar, which interact with the surface via Bragg scattering. The most common radar measurement method has been High frequency (HF) radar (e.g. Lund and Haus [2018], Ha [1979], [Teague et al., 2001] and Stewart and Joy [1974]), which covers oceanic wavelengths of 4 m and up [Rubio et al., 2017]. It has shown to yield good estimates of the average current in the top $\sim$ 1 m of the water column [Campana et al., 2017] and is suitable for use in coastal regions. In later years the use of X-band radar has become more common (e.g. Campana et al. [2017], Lund et al. [2015] and Young and Rosenthal [1985]). X-band radar is also best suited for use in coastal regions as the waves need to be at least two times longer than the radar ground resolution, leading to minimum wavelengths of $\sim$ 7.5 m [Horstmann et al., 2017*b*]. Optical methods such as polarimetric slope sensing has also been explored (e.g. Laxague et al. [2017*b*], Laxague et al. [2017*a*],

Zappa et al. [2008]). The polarimetric slope sensing is a single point passive image technique used to acquire short-scale wave structures and, as shown by Laxague et al. [2017*b*] and Zappa et al. [2008], it has great potential in near-surface current retrieval for waves with short wavelengths and short frequencies.

Varieties of the Schlieren method such as shadowgraph (e.g Horstmann et al. [2017*b*]) or Free Surface-Synthetic Schlieren (e.g. Smeltzer et al. [2019]) have also been used, but to a lesser extent. Shadowgraph is an optical method that reveals non-uniformities in a transparent medium like gas, water or glass due to the variation of fluid density or the reflection of light [Settles, 2001]. This is the method used by Horstmann et al. [2017*b*], [Horstmann et al., 2017*a*] in conjunction with the CC method to retrieve information of the surface from a video recorded by a Unmanned Aerial Vehicle (UAV). It shows great potential as a remote sensing technique to use in large-scale field work.

The Free Surface-Synthetic Schlieren method is the chosen method for the wave measurements used in this paper and it was also the chosen method by Smeltzer et al. [2019] when developing and validating the PEDM. The method measures the gradient component of the interface between two transparent fluids, e.g. water and air. A randomized dot pattern is placed either above or below the surface, and when waves pass over this pattern, they will affect the light refraction on the surface, which will appear as distortion of the dots. This distortion is in turn used to reconstruct the surface height matrix. The method was first introduced by Kurata et al (1990) and more recently it was outlined by Moisy et al. [2009]. The Free-Surface Synthetic Schlieren yields a high spatial resolution and gives good results in a small-scale setup such as in a lab- setting. It is however less suited on a larger scale due to the need to view the dot pattern through the free surface, and the fact that a too large distance between the dot pattern and the free surface will cause the distortion of the dots to be too large to analyse.

2.0.4 Inversion methods

Since Stewart and Joy [1974] presented their approximation of the relationship between currents and measured wave dispersion in 1974, much research has been done in this field. The varying spectral ranges of the wavenumber from the different wave detection methods presented above has led to the development of a number of inversion methods.

One of the earliest attempts to overcome the challenge with the assumption of the functional form of the current profiles was done by Ha [1979]. Ha developed a method for estimation based on an inversion of the relation found by Stewart and Joy [1974], but without the assumed shape of the current profile. The effective velocity measurements were taken using a unique HF radar system. HF radar measures the Doppler shift of the electromagnetic wave directly, measuring only one wavelength at the Bragg resonance. Information of the depth profile can be obtained by using multiple radar frequencies which probe different resonant wavenumbers. Ha used four different frequency waves to measure the effective

velocities, which was then used as input to the inversion. Because noise in the wave measurements gets amplified in the inversion process, the method yielded noisy current estimates.

Ha's method was further developed by Campana et al. [2016]. To overcome the problem with the small number of discrete wavenumbers from the HF radar and the corresponding noisy results, Campana used data from a X-band radar. Like the HF radar, X-band radar interacts with the surface via Bragg scattering. But where the HR measures only one wavelength, the X-band radar has the ability to image a broad range of wavelengths, giving wavenumber-dense data. Evaluating the many k-values reduces the noise in the inversion process and enable the use of inversion methods to estimate the current depth-dependence. Used in combination with a least square technique, the wavenumber data is used to invert for the current profile. This new method is capable of estimating the current with a similar error as other radar-based methods and it corresponded with the ADCP used as "truth" measurements. It is able to accurately depict depth variation in the current velocity, has twice the depth range compared to other radar based methods and does not require any *a priori* assumption of the shape of the current profile [Campana et al., 2017].

The PEDM is one of the newest additions to the inversion methods that aim to overcome the challenges related to the need for *a priori* knowledge of the functional shape of the current profile. It builds on the state-of-the-art EDM, but with a polynomial fit, rather than a linear or logarithmic one. The polynomial fit is based on the result from the wave-measurements. The method is based solely on experimental data and requires no user-input parameters or assumptions. The polynomial fit allows for better capture of the curvature of the current profile. The PEDM has been shown to be 3 times more accurate than the EDM for current profiles of significant curvature [Smeltzer et al., 2019].

While many of the newer inversion methods focus on reconstructing the depth-dependence of the flow, the most common and elementary methods determine a single current vector that is a representative of a weighted average of the near-surface flow. This method has been used by Horstmann et al. [2017*b*], Horstmann et al. [2017*a*] to determine the near-surface current velocity. Horstmann et al. [2017*a*] developed a MATLAB toolbox called Copter Currents that performed step 2-4 in the inversion process, with wave-measurements captured with a UAV used as input. From short video sequences of the water surface, characteristic parameters such as wavelengths, phase velocity and direction are quantified and analysed to find the current velocity. The inversion method used within the Copter Currents toolbox will in this paper be referred to as the CC method and the toolbox as a whole as Copter Currents. The combination of UAV and Shadowgraph makes it possible to cover a large area. The area can then be divided into smaller sub-sections where the waves are analysed separately, constructing a detailed surface current field. This has resulted in a wave measuring method that successfully covers a large area and an inversion method with a low computational cost.

The PEDM has currently only been tested in a small-scale lab setting with surface measurements carried out with Free Surface-Synthetic Schlieren, but the goal is to use the PEDM together with a wave-based measuring method that allows for the method to be applied on large-scale field work. The implementation of the PEDM into the Copter Currents toolbox is a step towards the testing of the PEDM on large-scale, real-field setting, utilizing the large spatial area that the UAV is able to cover by Horstmann et al. [2017*a*] in combination with an inversion method that derives the depth-dependence of the current.

Chapter 3

Theory

Parts of the theory in section 3.1 and 3.2 is reproduced from the author's project work, with minor alterations and additions.

This chapter aims to give an overview of the theoretical background of waves and dispersion before moving on to introduce the theory of inversion methods, the EDM and the PEDM. The significant features of frequency dispersion are retained in waves of infinitesimal amplitude, which means linear wave theory can be applied. In relation to water waves the term dispersion usually refers to the dispersion of frequency. In addition to the frequency dispersion water also exhibits amplitude dispersion, a non-linear effect where the phase velocity is different for waves of high and low amplitudes [Wu, 1963], but from this point on the term dispersion will refer to the dispersion of frequency.

3.1 Linear wave theory

The components of the waves can move with separate velocities. The two main velocities connected to waves are group velocity and phase velocity. For linear surface waves at constant depth, the phase velocity, which is the rate a given crest of the wave propagates in space is:

$$c(k) = c_0 = \frac{\omega}{k}, \tag{3.1}$$

where ω is the angular frequency and k is the wavenumber for a wavelength λ defined as

$$k = \frac{2\pi}{\lambda}. \tag{3.2}$$

A figure of the free water surface and the phase velocity can be seen in figure 3.2. The phase velocity is constant for a wave with a given frequency and wavenumber. Since the phase velocity is a function of the wavenumber, water waves are dispersive, causing the wave packets to disperse: spreading out and losing the original shape of the wave envelope as it moves, because wave components of different wavelengths move at different velocity.

The group velocity is a property of waves that have a defined envelope, measuring propagation through space of the overall shape of the wave envelope amplitude:

$$c_g = \frac{d\omega}{dk}. \tag{3.3}$$

If the medium is non-dispersive, the phase velocity will be constant and independent of k which will make the group velocity equal to the phase velocity. With a dispersive medium, like water, the phase velocity will differ from the group velocity, $c(k) \neq c_g$, which gives a non-linear relationship between ω and k. The relationship between the frequency and the wavenumber is called the dispersion relation.

3.2 Dispersion relation

In a dispersive medium the phase velocity of a wave is dependent on the frequency of the wave, as seen in Eq. 3.1. This means that wave components of different wavelength move at a different velocity. The waves can be expressed in terms of the angular wave frequency ω and the wavenumber k. These two are linked by the dispersion relation stating that waves of a given wavelength always have the same frequency. The dispersion relation varies depending on whether the water is deep, shallow or intermediate, the type of waves, and if there is a current present. Assuming negligible surface tension the dispersion relation for surface gravity waves in quiescent water of intermediate depth is:

$$\omega_0(k) = \sqrt{(gk \tanh{(kd)})}, \tag{3.4}$$

where g is the gravitational force and d the water depth.

Defining a still water surface to span the x-y-plane and the z-direction to denote the height, the wavenumber can be divided into two components, k_x and k_y. Within the 3D frequency-wavenumber domain the energy of the waves is located on the dispersion shell. The dispersion shell outlines the relationship between ω and k. Making a cut in the dispersion shell in the x-direction gives the the ω-k_x dispersion curve, the relationship between the angular frequency and the x-component of the wavenumber. An example on how the relationship between ω and k_x can look in quiescent water is shown in Figure 3.1. The black line is the dispersion curve, showing the non-linear relation between the wave frequency and the wavenumber in Eq. 3.4. The colour gradient represents the spectral power [dB], where the energy of the waves is centred, yellow colour denoting a high level of energy. From this figure one can see that the spectral power is concentrated with its peak in the dispersion curve.

The resolution of the $\omega - k$ domain is determined by the time-space signal of the measured wave. The resolutions of the frequency are defined by the length of the time signal used as input in the 3D FFT. A longer time signal increases the resolution of ω. The resolution of the wavenumber is defined by the size of the spatial area that is analysed. A large area results in high resolution of k, and a small area in low resolution of k. In addition to affecting the resolution, the size of the spatial area might also affect the range of ks. By increasing the area, waves of

longer lengths are observable. Corresponding small wavenumbers is seen in the $\omega - k$ domain, decreasing the width of the white line in the centre where there is no measured information of k. The resolution of ω and k impacts the quality and accuracy of the dispersion line.

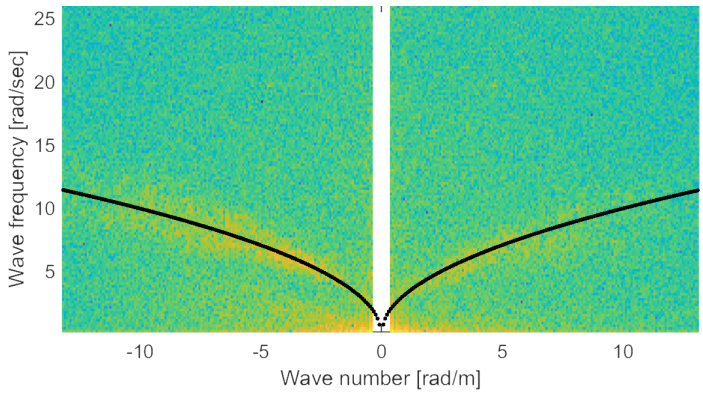

Figure 3.1: Example of a wavenumber-frequency plane retrieved from CC. The black line shows the dispersion relation for quiescent water of intermediate depth. Colour gradient is a spectral power log scale[dB].

If a uniform background current of velocity $U(z) = U_0$ is present it will lead to deviations from the phase velocity defined in Eq.3.1 due to a Doppler shift of the phase velocity. The frequency, ω, of the wave is shifted by an amount of $-kU_0$, and adding the shift to ω gives the frequency $\omega = \omega_0 + kU_0$. Inserting this into Eq. 3.1 gives the new phase velocity:

$$c(k) = \pm c_0 + U_0. \tag{3.5}$$

A current aligned with a waves propagation direction will increase the wave frequency, and the phase velocity becomes the sum of c_0 and U_0. A current in the opposite direction of the propagation direction will decrease the wave frequency and it is the difference between c_0 and U_0 that is observed in 3.5 [Laxague et al., 2017*b*][Ha, 1979]. If the background current varies with depth, U=$U(z)$, as seen in figure 3.2, the phase velocity becomes:

$$c(k) = \pm c_0 + \tilde{\mathbf{c}}(k), \tag{3.6}$$

where $\tilde{\mathbf{c}}(k)$ is the wavenumber dependent Doppler shift velocity. In the presence of a current the dispersion relation for a small-amplitude, linear wave in depth-varying flow can be approximated by:

$$\omega_{DR}(\mathbf{k}) = \omega_0(k) + \mathbf{k} \cdot \tilde{\mathbf{c}}(k) = \omega_0 + \Delta\omega, \tag{3.7}$$

where ω_{DR} is the wave frequency, ω_0 the frequency in quiescent water, $\mathbf{k} = \{k_x, k_y\}$ is the wave-vector, and $k = |\mathbf{k}|$. The second term in Eq. 3.7 takes into account the wave-shear current interaction that occurs in the presence of a depth varying current. The wavenumber dependent Doppler shift velocity, $\tilde{\mathbf{c}}(k)$, is the variation

in the phase velocity of the wave due to the background current. The Doppler shift velocity can be separated into two components:

$$\tilde{\mathbf{c}}(k) = \hat{\mathbf{u}}(k) + \mathbf{u_{sf}}(\mathbf{k}) \tag{3.8}$$

Where $\hat{\mathbf{u}}(k)$ is the effective velocity representing the weighted depth-averaged effect of Eulerian currents, and $\mathbf{u_{sf}}(\mathbf{k})$ is a wave induced current called the filtered Stokes drift. The filtered stokes drift is a non-linear wave interaction correction due to a non-linear correction term to the linear phase velocity [Lund et al., 2015],[Campana et al., 2017]. In the ocean the effective velocity is a combination of tidal currents, pressure-driven currents, inertia motion and wind drift.

The magnitude of the Doppler shift is the last term of 3.7, and inserting for $\tilde{\mathbf{c}}(k)$ the Doppler shift magnitude is give by:

$$\Delta\omega = \mathbf{k} \cdot \tilde{\mathbf{c}}(k) = \mathbf{k} \cdot [\hat{\mathbf{u}}(k) + \mathbf{u_{sf}}(\mathbf{k})]. \tag{3.9}$$

If the current profile is assumed uniform over the depth, the Doppler shift velocity reduces to the velocity of encounter $\mathbf{u}$, and Eq.(3.7) reduces to:

$$\omega_{\mathbf{DR}}(k) = \omega_0(k) + \mathbf{k} \cdot \mathbf{u}. \tag{3.10}$$

The velocity of encounter is a two-dimensional, weighted depth-average Eulerian current vector with components $[U_x\ U_y]$. It is independent of the wavenumber k, and represents the mean current near the surface, giving a uniform current profile independent of depth for the upper layer of the water.

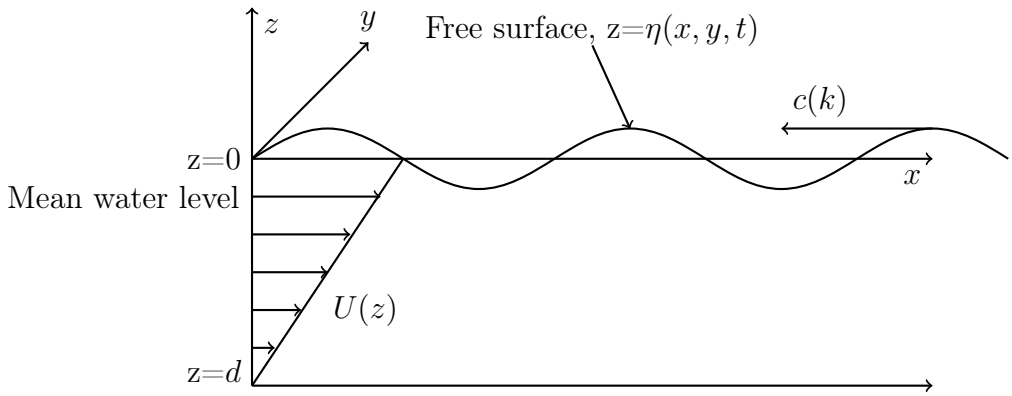

Figure 3.2: The free water surface with a wave of phase velocity $c(k)$ propagating in the opposite direction of a linear current profile $U(z)$.

3.3 Inversion methods

Inversion methods derive the near-surface current by measuring alterations to the wave frequency. The most elementary methods determine a single current vector representing a weighted depth-average current velocity, whereas the more advanced methods such as the EDM and PEDM reconstruct a current dependent of the depth. Most of today's inversion methods utilize the relationship between current and the

current-induced change in wave frequency derived by Stewart and Joy [1974] to find the velocity profile of the current. Assuming deep water and a current velocity that is small compared to the phase velocity of the wave, Stewart and Joy showed that the Doppler shift velocity can be approximated as a weighted average of the depth dependent current profile $\mathbf{U}(z)$ as:

$$\tilde{\mathbf{c}}(k) = \frac{\Delta\omega}{\mathbf{k}} - \mathbf{u_{sf}}(\mathbf{k}) = 2k \int_{\infty}^{0} \mathbf{U}(z) e^{2kz} dz, \tag{3.11}$$

where $\mathbf{U}(z) = [U_x(z)\ U_y(z)]$, $z = 0$ is the undisturbed water surface and $z = -h$ is the bottom with $h > 0$. For this approximation deep water regime, $kh \geq \pi$, is assumed. For deep-water regime one can assume the waves to be independent of the bottom and that the bottom is placed at $-\infty$, $h = \infty$. $\mathbf{U}(z)$ is determined from a set of measured values of the Doppler shift $\tilde{\mathbf{c}}_i$=$\{\tilde{c}_{x,i}\ \ \tilde{c}_{y,i}\}$ at discrete wavenumbers k_i, extracted from experimental data. $Ux(z)$ is determined from $c_{x,i}$ and $Uy(z)$ is determined from $\tilde{c}_{y,i}$. From Eq. 3.11 it can be seen that the weighted term decays exponentially with the depth z, hence the shorter wavelengths are sensitive to currents near the surface, and longer wavelengths are sensitive to the currents in the deeper layer. A version of the approximation in Eq. 3.11 that can be applied at finite depths where the depth affects the waves was derived by Skop [1987] and extended by Kirby and Chen [1989].

In the case of a depth-uniform current where $\mathbf{U}(z)$ =$\mathbf{U}_0$, the effective velocity reduces to $\hat{\mathbf{u}}(k)$=$\mathbf{U}_0$ and the Doppler shift velocity, $\tilde{\mathbf{c}}$, reduces to the wavenumber independent velocity of encounter, $\mathbf{u}$ in both in Eq.3.11 and in the dispersion relation, Eq.3.10. To first order the filtered stokes drift equals zero, $\mathbf{u_{sf}}$=0, and the depth uniform current can therefore be estimated with a linear fit, as can be seen in the second term in Eq. 3.10 [Campana et al., 2017]. In the presence of vertical current shear, the linear fit results in a wavenumber-independent *bulk velocity*. This bulk velocity is a representation of the bulk effect underlying currents have on waves. Since the bulk velocity lacks information of the vertical shear, the current estimate this method provides is of first-order [Campana et al., 2017]. The lack of shear information is not always of importance, and this first-order estimate of the current velocity has been widely used together with different remote sensing techniques.

The inversion method used in Copter Currents is of the first type, assuming a uniform depth profile, and using the dispersion relation given in Eq. 3.10. The resulting current vector is the velocity of encounter, $\mathbf{u}$, that represents the near-surface current velocity. The EDM and the PEDM use the dispersion relation in Eq. 3.7 and give a depth dependent current profile by using measured values of $\tilde{\mathbf{c}}(k)$ to determine $\mathbf{U}(z)$ using Eq. 3.11.

3.3.1 Effective Depth Method

The Effective Depth Method has been widely used in the literature for estimating near-surface shear currents $\mathbf{U}(z)$ by measured Doppler shift data, $\tilde{\mathbf{c}}(k_i)$. It is based on an *a priori* assumption of the functional shape of the current profile, which is assumed to be either linear or logarithmic. By assuming a given functional form to

the current profile, effective depths, Z_{eff}, can be assigned to the measured Doppler shift velocities based on the wavenumber, $\tilde{c}_i$=U[Z_{eff}(k_i)]. Each Doppler shift velocity $\tilde{c}(k)$ from points extracted from the wave-spectra is equal to the current profile at some depth, and the mapping function $Z_{eff}(k)$ is used to transform the wavenumber k into this depth, as can be seen in figure 3.3.

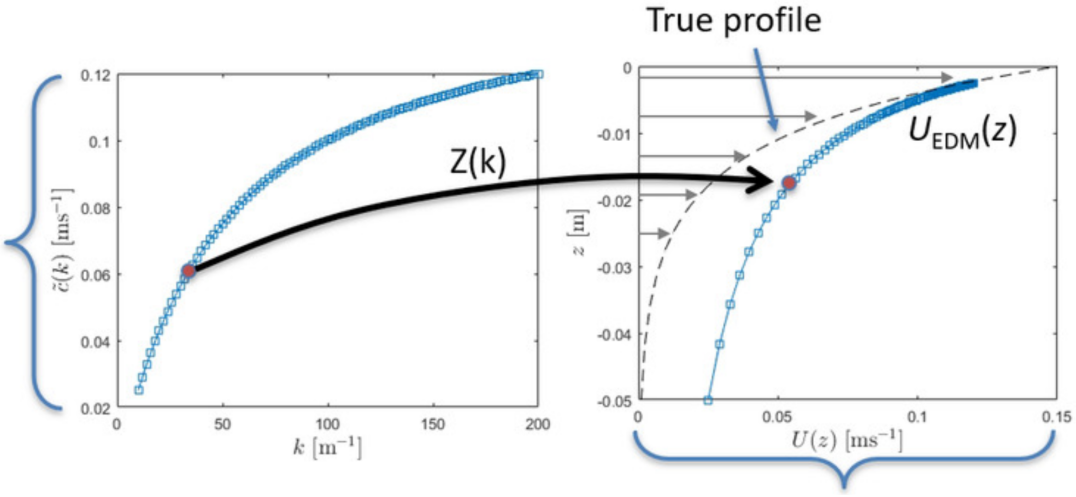

Figure 3.3: $\tilde{c}(k)$ mapped to corresponding depth with the mapping function $Z_{eff}(k)$. Reproduced from "Calculating Sub-Surface Flow from Surface Wave Measurements" by Smeltzer et al. [2021]. Reproduced with permission.

In figure 3.3, the Doppler shift velocity corresponding to wavenumbers can be seen to the left, and the Doppler shift velocities mapped to the depth can be seen to the right. These are used to find the EDM velocity profile, $U_{EDM}(z)$. The mapped profile of $U_{EDM}(z)$ differ from the true profile, which can be seen as the dashed line. The difference between the true profile and the profile derived by the EDM method increases with depth. The reason for this is that the mapping function, $Z_{eff}(k)$, is not known and dependent on the functional shape of the current profile, which in this case is assumed to be linear.

Assuming that the current profile varies linearly with depth gives the following approximation for $U(z)$:

$$U(z) = Sz + U_0, \tag{3.12}$$

Where z is the distance from the undisturbed water surface, and U_0 is the velocity at the bottom. Inserting for $U(z)$ into Eq. 3.11 the approximation for the Doppler shift becomes:

$$\tilde{c}_i = -\frac{S}{2k_i} + U_0 = U[-(2k_i)^{-1}]. \tag{3.13}$$

This shows that the approximated effective depth at deep water using the approximation derived by Stewart and Joy in Eq. 3.11 is

$$Z_{eff,linear}(k) = -(2k)^{-1} \tag{3.14}$$

for a linear current profile.

A similar relation can be derived for a logarithmic current profile, starting with an assumption of a logarithmic current-depth profile of the form

$$U(z) = U(z=0) - \frac{u*}{\kappa} log(\frac{z}{z_0}), \tag{3.15}$$

where $u*$ is the friction velocity given by $u* = \sqrt{\frac{\tau}{\rho}}$, z_0 is the roughness length, and κ is an empirical constant, the von Kármán constant. The last term of Eq. 3.15 is the same as the equation for a boundary layer velocity profile. Evaluating Eq. 3.11 with 3.15 the approximation for the Doppler shift becomes:

$$\tilde{c_i} \approx u(z=0) - \frac{u*}{\kappa} log(\frac{1}{2kr}\frac{1}{z_0}), \tag{3.16}$$

where r is a constant of 1.78. This results in a logarithmic effective depth of approximately

$$Z_{eff,log}(k) = -(3.56k)^{-1}. \tag{3.17}$$

For both the linear and logarithmic current profile assumption, the estimation of the Doppler shift velocities is performed by spanning a range of wavenumbers and assigning them to the corresponding effective depth, thus getting information of the velocities at different depths. Information of the depth velocity will be limited to a small range of depths defined by the present range of wavelengths in the measured area and the effective depth definitions. Ideally a large range of wavelengths should be measured such that the EDM might span over a wide range of wavenumbers. This will give information of the velocity at varying depths. Although the EDM is extensively used, the *a priori* assumption of the shape of the current profile is a clear weakness if the method is applied to currents where the assumption does not hold.

3.3.2 Polynomial Effective Depth Method

The Polynomial Effective Depth method is a new inversion method developed by Benjamin Smeltzer, [Smeltzer et al., 2019], at the Norwegian University of Science and Technology (NTNU). It is derived assuming deep water and follows the same steps as EDM for solving $U(z)$, but is not dependent on the assumption of the functional form of the current profile. The current profile derived from EDM is fitted to a polynomial function, and using a simple relation based on 3.11 an improved estimate for the profile $U(z)$ is constructed directly from the polynomial fit. The method is purely based on measured Doppler shift data and is free of both user-input parameters and dependence on *a priori* knowledge of the functional form of the current profile. Without being bound by the assumption of the functional form of the current profile the PEDM manages to improve the correlation between the true $U(z)$ and the derived profile $U_{PEDM}(z)$.

From an experimental set of data of the wave spectrum, a set of Doppler shift velocities, $\tilde{c_i}$, can be obtained at unique wavevector magnitudes, k_i. The Doppler shift velocities can be derived by different methods such as Least Squares

Techniques or Normalized Scalar Product, the Normalized Scalar Product being the method currently used for the PEDM.

Instead of assuming a linear or logarithmic current profile, the PEDM assumes a polynomial current profile. The functional form of the current profile is

$$U(z) = \sum_{n=0}^{\infty} (u_n z^n), \tag{3.18}$$

which is a summation of polynomial terms. Inserting for $U(z)$ into 3.11 yields the following approximation for the Doppler shift velocities:

$$\tilde{c}(k) = \sum_{n=0}^{\infty} n! u_n (-\frac{1}{2k})^n. \tag{3.19}$$

The last part of Eq. 3.19 contains the same term as that of the defined mapping function for the effective depth for a linear current profile for the EDM in Eq. 3.14. By inserting $(-\frac{1}{2k}) = Z_{eff,lin} = z$ for this term, and using it together with the EDM, the estimated current profile becomes:

$$U_{EDM}(z) = \sum_{n=0}^{\infty} n! u_n z^n. \tag{3.20}$$

From Eq. 3.20 one can see that The polynomial coefficients for each order differs with a factor of $n!$ from the true profile. It becomes clear that the mapped profile for EDM of a linear current profile is also of polynomial form with coefficients of the n-th order term differing by a factor of $n!$ from those of the true profile $U(z)$. Because the mapping function is not the correct one, the estimated velocity profile from the EDM, $U_{EDM}(z)$, will be inaccurate. This factor of $n!$ is the reason for the difference between $U(z)$ and $U_{EDM}(z)$ that can be observed in figure 3.3, and the difference between the true profile and the derived Doppler shift velocities increases with depth. To improve this inaccuracy of the EDM, the PEDM uses the difference of $n!$ between the coefficients in the series representation of $U_{PEDM}(z)$ and the true profile $U(z)$. First, $U_{EDM}(z)$ is obtained from measured values of $\tilde{c}_i(k)$ using Eq. 3.13. Then the obtained values of $U_{EDM}(z)$ is fitted to a polynomial of degree n_{max}:

$$U_{EDM}(z) \approx \sum_{n=0}^{n_{max}} u_{EDM,n} z^n. \tag{3.21}$$

The improved PEDM estimate of the current profile is then given by:

$$U_{PEDM}(z) \approx \sum_{n=0}^{n_{max}} \frac{1}{n!} u_{EDM,n} z^n. \tag{3.22}$$

In figure 3.4 the different steps of the PEDM process can be visualized. The Doppler shift velocities, $\{Z_{eff}(k_i),\ \tilde{c}(k_i)\}$ retrieved from experimental data are mapped to depths with the linear mapping function in Eq. 3.14. The polynomial fit in Eq. 3.21 based on these mapped velocities can be seen as the red line. The improved PEDM estimate of the current profile scaled by $1/n!$ given by Eq. 3.22, can be seen as the green line, which is significantly closer to the real profile $U(z)$

measured by PIV.

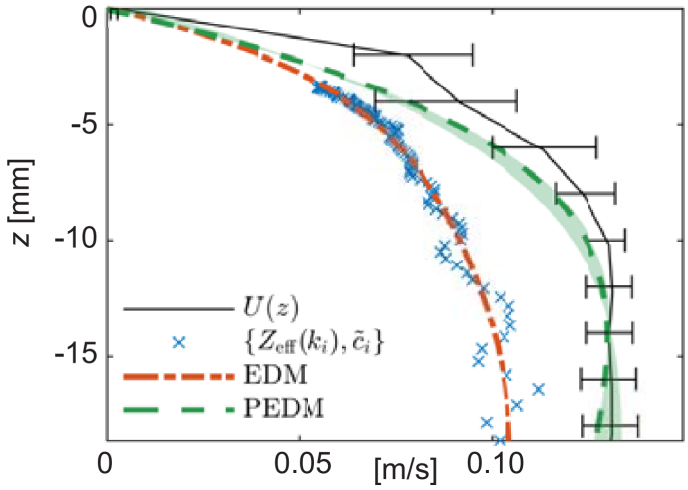

Figure 3.4: Results from the final PEDM scaled with 1/n! seen in green, and the un-scaled EDM seen in red. The blue crosses are the mapped Doppler shift velocities. The black line is the PIV with error bars. Reproduced from "An improved method for determining near-surface currents from wave dispersion measurements"by Smeltzer et al. [2019]. Reproduced with permission.

The PEDM method has proved to be more than three times more accurate than the state-of-the-art methods for currents with significantly curved profiles near the surface. For linear current profiles the EDM assumption of a linear current profiles is valid and in these cases the PEDM offers insignificant improvement over the EDM.

There are two theoretical limitations of the method. The first is that Eq. 3.19 and 3.20 assumes deep water regime and does not hold in waters of finite depth, h, where $\lambda >> h$. At finite depth the linear effective depth becomes $Z_{eff,lin} = -\frac{1}{2k}tanh(kh)$ which cannot be solved analytically with respect to k. An analysis of the effect of finite depth carried out by Smeltzer et al. [2019] reveals that the deep water assumption used in the mapping of $Z_{eff,lin}$ only leads to errors at the 1% level for all but the shallowest depths. Thus the deep water assumption for Eq. 3.19 and 3.20 yields sufficient accuracy and can be used for almost all realistic combinations of wavelengths and depth.

The second potential complication is linked to the experimental measurements of the Doppler shift velocities. As for all inversion methods that reconstruct a depth dependent current profile based on wave dispersion, the Doppler shift velocity is measured for a limited range of wavenumbers, and this will affect the accuracy. If the range of measurable wavenumbers are too small, too few Doppler shift velocities will be measured and the polynomial fit based on these points might deviate from the actual current profile, but the fit is still correct based on the available data. When taking the experimental data, the measuring might lead to errors in the Doppler shift velocities, and in combination with the limited range of wavenumbers that are measured, the error in the Doppler shift velocities can lead to errors in the fitted

polynomial coefficients, which might rapidly increase for higher values of n. To minimize the effect of this, a criterion depending on the measured Doppler shift data is implemented in the algorithm to determine the optimal parameters involved in the polynomial fit.

Chapter 4

Methodology

This chapter describes the methods and tools used in order to answer the research question. The chapter starts with the methods used to retrieve the experimental data from the wave-current laboratory. In section 4.1 the Free Surface-Synthetic Schlieren method used for measurements of the waves is introduced and in section 4.2 the Particle Image Velocimetry, used to measure the surface velocities and depth-velocities is described. Section 4.3 outlines the Copter Currents toolbox used to calculate the three inversion methods. First the dispersion relation fit algorithm of the CC method is described. Then the implementation and the steps of the PEDM and EDM_{lin} are presented. The last section, 4.4, presents a short analogy between the adaptive mesh approach used in Computational Fluid Dynamics(CFD) and the spatial windows where the dispersion relation is applied.

4.1 Free-Surface Synthethic Schlieren

Free Surface Synthetic Schlieren (FS-SS) is an optical measuring method used for measurements of the instantaneous topography of the interface between two transparent fluids. It was first introduced by Kurata et al in 1990 and later characterised by Moisy et al in 2009. The method relies on the same physical principles as Synthetic Schlieren, but whereas Synthetic Schlieren only can be applied on density-varying fluids, FS-SS can be used on fluids of constant density, such as water. The FS-SS method is based on simple optics and a black and white imaging system, and it offers a high spatial resolution at low computational costs. The equipment for taking FS-SS measurements consists of a mat with a randomized black and white dot pattern and a camera. The dot pattern is viewed through the free surface and waves will cause the dots to look distorted. The distortion is dependent on the distance between the free surface and the dot pattern. A small distance creates a small distortion and a large distance increases the amount of distortion. A too large distance can lead to difficulties of analysing and calculating the displacement field.

There are two possible setups with the camera and the dot pattern; viewing the mat with the randomised dot pattern either down through the water surface or up through the water surface. The first option requires that the water is kept in a container with a transparent bottom. The mat is placed under the transparent bottom of the container, and the camera is placed above the water surface directly

over the mat. The second option is to place the mat above the water surface with the camera placed either at the side of the water tank, angling the field of view of the camera up towards the dot pattern with a mirror angled at 45 degrees, or under the water tank, directly below the mat. An advantage of the second setup is that the distance between the free surface and the dot pattern can easily be adjusted, whereas in the first setup the distance is entirely dependent on the water depth, limiting the use of this setup to shallow waters.

The FS-SS measuring method consist of two steps:

1. Comparing the refracted image with a reference picture. The displacement field between these two can be found using a Digital Image Correlation (DIC) algorithm.

2. Reconstruction of the surface height by using a least-square integration of the surface gradient.

In the first step, a reference image of the randomized dot pattern is taken when the water-air interface is flat. A section of the reference image can be seen in Figure 4.1a. Waves and currents are then introduced to the flow, and an image series is recorded by the camera. The waves affect the light refraction at the surface, which can be observed as deformations or displacements of the dots, as can be seen in Figure 4.1b. The displacement field, $\delta r(x, y)$, between the dots on the reference image and the refracted image series is then processed with a DIC algorithm, giving the displacement field.

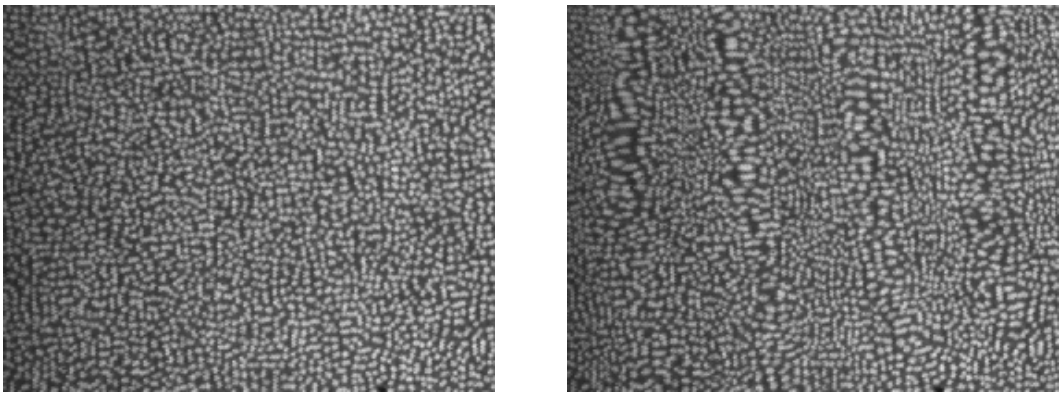

(a) Reference image (b) Refracted image

Figure 4.1: A section of the random dot pattern used in the FS-SS. The distortion of the dots between the reference image and the refracted image is used to calculate the displacement field in the DIC process. Four wave crests can be observed as vertical lines in the refracted image.

The displacement field is then used to calculate the surface height matrix, $\eta(x, y, t)$ that gives the surface height, η at location (x,y) at the time t, as can be seen in Figure 4.2. This is done by numerical integration of the displacement field, using a least-squares inversion of the gradient operator. The surface gradient can be viewed as a finite difference representation of a derivative where the surface height is the unknown. This gives an over-determined linear system, with 2M×N

equations and M×N unknowns. The resulting surface height matrix is defined as the matrix that minimizes the residual of the least-square method.

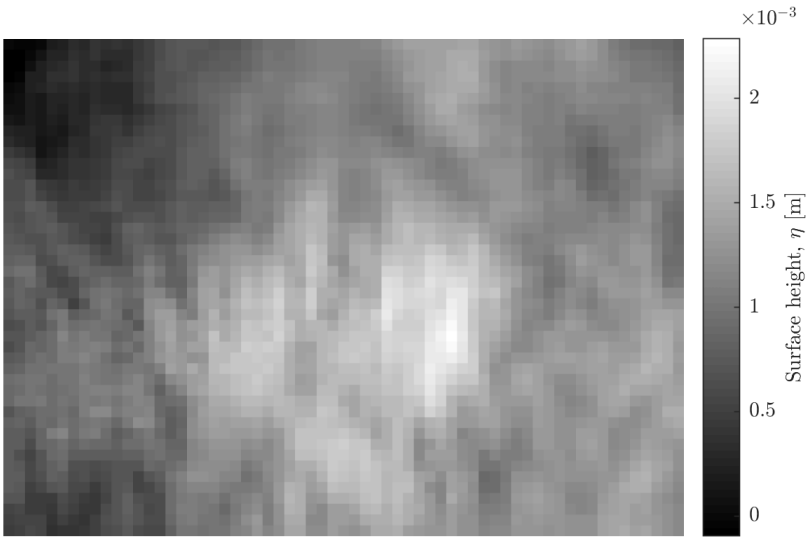

Figure 4.2: A visualization of the surface height matrix $\eta(x, y, t = 1)$.

The FS-SS method has two main limitations. The first is that it is not able to pick up signals from very small wavelengths, limiting the use to waves of linear wave theory, where the surface tension can be neglected. The second limitation is ray crossings, which occurs at large wave steepness, $\frac{\eta}{\lambda}$, or when the distance between surface and pattern is so great that it causes too much distortion on the pattern.

4.2 Particle Image Velocimetry

Particle Image Velocimetry (PIV) is an optical, whole-field technique used to measure the instantaneous velocity distribution in a plane of the flow [Cengel and Cimbala, 2010]. PIV provides velocity values simultaneously through a cross-section, unlike point based measuring methods such as hot-wire anemometry and Laser Doppler Velocimetry. The ability to capture whole-field images to great precision makes PIV a valuable tool as a truth measurement for other measuring methods. PIV consists of two main steps: visualization and image processing.

In the visualization step the flow is seeded with a tracing particle, known as a marker. The marker should have approximately the same density as the fluid, so as to be neutrally buoyant, or it should be small enough to have a negligible relative velocity to the fluid. This way the motion of the particles can be assumed to follow the flowpath of the flow. A thin slice of the flow is then illuminated by a pulsing laser light sheet at the desired plane. When the laser is pulsing, the markers are illuminated, and their scattered light is detected by a camera positioned at right angles to the light sheet. This gives the first position of the particles, and when the light pulses again, after a short time period $\Delta(t)$, the new position of the particles are recorded.

In the second step, the image processing, these two superimposed images are used to determine the displacement of the particles, $\Delta(s)$, during the time interval $\Delta(t)$ for all the particles in the flow. For each particle in the light sheet the magnitude of the velocity can be determined as

$$U = \frac{\Delta(s)}{\Delta(t)} \tag{4.1}$$

This method can be applied in both the x- and y-direction, providing two velocity components in the plane. The result of the velocity calculations can be visualized as a velocity field of the plane.

4.3 Copter Currents

Copter Currents is a MATLAB toolbox developed in the Department of Radar Hydrography at the Helmotz-Zentrum Geesthacht Centre for Material and Coastal Research. It is used to retrieve current velocity based on measurements of wave dispersion at the water surface using the dispersion relation. It has been designed to process a data file from a UAV consisting of a video read as a series of images of the water surface and metadata with information of the geographical location of the drone. The data file is loaded into Copter Currents where the image series is transformed into a series of shadowgrams representing the water surface. The water surface can then be sliced into spatial windows, as can be seen in Figure 4.3, with the possibility to change both the size, placement and distance between the windows. Dividing the area into smaller sections can give a detailed current field, as seen in Figure 4.4, while a larger window will give a velocity that is an average of the varying velocities within the covered area.

In each of the windows in figure 4.3 a dispersion relation fit algorithm can be applied and run separately based on the surface information in the given window. The time-space signal of the water surface is transformed into the frequency-wavenumber domain with a 3D FFT. The frequency-wavenumber domain for k_x can be seen to the left in figure 4.5. The result from the FFT is a power spectral signal consisting of both power from the surface waves, centered around the dispersion shell, and power related to background noise. The power from the surface waves is located along the dispersion line. This can be observed as the yellow line that appears for positive wavenumbers in the left figure 4.5. A dispersion relation fit algorithm is applied to all possible current combinations of $[Ux\ Uy]$ within a pre-defined range in the frequency-wavenumber domain. This is done using a spectral-based maximization technique based on the Signal-to-Noise(SNR) density to fit the most probable current. The best current fit is located at the combination of $[Ux\ Uy]$ where the SNR density is highest. This process can be observed in the right figure 4.5: The possible combinations of $[Ux\ Uy]$ from the dispersion relation and the frequency-wavenumber domain all have a corresponding SNR density value. The process of locating the $[Ux\ Uy]$ pair that corresponds to the highest SNR density has two steps; The black cross is for the first fit, and the red cross for the second. The $[Ux\ Uy]$ that corresponds to the

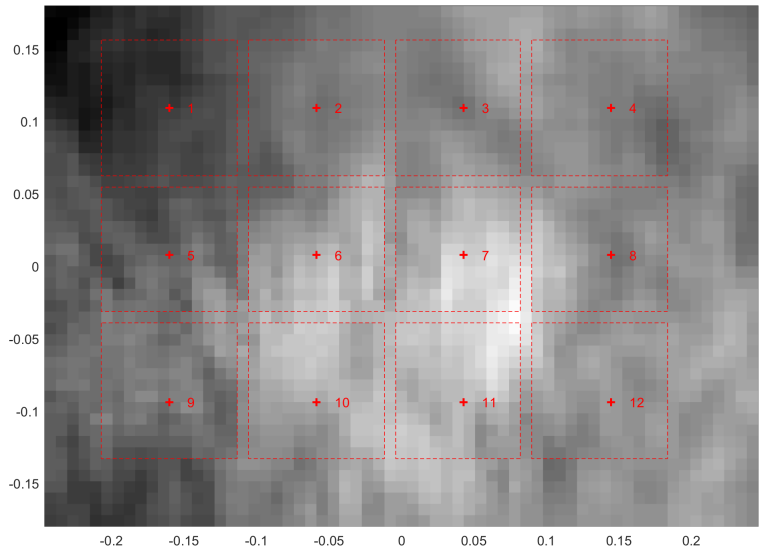

Figure 4.3: An example of window placement in Copter Currents used to retrieve a current field.

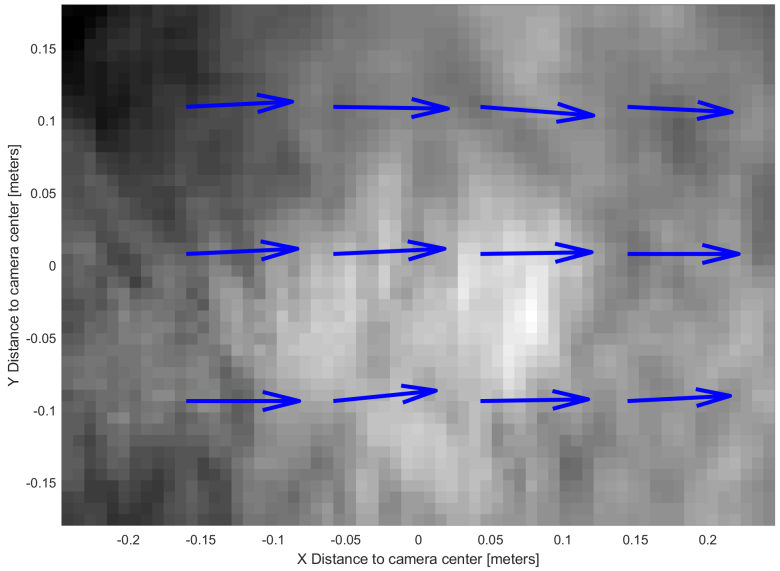

Figure 4.4: The current field retrieved using the window placement in figure 4.3.

red cross is the output velocities of the CC method.

It is also possible to use other information about the time-development of the water surface as CC input, such as the surface height matrix resulting from the FS-SS analysis, seen in figure 4.2. In this case the surface height matrix, $\eta(x, y, t)$ will replace the shadowgraph image series. For each time increment, t, the matrix contains information about the height of the water surface, η, at the given coordinate (x,y). Representing the surface height as a greyscale colour gradient

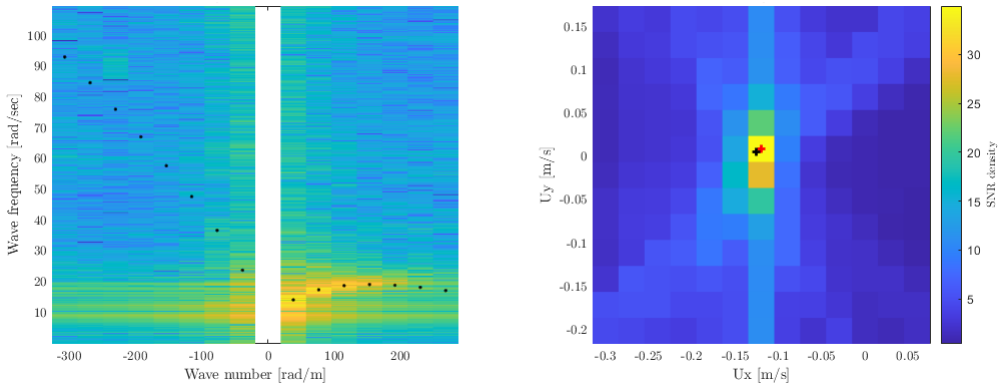

Figure 4.5: Left: The frequency-wavenumber domain with black dots marking the dispersion line.
Right: The SNR density map with possible combinations of $[Ux\ Uy]$.

gives a greyscale representation of the water surface in much the same way as the shadowgraph. The parameters in the original image sequence structure are replaced with the surface height matrix, information about the image pixel spacing, dx, dy, water depth, and the camera framerate.

4.3.1 Implementation of the PEDM and EDM$_{lin}$

In addition to solving for the depth-uniform velocity of encounter as the original Copter Current toolbox does, the linear EDM (EDM$_{lin}$) and the PEDM is integrated into the Copter Currents toolbox. This makes it possible to solve both the near-surface velocity and the depth varying current velocity with three different inversion methods. The PEDM and EDM$_{lin}$ solvers are implemented such that the CC method, PEDM and EDM$_{lin}$ all can be used on the same data set. All three methods use the same wave data input, η(x,y,t), from the FS-SS measurements, and are solved in the same areas defined by the windows.

Whilst the inversion method originally used in the Copter Currents toolbox only solves for a weighted average of the depth based on an average of multiple wavenumbers, the PEDM and EDM$_{lin}$ methods span a range of wavenumbers for each window. Rather than locating the combination of $[Ux\ Uy]$ that yield the strongest signal in a single averaged SNR density plot, as in figure 4.5, the depth dependent methods find the combination of $[Ux\ Uy]$ that yield the strongest signal for several separate wavenumbers. Each wavenumber corresponds to a certain depth, as given by Eq. 3.14. A vector consisting of a chosen range of wavenumbers is defined. Then the maximization algorithm detects the SNR density peak with the best signal for each of these wavenumbers. The $[Ux\ Uy]$ pair that corresponds to this peak is the Doppler shift velocities $[\tilde{c}_x(k) \quad \tilde{c}_y(k)]$. The process is repeated for all the wavenumbers in the vector and combining the results will give information of the depth profile of the current. The range and steps between the wavenumbers can be adjusted to correspond to the length of the waves in the data set. An example of the SNR-density maximisation process for increasing wavenumbers for profile b) can be seen in figure 4.6 for k_x=40 rad/m. k_x=120

rad/m and k_x=195 rad/m. For each wavenumber the optimal fit of the dispersion relation is located at the peak with highest SNR density signal. For both the lowest and highest wavenumber the peak is large and undefined, while in b) for the wavenumber of k_x=120 rad/m, the signal is clearly defined with a peak corresponding to a set of $[Ux\ Uy]$.

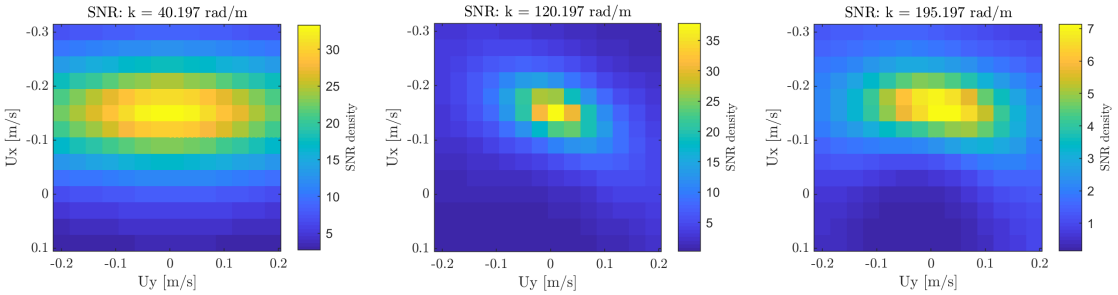

(a) k_x=40 rad/m. (b) k_x=120 rad/m. (c) k_x=195 rad/m.

Figure 4.6: The SNR density maximisation used to retrieve the Doppler shift velocities for the PEDM and EDM$_{lin}$,

A filter detects if multiple peaks are present in figure 4.6. With multiple peaks the solution of the polynomial fit is non-unique and no solution for the depth current profile is found. When all wavenumbers are processed and analysed the result of this is a set of Doppler shift velocities, $\tilde{\mathbf{c}}(\mathbf{k})$. These Doppler shift velocities are then mapped to depth with the mapping function Z(k). The mapped Doppler shift velocities can be seen as the blue crosses in figure 4.7. Based on these mapped Doppler shift velocities, the linear fit given by Eq.3.12, is performed for the EDM$_{lin}$ and the polynomial fit given by Eq. 3.18 is performed for the PEDM. The uncertainty of the polynomial fit is marked as the light and dark grey areas in figure 4.7 a). Dark grey denotes a smaller uncertainty than the light grey area. The resulting depth profile for the streamwise velocity, $Ux(z)$, of the PEDM and EDM$_{lin}$ can be seen in figure 4.7. Unlike the CC method, the PEDM defines the streamwise velocity, Ux, to be aligned with the current direction, and the cross-flow velocity, Uy, to be perpendicular to Ux, independent of whether this is in the defined x-direction of the surface. The deviation of the streamwise velocity from the defined x-direction of the surface is given by the parameter ϕ.

4.4 Adaptive mesh analogy

In CFD an adaptive mesh can be used to get a more detailed and accurate solution by decreasing the mesh size in regions of turbulence and in sensitive and difficult regions with discontinuities, steep gradients, shocks etc. The spacing between the grid points determine both the local error and the number of calculations needed to cover the domain, hence it is both a question of accuracy and cost of computation. While it would be possible to use a uniform grid with a small mesh size for the whole domain to achieve high accuracy, this approach is computationally unfeasible. It can also be difficult to predict in advance what

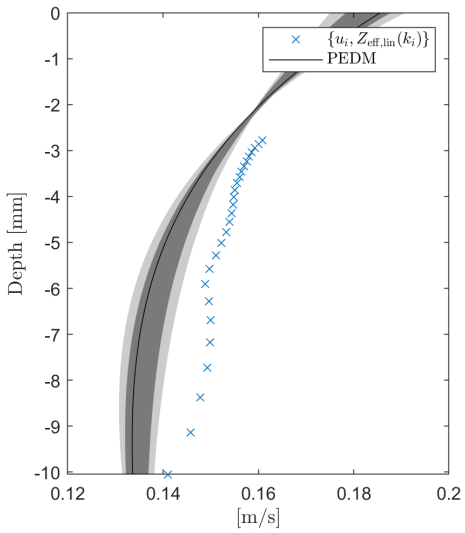

(a) PEDM with uncertainties marked in grey.

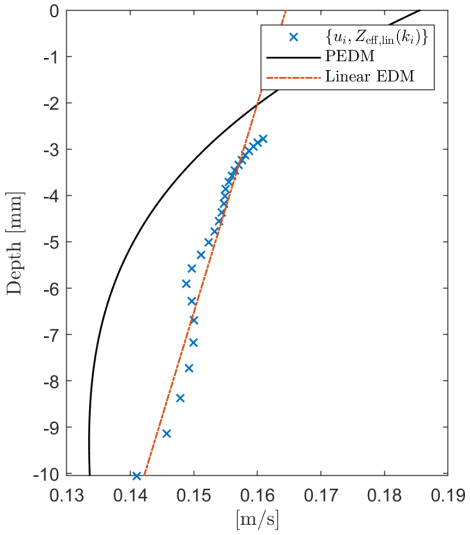

(b) PEDM, EDM$_{lin}$ and mapped $\tilde{c}$.

Figure 4.7: The resulting current profiles based on the mapped Doppler shift velocities for the PEDM and EDM$_{lin}$.

mesh size would yield acceptable results. An adaptive mesh starts out with a coarse grid and dynamically adapts the mesh size, imposing a finer sub-mesh in regions that require higher resolution. These regions are determined on a criterion linked to a parameter characterizing the solution, usually the truncation error.

A similar approach can be used when analysing the wave dispersion in a domain with varying current velocities. In areas of spatially uniform current, the mesh, or what is in this case referred to as the window size, can be kept large. Whereas in areas where the current varies, the window size needs to be decreased, and the number of windows increased so as to best capture the details of the current velocities. An implementation of adaptive windows can be added to the solver of the dispersion relation, in this case the extended Copter Currents. By using this approach of adapting the window size dynamically during the solution process, no *a priori* knowledge of the current gradient within the area is needed. Two possible parameter characterizations that could be used as a criterion for refining the windows are the velocity gradient between two windows or the SNR density maximization.

In the first criterion a limit can be set such that additional, smaller windows are created if two adjacent windows have a difference in velocities that is larger than a set value. The second criterion is based on the varying velocities within a window rather than the velocity gradients between two windows. This can be observed in a SNR density map similar to that in figure 4.6. A window with large internal variations will have either a large and undefined SNR density peak, or more than one SNR density peak. In cases with multiple peaks, the window can be divided into smaller windows.

In adaptive mesh refinement in CFD its often Partial Differential Equations (PDEs) dependent on points placed at nodes or at the boundaries that are solved. The solution of the wave dispersion relation fit is solely based on the average of the surface information from the whole area in the windows and is not dependent on any boundary conditions or specific points. The location of the output velocity is in the centre of the window, marked as a red cross in figure 4.3. To get a good resolution of the horizontal current velocity, these centre points needs to be placed as close as possible, while still ensuring that the area the windows covers is large enough. Closely spaced centres in combination with large windows can be achieved by overlapping the windows by varying degrees. The spacing between centres and the overlapping between windows can be done separately in x- or y-direction, to increase the resolution in a given direction, or combined to increase the resolution in both directions.

Different placements, spacing, size and overlap options are investigated in depth to identity the option that yields the most accurate current profile compared with the current profile retrieved from surface PIV and PIV. The overall goal of this investigation is to implement the best option into Copter Currents as an adaptive mesh that is used in areas of strong current gradients. That way the advantages of large window size can be applied where it is possible, while the smaller and more closely spaced windows would ensure a good representation of the varying velocity in areas where this is needed.

Chapter 5

Experimental Setup

This chapter will present the experimental setup in the laboratory in section 5.1 and the Copter Current setup in section 5.2. The last part of the chapter presents the three optimization alternatives, Option 1-3, in Copter Currents used to identify the window sizes and placements for optimal horizontal resolution in section 5.3, and the setup used to identify the optimal vertical resolution in section 5.4.

5.1 Laboratory setup

The data set was acquired from the fluid mechanics laboratory at NTNU and consist of four shear flow profiles, represented by a matrix of the surface height $\eta(x, y, t)$. The different shear profiles were created by adjusting the speed of the background current. Measurements of the wave spectra and the current velocities were carried out using FS-SS and PIV measurements respectively.

The laboratory setup used for measuring the wave spectra can be seen in figure 5.1. It consist of a 2x2 m transparent plate with a thickness 0.022 m for both the bottom and sides of the tank. The tank is filled with water and a pump is used to drive a controllable laminar background shear flow over the transparent plate. To ensure that the flow is laminar as well as to straighten and direct the flow, two honeycomb structures are placed right after the pump outlet. Different shear profiles can be obtained by flow conditioning such as inserting a curved wire mesh between the honeycomb structures. The curved mesh will distort the streamlines and produce a vertical uniformly sheared flow with a flow profile of peak velocity at the surface, and velocity decreasing with depth. The velocity of the surface current and the near-surface shear strength can be changed by adjusting the power of the pump and water depth. Decreasing the water depth gives more shear near the surface and decreasing the power of the pump gives lower surface current velocities.

To create a flow with strong current gradients across the horizontal flow direction, the wired mesh was moved so that only the left part of the flow would go through it. This created a partially blocked flow, where the flow going through both the honeycomb mesh and the wired mesh was slowed down compared to the part of the flow only going through the honeycomb mesh. In addition to slowing down the

flow, the flow going through the wired mesh should make the shear profile more uniform compared to the open side of the flow.

Waves were created using a plunger-type wavemaker placed downstream with the waves traveling in the opposite direction of the current. It runs in a 60 second cycle and produces waves over a range of wavelengths with a Gaussian wavefield with a wave steepness of 0.03. It is important to keep in mind that the FS-SS method struggles to measure the surface if the wave steepness is too high when setting the wave steepness-parameter. All wavemaker parameters can be seen in Table 5.1.

Table 5.1: Wavemaker parameters

Parameter	Value
Wave field	Gaussian
Frequency spread, $\Delta\omega$	$2{\cdot}\pi{\cdot}1.0$
Centre frequency, ω_0	$2{\cdot}4\pi{\cdot}4.0$
Wave steepness, ϵ RSM	0.03
Run duration [s]	60

The waves were measured using FS-SS, and the surface current and current depth-profile of the shear flow was measured with PIV to be used as truth data to compare against the current velocities obtained with the CC, the PEDM and the EDM_{lin} . The measurements were carried out with a water level of 0.07 metres and at four different pump speeds settings. All lab parameter settings can be seen in Table 5.2

Table 5.2: Laboratory parameters

Parameter	Value
Water depth, h [m]	0.07
PIV position 1 [m]	0.072
PIV position 2 [m]	0.326
Pump settings [% of max speed]	30, 40, 50, 60

5.1.1 FS-SS

The surface height was measured with FS-SS using the second setup alternative with the dot pattern placed above the surface. The randomised dot pattern was placed at height h above the water surface and the camera placed beside the tank at a level lower than the tank bottom. The field of view of the camera was angled up towards the dot-pattern with a mirror at 45 degrees placed directly under the dot pattern. A figure of the FS-SS setup can be seen in Fig. 5.1. Before introducing waves and current into the flow, a reference picture of the dot-pattern was taken to use in the DIC process. For each flow profile an image series consisting of 750 images was taken of the randomised dot pattern. With a framerate of 35.1 Hz, this corresponds to 21 seconds of observation of the water surface. The framerate is assumed to be frequent enough so as to avoid aliasing of the signal. The displacement field and the integration of the gradient operator was calculated in MATLAB, and the resulting output was a matrix of the surface elevation, η, as a function of time, as well as data

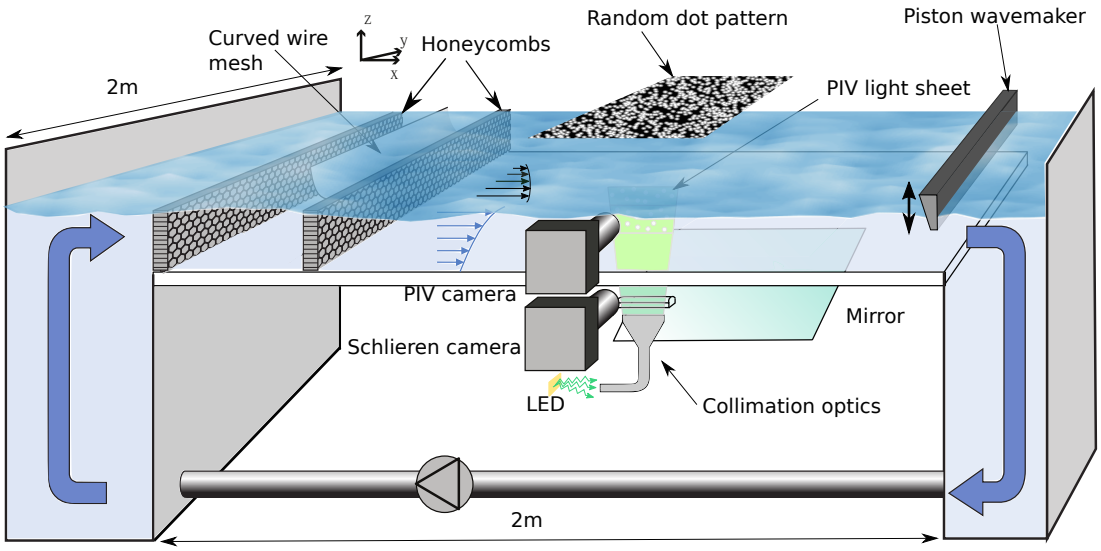

Figure 5.1: The laboratory setup used for measurements of the wave spectrum in the presence of a controllable background shear flow.

about the pixel spacing, dx and dy, and the framerate of the camera. The surface height matrix and the data were then analysed using the Copter Currents toolbox.

5.1.2 PIV

PIV measurements were used as truth measurements of the flow field. Two sets of PIV measurements were taken, one spanning horizontally across the surface, the other measuring the depth current profile. For both PIV measurements, the water was seeded with 40 μm polystyrene spheres as a marker. The planar light sheet was created by setting up an array of high-power Light-Emitting Diodes (LED) under a thin rectangular slit. The camera framerate set to 49.8 frames per second. Before the measurements were taken a calibration-block placed within the cameras field of view was depicted to be used as calibration reference in the image processing.

The surface PIV measurements were taken across the flow, measuring the streamwise velocity $ux(y)$. The pulsating LED light sheet was projected horizontally onto the water surface and illuminated a plane of the water surface at z=0. A camera placed directly above the pulsating light sheet detected the scattered lights from the markers each time the laser pulsated. A picture of the flow was taken every Δt= 0.02 second.

The depth profile of the shear flow was measured at two y-locations in the flow, shown in figure 5.8. Position 1 was located in the area blocked by the wired mesh at y=-7.6 cm. Position 2 was located in the open flow at y=-32.6 cm. Measuring at the two different positions gave both a picture of the local velocity profile at the given location, as well as the spanwise change in the depth-velocity profile caused by the blocking curved mesh. The camera was placed at the side of the tank, viewing the LED light sheet through the transparent wall. The the LED light

sheet was placed under the tank bottom, creating a vertical light sheet in the flow.

The image processing of the PIVs was done in MATLAB. The displacement of the markers, ΔS, between each image over the time interval, Δt, was used to calculate the velocity of the flow at each location. The output of the image processing was an averaging of the local current velocity along a line in the flow, rather than a velocity field of the whole section. For the surface measurements this gave the streamwise velocity over y, $Ux(y)$, at z=0 at eleven y-locations. For the depth measurements the output was the stremawise velocity as a function of z, $ux(z)$, at position 1 and 2, where the velocity at each depth was the averaged velocity along the x-direction over the whole length of the LED light sheet.

The measurements and post-processing of the data in the lab resulted in PIV data, surface PIV data and a surface height matrix $\eta(x, y, t)$ for each flow profile. The surface height matrix is used as input in the Copter Current toolbox that is used to analyse the wave dispersion with the three different inversion methods; the CC method, the PEDM and the EDM$_{lin}$.

5.2 Experimental setup in Copter Currents

All calculation parameters used in the calculations withe CC method can be seen in Table 5.3

Table 5.3: Calculation parameters used for the CC calculations of the surface velocity.

Parameter	Variable name	Value
Minimum window size	sq_size_m_min	0.0313
Maximum window size	sq_size_m_max	0.1719
Pixel size [m]	dx, dy	0.0078
Distance between squares, y-direction [m]	sq_dist_m	dx=0.0078
Time step [s]	dt	0.02
Wave length limits [m]	waveLenght_limits_m	[0.02 0.08]
Water depth [m]	water_depth_mask_2D	0.07
SNR density threshold	SNR_density_thr	3
Ux limits [m/s]	Ux_limits	[-0.3 0.3]
Uy limits[m/s]	Uy_limits	[-0.3 0.3]
Current step in first guess [m/s]	U_GF_res	0.1
Filter width FG [rad/s]	w_width_FG	1
Current step in SG [m/s]	U_SG_res	0.01
Filter width SG [rad/s]	w_width_SG	0.5

5.2.1 Identification of the optimal PEDM calculation parameters

The PEDM method is more sensitive to the wavenumber parameters than the CC method because it sweeps over a range of wavenumbers corresponding to different depths. Both the range of wavenumbers and the spacing between wavenumbers in the range is of importance and affects the result in different ways. The initial wavenumber range and steps were set as:

$$wavenumbers = dk \cdot 2 : dk : 200, \tag{5.1}$$

where the minimum wavenumber and step size were determined from dk, which is defined as:

$$dk = 0.5 \cdot \frac{2 \cdot \pi}{\lambda_{max}} = \frac{0.5 \cdot 2 \cdot \pi}{window\ size}. \tag{5.2}$$

The formula for dk sets the steps between the wavenumbers to be half of the minimum wavenumber. The minimum wavenumber corresponds to the largest wavelength, λ_{max}, which will be approximately equal to the window size, λ_{max}=window size. With the value of dk in Eq. 5.2 the minimum wavenumber in the wavenumber range will be 2$\cdot$ dk, which corresponds wavelengths equal to the window size.

The step size in the wavenumber range is linked to the number of mapped Doppler shift velocities $\{u_i,\ Z_{eff,lin}(k_i)\}$ in figure 5.2, where u_i is the Doppler shift velocity $\tilde{c}_i$. A small step size results in more closely mapped Doppler shift velocities in the plot and will lead to a better basis when the current profile is fitted based on these data points. By using 2$\cdot$ dk as the minimum wavenumber in Eq. 5.2, the minimum wavenumber increases with decreasing window sizes, which makes sense, as the window cannot observe wavelengths longer than the dimensions of the window. However, using dk as the step size between the wavenumbers will leads to larger steps in the wavenumber range for the smaller windows, which will decrease the number of Doppler shifts velocities. With fewer point the PEDM might have trouble with the polynomial curve fit.

A short analysis of the effect of different parameter combinations was carried out in order to find a combination that ensured that both the depth range was maximised and that a sufficient number of mapped Doppler shift velocities were found for the curve fit.

The upper wavelength limits of 0.08 m set in the CC part of the algorithm was found to override the lower wavenumber range defined in the PEDM section. No solution was found for wavenumbers lying within the area of no data in the $k_x, k_y, \omega_{average}$ plot in figure 6.13, which can be seen as the dark blue area in the centre. Two sets of new wavelength limits were explored; λ_{max}=0.2 m and λ_{max}=0.4 m. With the upper wavelenght limit set to 0.4 m the The maximum effective depth increased for the largest windows, but few to none Doppler shift velocities were located at these depths. This is probably because there were too few waves of this size, and if any were observed they lead to the single outlier

Doppler point value located at the maximum depth, as can be seen in figure 5.2 b). The rest of the Doppler points were located at the top half of the depth, down to $\sim$ -11 mm, leaving the lower half with a single point. With the upper wavelength limit set to 0.2 m, mapped Doppler shift velocities were evenly distributed down to -10 mm. λ_{max}=0.2 m was deemed a suitable upper wavelenght limit for the PEDM calculations. The velocity plot with the two different upper wavelength limits can be seen in figure 5.2.

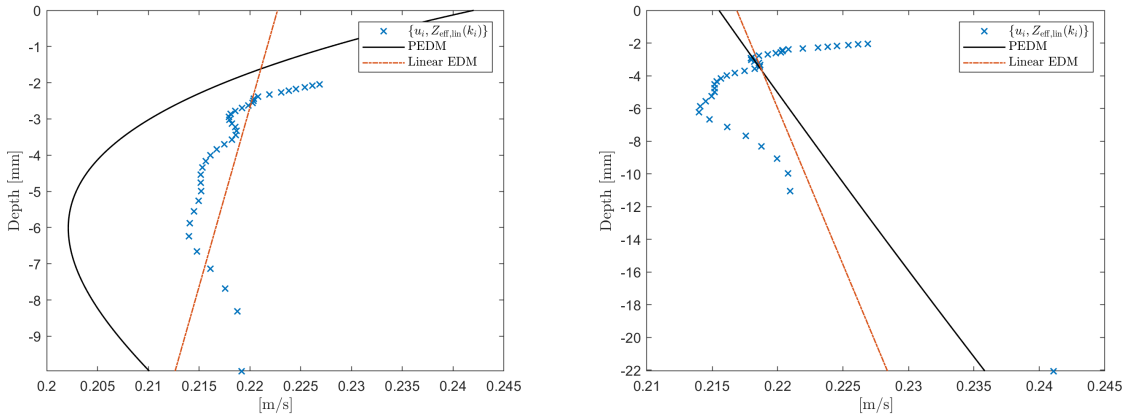

(a) λ_{max}=0.2 m. (b) λ_{max}=0.4 m.

Figure 5.2: The velocity profile of the PEDM, the linear EDM$_{lin}$ and the mapped Doppler shift velocities for a window size of 0.3125 m and a wavenumber vector of [dk·2:5:250]. In b) an outlier mapped Doppler shift velocity can be observed at (0.24,-22).

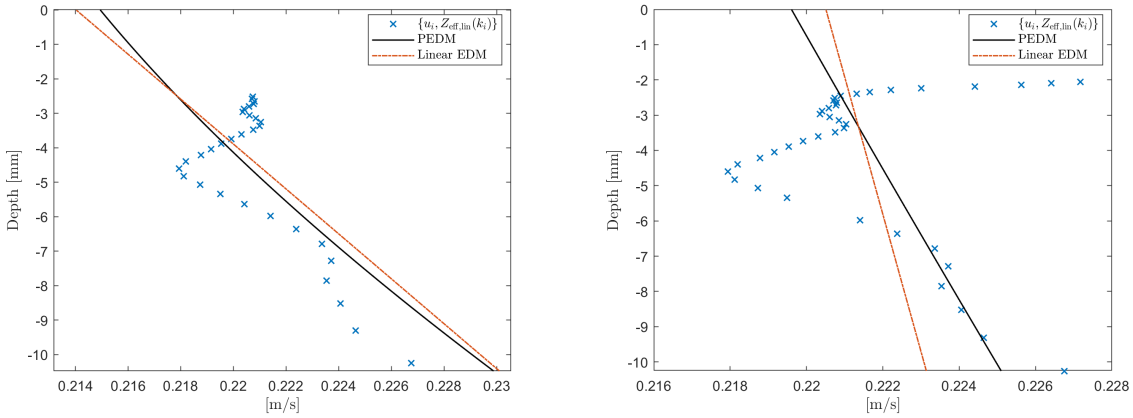

(a) Maximum wavenumber=200. (b) Maximum wavenumber=250

Figure 5.3: The velocity profile of the PEDM, EDM$_{lin}$ and the Doppler shift velocities for a window size of 0.2657 m and a wavenlength limits of [0.02 0.2]. In b) k_{max}=250 rad/m causes the Doppler shift velocities to increase in velocity and converge towards a depth of -2 mm.

Similarly as for the lower wavenumber limit discussed above, two different alternatives for the upper wavenumber limit was explored. With an upper

wavenumber of 200 rad/m the depth is not resolved for shallower depths than -2.5 mm, as can be seen in figure 5.3a. Figure 5.3b shows an attempt at running the PEDM with 250 rad/m as the highest wavenumber, in order to capture the velocity as close to the surface as possible. The increase in the maximum wavenumber lead to an increased number of Doppler data points close to the surface. The points converged towards a depth of $\sim$ 2 mm with increasing velocity, rather than giving data of points closer to the surface. According to Eq. 3.14 the effective depth for waves with k=250 is 2 mm which explains why this is the smallest depth we get data from, but it does not explain why the Doppler shift velocities at this depth span over a wide range. This almost horizontal increase might be caused by the noise in the signal, giving ambiguous results in the SNR density maximization algorithm. To avoid the converging Doppler shift velocities at -2mm, k_{max}=200 rad/m was chosen as the upper wavenumber.

The step size was changed from dk to 5 to avoid that the step size increased as the windows got smaller. This ensured enough Doppler data points for the polynomial fit for all window sizes. All calculation parameters used in the calculations of the surface velocities with the PEDM, EDM$_{lin}$ and the second set of CC can be seen in table 5.4.

Table 5.4: Calculation parameters used for the PEDM and EDM$_{lin}$ calculations of the surface velocity

Parameter	Variable name	Value
Minimum window size	sq_size_m_min	0.0469
Maximum window size	sq_size_m_max	0.1719
Distance between squares, y-direction [m]	sq_dist_m	dx=0.0078
Time step [s]	dt	0.02
Wave length limits [m]	waveLenght_limits_m	[0.02 0.2]
Water depth [m]	water_depth_mask_2D	0.07
Wavenumber step	dk	π/window size
Wavenumber vector	wavenumbers	[dk·2:5:200]
SNR density threshold	SNR_density_thr	2
Ux limits [m/s]	Ux_limits	[0.0 0.3]
Uy limits[m/s]	Uy_limits	[-0.2 0.2]
Current step in first guess [m/s]	U_GF_res	0.1
Filter width FG [rad/s]	w_width_FG	1
Current step in SG [m/s]	U_SG_res	0.01
Filter width SG [rad/s]	w_width_SG	0.5

5.3 Optimization of near-surface velocity

The spanwise variation of the streamwise velocity, $Ux(y)$, for profile a) -d) is measure by the surface PIV. The four profiles are designed to have surface

velocities that varies with y, creating surface profiles of different overall velocities and different levels of shear within the flow. The optimization process explores three different approaches termed Option 1, Option 2 and Option 3 for capturing an accurate and detailed representation of surface current gradients with the CC method, the PEDM and EDM_{lin}. The surface PIV is used as truth measurement to validate the efficiency of the different methods. Each approach investigates a certain placement, shape and number of windows, and how this affects the results. The goal is to find the combination of these factors that infers a surface velocity profile that resembles the velocity profile from the surface PIV, capturing the spanwise changes in the velocity profile.

The input data from the FS-SS of the time-evolution of the water surface is the 64 $\cdot$ 47 $\eta(x, y, t)$ matrix depicted in figure 4.3. To best be able to capture the change in velocity that takes place over the y-direction one window centre was placed for each spanwise pixel, giving 47 windows between y=0 m and y=-0.35 m, as can be seen in figure 5.4. With a pixel size of 0.0078 m this setup requires a large amount of overlap between the windows. To be able to derive velocities close to the top and bottom boundaries of the domain, window centres are placed all the way out to the edges. To be able to place the centres this close to the edge, the size and shape of the bordering windows are adjusted from square to rectangular, as can be observed in figure 5.5. The number of windows that are affected by the upper and lower boundary increases as the window size is increased.

For each approach the effect of various window sizes is investigated, to find a good balance between spatial precision by using small windows and having windows that are large enough to retrieve surface data with a good k_x resolution that affects the dispersion relation fit algorithm. The windows are increased around a centre-coordinate that remains constant. For each run the dispersion relation fit algorithm is applied, calculating the surface velocity before the size of the window is increased by one pixels in all four directions. For the For Option 1 and 3 the starting size of the windows used with the CC method covered 3·3 pixels or 0.0313·0.0313 m^2. The PEDM and EDM_{lin} required a slightly larger spatial window for the algorithms to run, so the minimum window size for these methods were set to 5·5 pixels or 0.0469 $\cdot$ 0.0469 m^2. For Option 2 the starting window height were the same for Option 1 and 2, but the length of the window was set to cover the whole domain. The maximum window size was 0.1719 $\cdot$ 0.1719 m^2 for all three options.

Option 1: Uniform flow in the flow direction

The first and simplest attempt at deriving an accurate representation of the surface current velocity with calculations from the CC method is based on the assumption that the surface velocity is uniform in the flow direction. By assuming that the velocities are constant in the x-direction, one can calculate the cross-sectional velocities at one location of the flow by placing a single column of square windows across the flow at any random x-location. The windows were placed at the centre x-location, as can be seen in figure 5.5. To better visualise the setup the number of windows in the figure are decreased down to five, and the

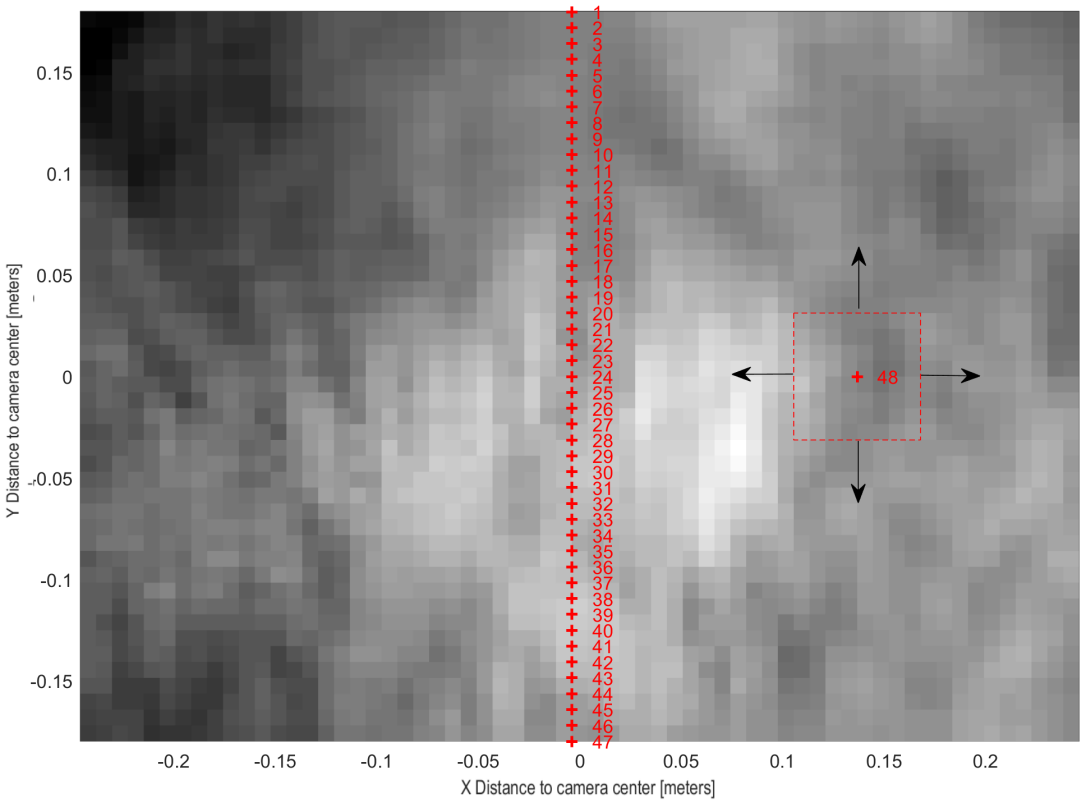

Figure 5.4: The setup of the 47 window centres spanning across the flow. Each cross is the centre in a window that incrementally increases in all directions. An example of this can be seen to the right.

windows are not overlapping.

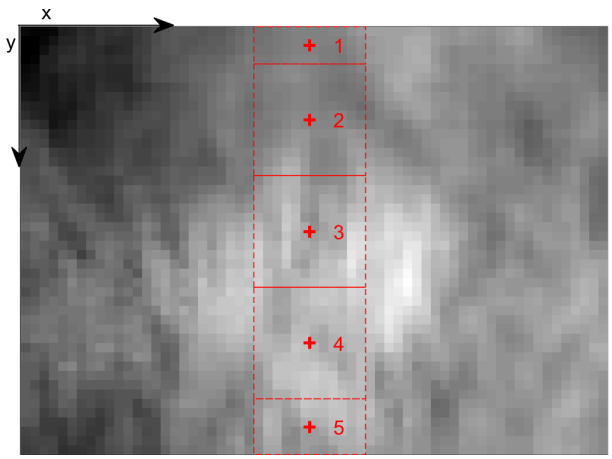

Figure 5.5: A simplified visualization of the window placement in Option 1. In reality there are 47 windows instead of 5, and the windows are overlapping. In window 1 and window 5 the boundaries affects the shape of the windows.

Option 2: Rectangular windows

The second approach assumes that the flow velocities varies in the flow direction, so the whole flowwise area should be included in the calculations. This is in line with the surface PIV velocity, which is calculated as an average of the varying measured velocities along the whole length of the domain. To cover the whole length of the domain with the windows the shape of the windows was changed to rectangles with the same length as the flow domain, see Figure 5.6. This length is kept constant while the velocity across the flow domain is calculated for windows of heights increasing from the minimum window size up to 0.1719 m. This way the calculated velocity from each window would be an average based on surface information from the whole length. By increasing the length of the windows more information of the wave development in the x-direction can be analysed, increasing the k_x resolution. Since it's only the velocity in the flow direction, U_x, that is of interest, increasing only the length of the window could increase the accuracy of U_x, compared with square windows of equal height.

Option 3: Averaging the velocity over the x-direction

The third approach is built on the same assumption as the second approach; variation of surface velocity in the flow direction. Rather than using one large rectangular window covering the whole length of the measurement domain, several columns of square windows were placed along each other with no overlap in the x-direction. In the y-direction there was still 47 windows with one pixel overlap between. After deriving the spanwise velocities of each column, the average spanwise velocity was found by calculating the average of all columns. To number of columns placed in the x-direction decreased with increasing window size. To avoid any possible effects non-square windows might cause only a whole number of columns were used. For certain window sizes this meant that a small area to the

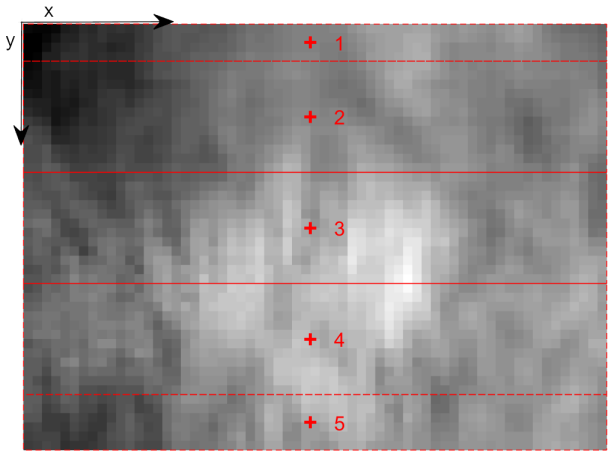

Figure 5.6: A simplified visualization of the window placement in Option 2. The dimensions of the windows in y-direction are the same as for Option 1, and incrementally increases. The windows are expanded to span the whole length in the x-direction and is kept constant.

far right in the domain was not included in the analysis. Although this option is similar to option 2, it is explored because the shape of the analysed area might affect the algorithm and the results.

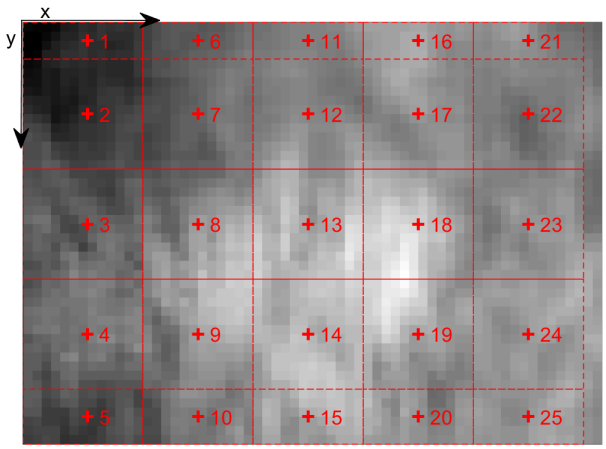

Figure 5.7: A simplified visualization of the window placement in Option 3. For each row, a single Ux component is derived that is an average of all Ux components of the row.

5.4 Optimization of depth dependent velocity

The calculation parameters used in the analysis of the depth-dependent velocity can be seen in Table 5.5. All other relevant parameters were kept the same as in the calculation of the surface velocity, as seen in Table 5.4.

For the depth-dependent streamwise velocities, $Ux(z)$, from the PEDM and EDM_{lin}, the calculated velocities are investigated for window sizes ranging between

Table 5.5: Calculation parameters used for the PEDM and EDM_{lin} calculations of the depth-profile.

Parameter	Variable name	Value
Minimum window size	sq_size_m_min	0.0625
Maximum window size	sq_size_m_max	0.1407
PIV placement Position 1 [m]		y=-0.076
PIV placement Position 2 [m]		y=-0.32.6
Adjusted window placement Position 2 [m]		y=-0.32.6+0.023

$0.0625 \cdot 0.0625$ m^2 and $0.1407 \cdot 0.1407$ m^2. The smallest window size is limited by the maximum effective depth this window size originally achieves, which is 5 mm for windows of $0.0625 \cdot 0.0625$ m^2. Analysing window sizes smaller than this results in shallow effective depths, giving a too limiting range of mapped Doppler shift velocities to do an extrapolation of the current profile down to larger depths. The largest window size of $0.1407 \cdot 0.1407$ m^2 is set based on the largest possible square window size placed over the y-location of the PIV at Position 1 and Position 2. Due to the PIV measurements positions being placed close to the upper and lower edges of the domain, square windows larger than 0.1407 m will go outside the domain at the upper and lower edge respectively, giving rectangular windows that can cause complications in the analysis. To be able to analyse the same range of window sizes at Position 1 and Position 2, the window covering Position 2 that is used in the analysis of the velocities from the PEDM and EDM_{lin} is moved 3 pixels (2.3 cm) closer towards y=0 than the original y-location of the PIV measurements at Position2. The placement of the windows covering Position 1 and 2 for the maximum window size can be seen in figure 5.8. For each window size within this range the depth-dependent velocity profile is found for the streamwise velocity, $Ux(z)$.

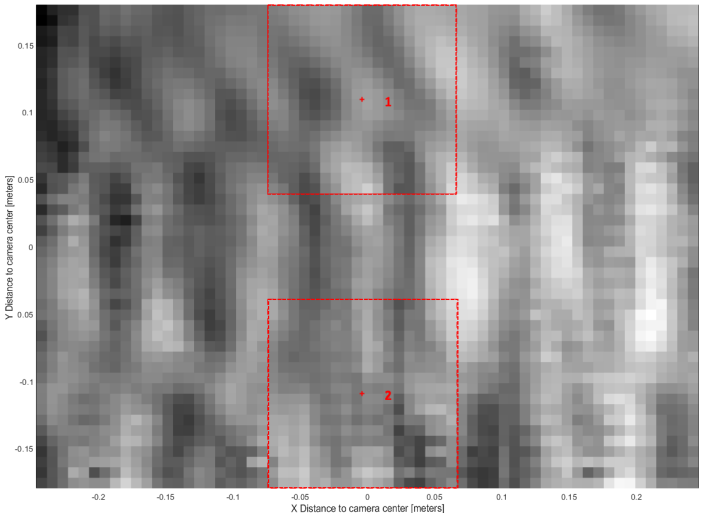

Figure 5.8: The PIV was measured at position 1 and position 2, as marked by the red crosses.

5.4.1 Extrapolation

Because the maximum effective depth is dependent on the size of the analysed domain, the maximum effective depth decreases with decreasing window size. In order to be able to analyse and compare windows of different sizes over the same depth range an extrapolation is performed for all window sizes smaller than the maximum window size. The extrapolation is based on the mapped Doppler shift velocities, where the depth range of the polynomial fit is extended down to the given maximum depth $Z_{0.1407}$=-9mm, rather than being limited by the deepest mapped Doppler shift velocities for the current window size. The polynomial fit for each window size is solved by $Ux(Z_{max})$, where Z_{max} is a vector spanning from z=0 mm to z=-9 mm.

Chapter 6

Results and Discussion

This chapter will present and discuss the results of the experiments conducted in order to answer the three research questions. Four different shear flows, referred to as profiles a)-d), are measured with PIV and surface PIV and the same flows are analysed with the three inversion methods; PEDM, EDM_{lin} and CC method.

The horizontal resolution is investigated by evaluating the surface velocities of the three inversion methods. The surface profiles measured by the surface PIV is presented in section 6.1. The surface velocity as a function of window size is analysed with the CC method in section 6.2, and with the PEDM and EDM_{lin} in section 6.4. The key findings from these sections shows that the optimal window size for horizontal resolution is achieved for windows of approximately $0.06 \cdot 0.06$ m^2 for all three inversion methods. The CC method performs best by averaging the velocity over the x-direction with Option 3, but due to the large amount of vertical shear in the flow, the CC method calculates the velocity at the effective depth, rather than the surface velocity. The PEDM and EDM_{lin} proved less sensitive to the number of windows and window placements and performed well with both the single column of windows used in Option 1, and with Option 3. The PEDM and EDM_{lin} manages to measure the surface velocity with greater accuracy than the CC method, due to taking vertical shear into account.

The vertical resolution in Research question 2 is analysed in section 6.6 by evaluating the depth-range and depth-velocities as a function of window size with the PEDM and EDM_{lin}. The results presented in this section shows that the vertical accuracy increases with increasing window size. Due to a close to linear PIV in the resolved depth-range, the PEDM and EDM_{lin} performs equally well.

A sensitivity to the range of measured wavenumbers leading to poor accuracy of the polynomial fit was discovered for the PEDM, and this is discussed in section 6.7.

In section 6.8 the results of sections 6.2, 6.4 and 6.6 are used to identify the window size that balances the horizontal and vertical resolution in order to answer Research question 3.

The chapter ends with an evaluation of possible error sources in section 6.9.

6.1 Surface profiles

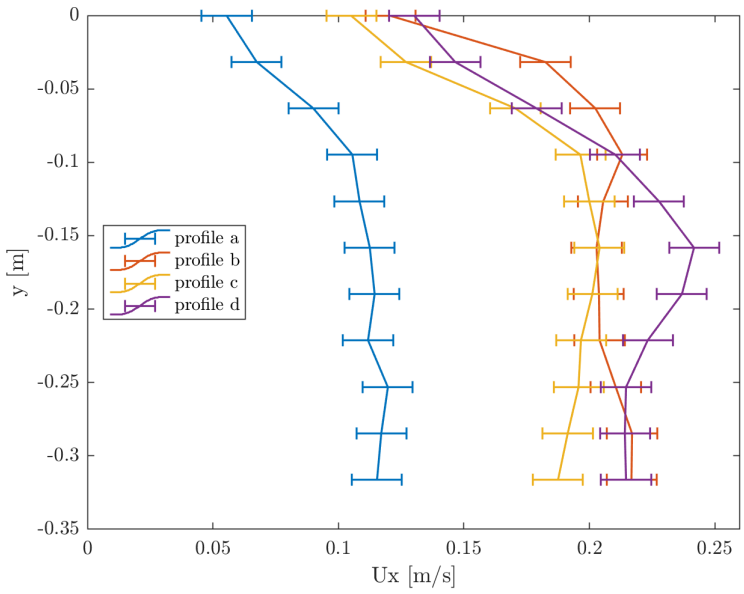

Figure 6.1: The horizontal surface profile of the streamwise velocity, $Ux(y)$, for profiles a)-d)

The surface currents measured by surface PIV is shown in figure 6.1, and is used as «truth» measurements when comparing and validating the results from the surface velocities from the CC method, the PEDM and EDM. The surface PIV measured the spanwise velocity of the streamwise velocity component $Ux(y)$. To allow for easier plotting, the y-axis is set to go from y=0 to y=-0.35, rather than placing y=0 at in the middle as is done in the Copter Currents $\eta(x, y, t)$ matrix in figure 5.4. The top half, from y=0 m to approximately y=-0.15 m is partially blocked by the curved mesh that reduces the velocity of the flow without creating eddies and other disturbances in the flow in the intersection between the open and partially blocked part of the flow. A reduction of velocity can be observed in this area for all four flow profiles. Profile a)-c) exhibit the same overall shape, with stable velocities in the open region between y=-0.15 m and y=-0.32 m whereas profile d) reaches a peak velocity at y=-0.15 m. The variation of velocity gradients both within the profiles spanwise surface velocity and between the different profiles makes this dataset a good starting point for analysing how well the inversion methods manages to capture the velocity gradients in the flow, and how the different sizes of the analysed areas affects the results.

6.2 Surface velocity, Copter Currents

6.2.1 Option 1

The streamwise surface velocity across the flow, $Ux(y)$, for Option 1, profile c), can be seen in figure 6.2. The surface profile from the CC method for four different window sizes are plotted together with the surface PIV. The calculated surface profiles derived from profile a), b) and d) show the same trends and behaviours with regard to both the window size dependency and the deviation from the surface PIV as profile c), and are therefore not presented.

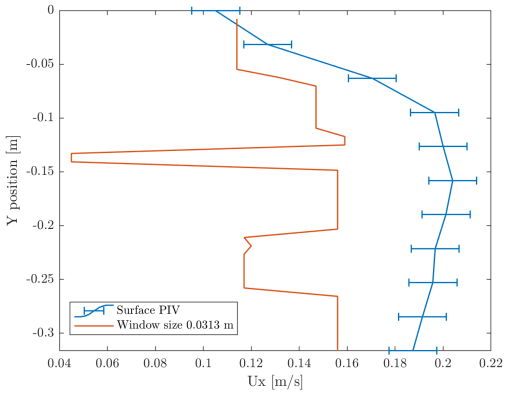

(a) Window size=0.0313 · 0.0313 m^2.

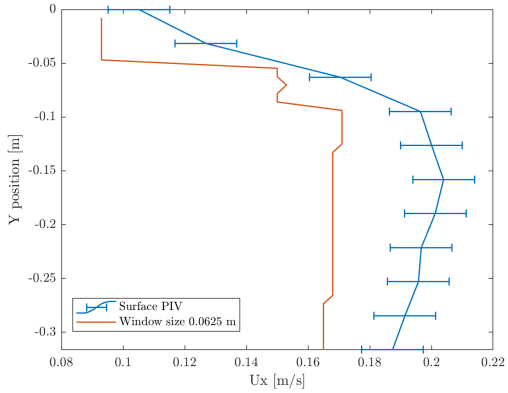

(b) Window size=0.0625 · 0.0625 m^2.

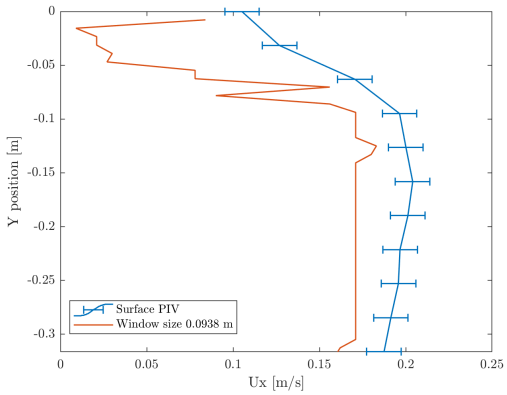

(c) Window size=0.0938 · 0.0938 m^2.

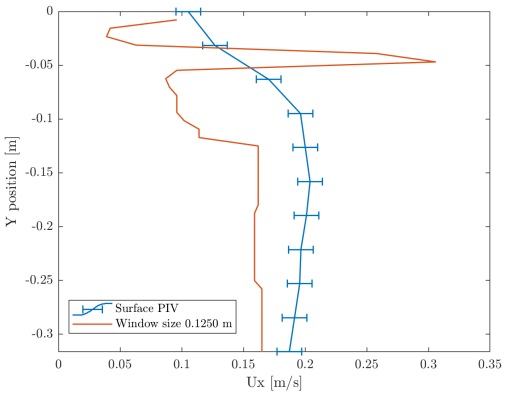

(d) Window size=0.1250 · 0.1250 m^2.

Figure 6.2: Option 1, profile c). $Ux(y)$, the spanwise surface profile of the streamwise velocity.

The surface velocity profile derived from the smallest window size of 0.0313 · 0.0313 m^2 shows unstable behaviour, the velocity changing drastically between adjacent points. Most notable is the sudden drop in velocity between Ux=0.159 m/s at y=0.125 m and Ux=0.045 m/s at y=-0.139 m. As well as being unstable across y, the derived velocities are consistently lower than the surface PIV velocities, and there is small resemblance between the shape of the calculated surface profile and the profile from the surface PIV.

The large change between bordering points can be explained by a shortage of analysable waves due to the small surface area covered by the windows. As of Table 5.3, the minimum wavelength is 0.02 m, which leaves a very small range of possible wavelengths in a window of length 0.0313 m. The small range of wavelengths and the small spatial size of the window leads to a small range of ks in the frequency-wavenumber domain and low resolution of the k-space used in the dispersion relation fit. The small range of analysable wavelengths does not however explain why all calculated velocities are lower than the surface PIV velocities. With a small window, only short wavelengths with corresponding high wavenumbers are analysed, and with the inverse relationship between the wavenumber and the effective depth in Eq. 3.14, this should give a velocity weighted close towards the surface and the surface velocity measured by the surface PIV.

Increasing the window size leads to a larger range of observable wavelengths and therefore better resolution in k-space. This in turn gives a better fit of the dispersion relation in the ω-k space. With a window size of $0.0625 \cdot 0.0625$ m^2 the shape of the surface profile derived from Copter Currents roughly matches that of the surface PIV, but again the derived velocities are all lower than the truth measurement. The closest match between the derived velocities and the surface PIV is in the area of partially blocked flow at the top half. The CC method successfully manages to capture the large current gradient that takes place in this area.

The surface profile for the two largest window sizes in Figure 6.2 shows instabilities in the region where the surface PIV decreases towards y=0 m. The instabilities in this region might be caused by the boundary of the domain. As seen in Figure 5.5, the window centres are placed all the way out to the borders of the domain to be able to retrieve the velocity in these points. The rectangular shape leads to different resolution of k_x and k_y, which might cause problems in the algorithm. These problems appear only for the largest window sizes, which is when the proportions in x- and y-direction of the bordering windows deviates the most from each other. The same problem of instabilities in the windows close to the bottom edge of the domain is also apparent, but these point lies outside of the range of the surface PIV and can therefore be ignored in the analysis. Except for the top region where the window shapes are affected by the border the figures show a relatively good correspondence with the surface PIV, but again the CC method undercalculates the velocities.

6.2.2 Option 2

The streamwise surface velocity across the flow, $Ux(y)$, for Option 2, profile c), can be seen in figure 6.3, and for profile d) in figure 6.7. The reason the surface velocity profile for both profile c) and profile d) is included is that profile c) deviates from the trends and behaviours that profile a), b) and d) exhibit. Profile d) is therefore a good representative for the remaining profiles a) and b).

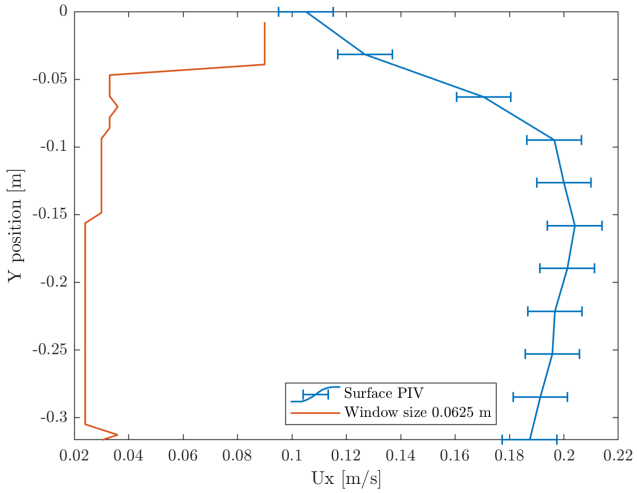

Figure 6.3: Option 2, profile c). $Ux(y)$, the spanwise surface profile of the streamwise velocity for a window size of $0.5 \cdot 0.0625$ m^2.

With the rectangular windows, the surface velocity profile for profile c) is close to constant across y, and shows no correspondence with the surface PIV. For the smallest window size of $0.0313 \cdot 0.0313$ m^2 Option 2 results in negative velocities across the flow. For larger window the velocity behaves approximately as in figure 6.3. Looking at the surface height matrix at t=1 for profile c) in figure 6.4, it appears as if the waves propagates along the diagonal, from the top right corner to the lower left corner. Increasing the length of the window will therefore not increase the time-space signal of the wave dispersion, as the wave will enter and exit the window in short diagonals rather than propagating along the whole length of the window. This combination of window shape and wave direction will give more information about the water surface than a square window of same height, but the additional data does not contribute to a better k_x-resolution and a more accurate dispersion relation fit. Instead the result is worse than for a square of same height.

Comparing the $\omega - k_x$ space for profile c) for Option 1 and Option 2 in figure 6.5, one can observe how the rectangular window greatly increases the resolution in k_x space. Both options have a horizontal band of noise for wave frequencies under 20 rad/s. For Option 1 a dispersion line is fitted along a line of slightly higher power, observed as a light green sections. In Option 2 the yellow dispersion line where the power is located is clearly visible for negative wavenumbers, but the black line marking the dispersion fit found by the CC method does not match with this. The incline of the dispersion line becomes steeper for negative wavenumbers and flatter for positive wavenumbers when the current velocity increase. From figure 6.5 it is therfore clear that the CC methods dispersion fit will yield too low velocities compared with the PIV. The reason why the CC method manages to locate the dispersion line for Option 1 but not for Option 2, when it is clearly visible in the frequency-wavenumber domain is not known. A possible explanation is that the algorithm does not handle the different resolutions in k_x and k_y space, even though the information of wave dispersion is perceived in frequency-wavenumber domain.

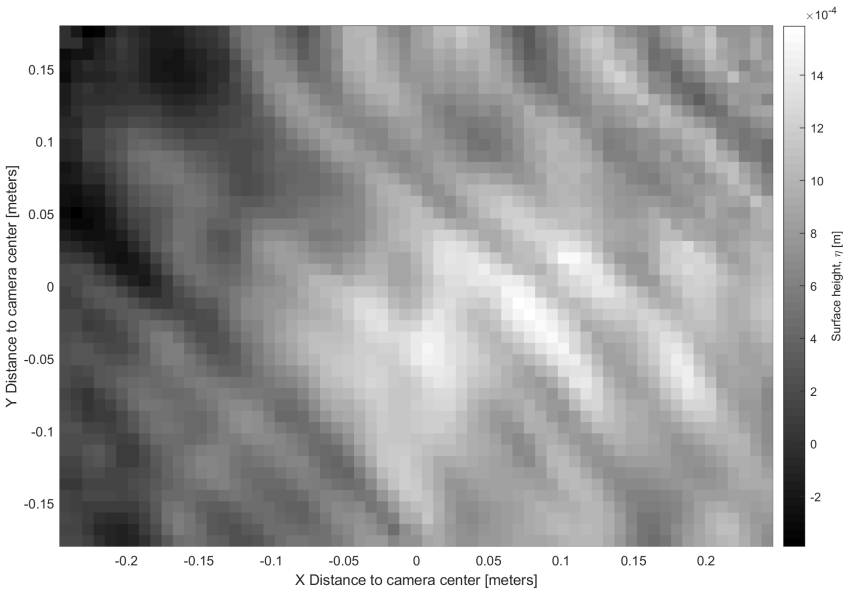

Figure 6.4: Surface height matrix for profile c). The diagonal lines are wave crests propagating from right to left.

Another explanation might be the noise, but as the level of noise is higher in Option 1 than in Option 2, this is unlikely the cause of the problem.

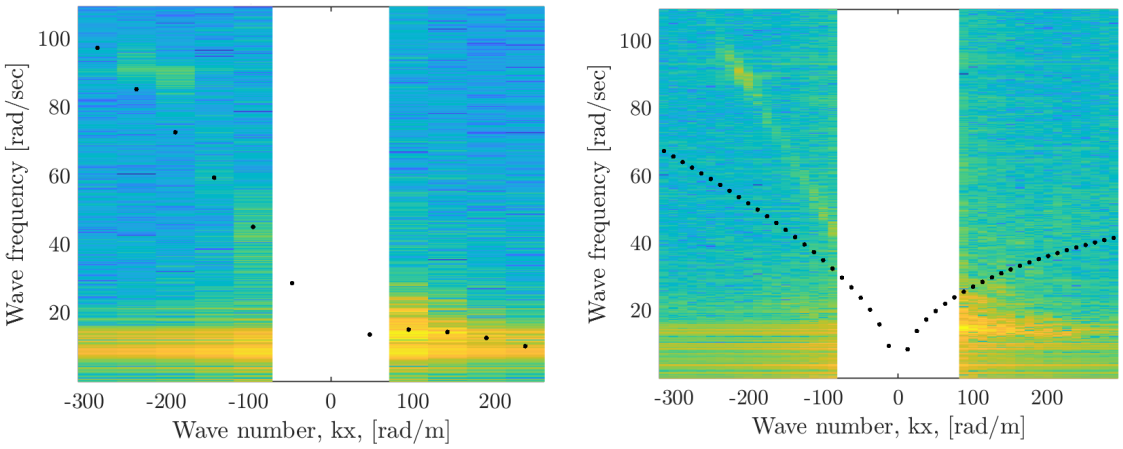

(a) Option 1.

(b) Option 2.

Figure 6.5: The frequency-wavenumber domain for Option 1 and 2 for profile c).

In figure 6.6 a zoomed in SNR density map of Option 1 and Option 2 is depicted. This reveals that rather than a well defined SNR density peak corresponding to a single pair of $[Ux\ Uy]$ there is a diagonal band of equally high SNR density values and wide range of solution for the streamwise and cross-flow velocities. Regardless of this, Option 1 still manages to do a reasonable fit, and no apparent explanation is found for this. Normally the shape of the SNR density peak is circular with higher values close to the centre, so even with a large area of high SNR densities, the centre is easily located. With the long and narrow shape of the SNR density peak, locating the peak becomes more difficult. The PEDM and EDM_{lin}

encounters the same problems with profile c) and Option 2, which is further discussed in section 6.4.

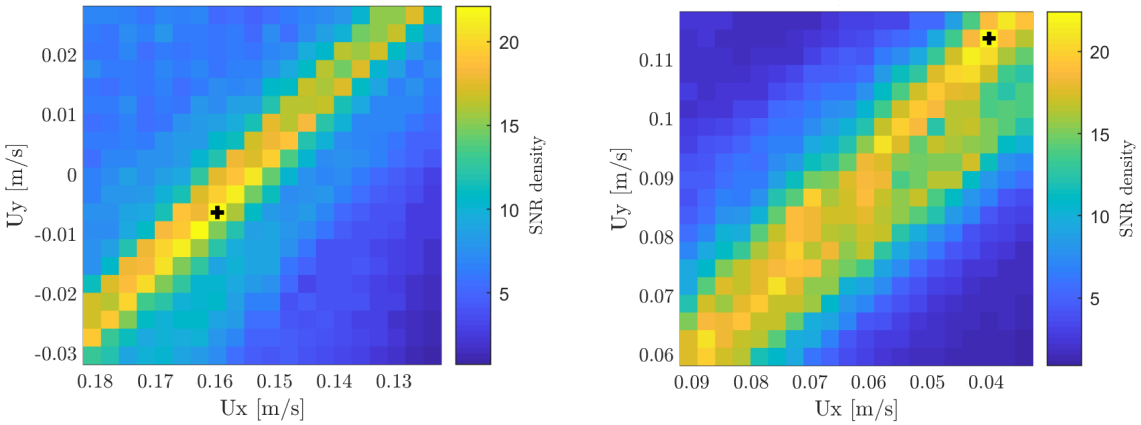

(a) Option 1.

(b) Option 2.

Figure 6.6: The SNR density map for Option 1 and 2 for profile c).

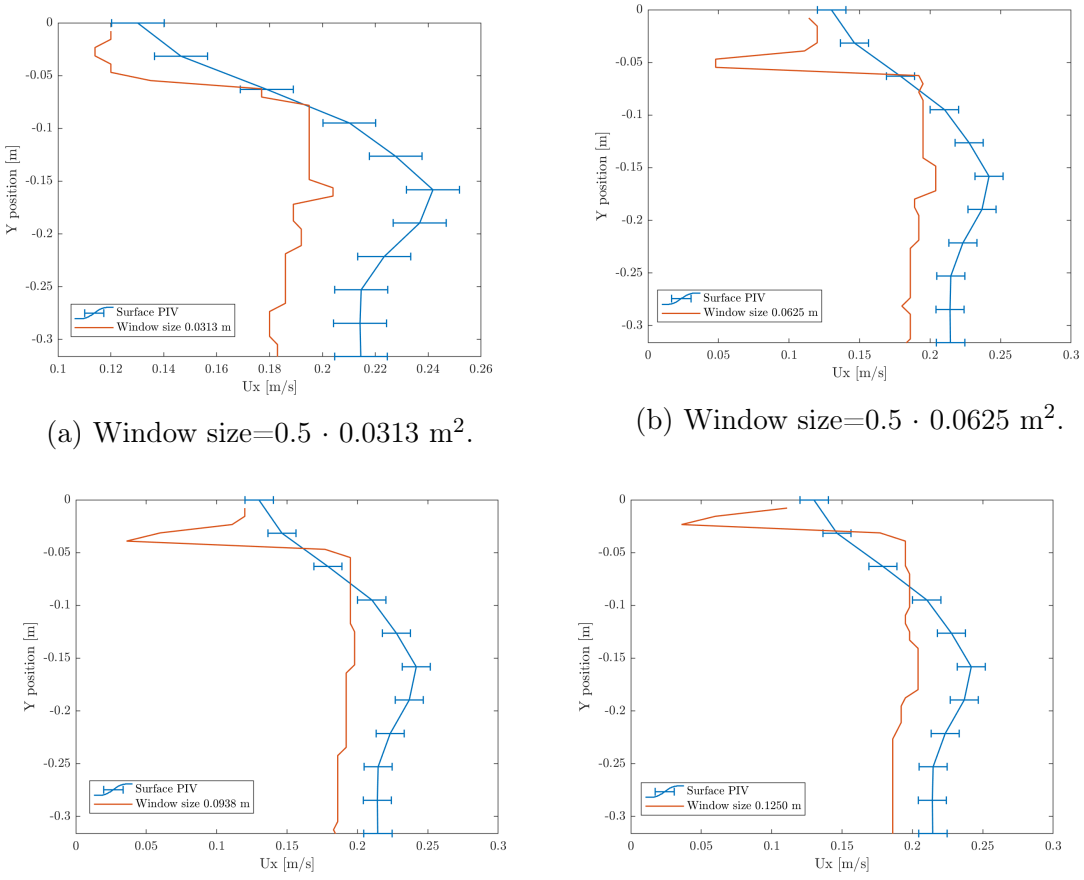

(a) Window size=$0.5 \cdot 0.0313$ m^2.

(b) Window size=$0.5 \cdot 0.0625$ m^2.

(c) Window size=$0.5 \cdot 0.0938$ m^2.

(d) Window size=$0.5 \cdot 0.1250$ m^2.

Figure 6.7: Option 2, profile d). $Ux(y)$, the spanwise surface profile of the streamwise velocity.

For the remaining profiles, represented by profile d) in figure 6.7, Option 2 yields

stable results. With this option the smallest window size manages to capture the large current gradient that takes place at the small y-values. The instabilities between bordering points in the y-direction that was observed for this window size for Option 1 is not present. This indicates that the increased length of the window contributes to capture a wider range of wavelengths such that the k_x resolution in the ω-k space is good enough to perform a precise dispersion line fit. For the larger window sizes, the windows affected by the upper boundary exhibit the same instability as for Option 1, with wither positive or negative peaks in the Ux velocity.

The frequency-wavenumber domain for profile d) can be seen in figure 6.8a. Here the dispersion line is visible for negative wavenumbers, and the black dispersion fit line from the CC method matches this. The black line located around k_x=-300 rad/m is due to the nyquist reflection of the 3D FFT causing the signal to be mirrored around the Fs/2, where Fs is the sample frequency. The line is therefore a continuation of the dispersion line going out of the frame at $k = 200$ rad/m. Similarly to profile c) there is an area of noise for frequencies lower than 20 rad/s, especially for positive wavenumbers, but it does not seem to affect the result of the dispersion fit algorithm. This contributes to pointing at the combination of the diagonal waves and the rectangular windows as the source of the poor results of profile c). The SNR density map for profile d) is depicted in figure 6.8b. Here the shape is more round, and the SNR maximization algorithm has managed to place the best fit for the velocities in the middle of the SNR density peak.

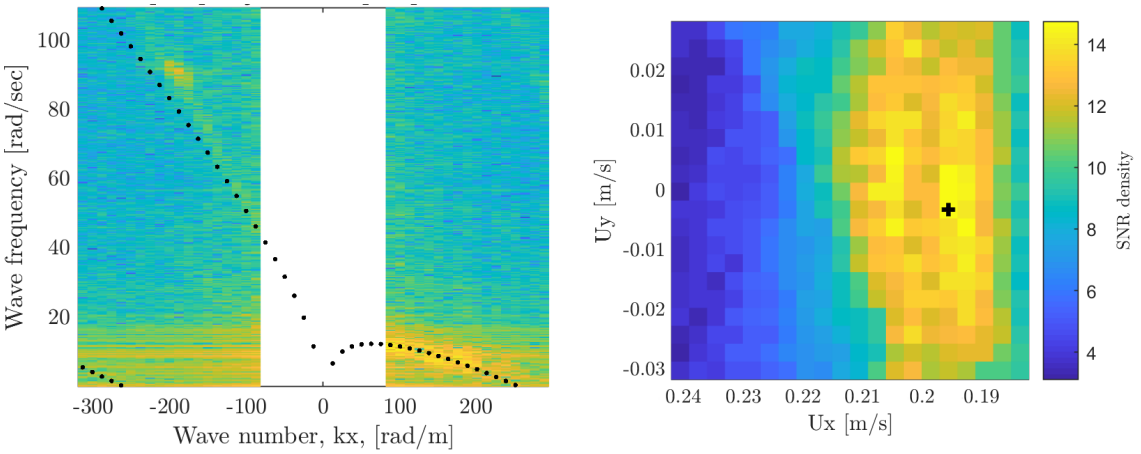

(a) Frequency-wavenumber domain

(b) SNR density map

Figure 6.8: The frequency-wavenumber domain and SNR density map for Option 2, profile d).

A common factor for the results of profile a), b) and d) with Option 2 is the lack of detail of the spanwise variation. Although the smallest window size manages to capture some of the variation, the larger windows derives an almost linear surface profile. The window size sensitivity is low, and for most window sizes it is only the windows affected by the upper and lower boundary that differs with window size.

6.2.3 Option 3

The surface profiles for Option 3, profile c) can be seen in figure 6.9. In Option 3 the velocity is averaged along the flow direction. This is done to mimic the surface PIV that is calculated as an average of the measured flow velocities along x. Any local variations along the flow in x-direction is smoothed out by the averaging. For this option the results of profiles a) -d) behaved similarly, and profile c) is again used to represent the other three profiles.

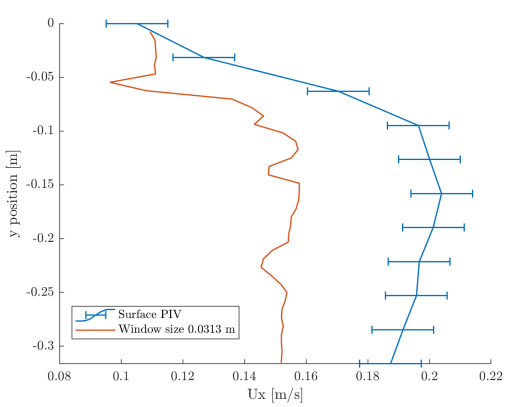

(a) Window size= 0.0313 · 0.0313 m^2.

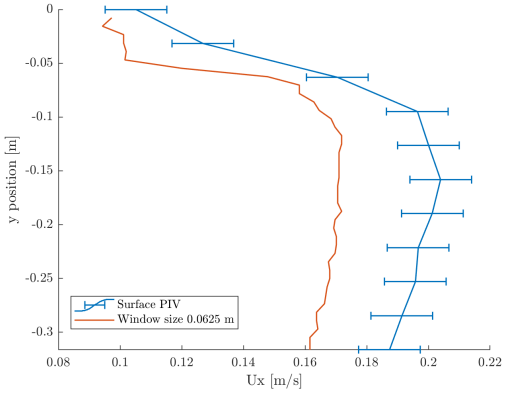

(b) Window size= 0.0625 · 0.0625 m^2.

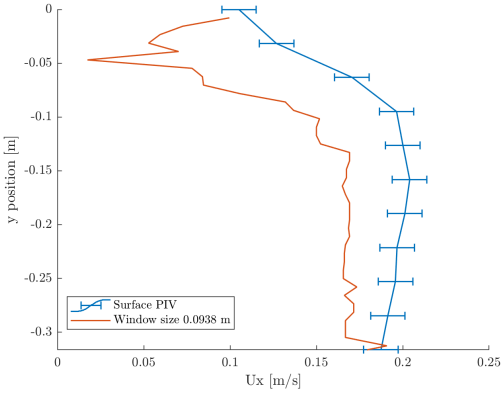

(c) Window size= 0.0938 · 0.0938 m^2.

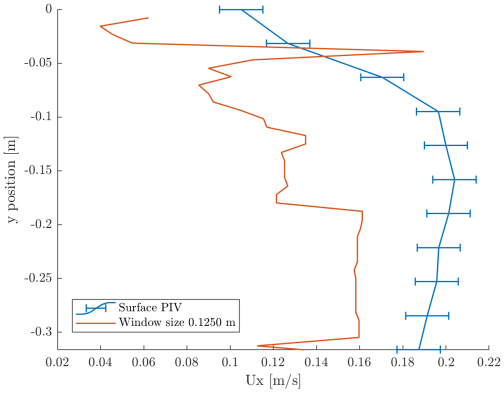

(d) Window size= 0.1250 · 0.1250 m^2.

Figure 6.9: Option 3, profile c). $Ux(y)$, the spanwise surface profile of the streamwise velocity.

The instabilities in y-diretion that was observable for the smallest window size in Option 1, figure 6.2a have been smoothed out with Option 3, figure 6.9a.

The averaged surface profile based on windows of 0.0625·0.0625 m^2 successfully manages to capture the shape of the surface PIV profile. No instabilities are experienced at the top boundary, and the large current gradients taking place between y=0 m and y=-0.15 m is captured with great detail. Although the shape of the surface current profile is correct, this option also underperforms the velocities. The underperformance is smallest in the partially blocked region of the flow, where the calculated velocities are approximately 1 cm/s under the lower

limits of the surface PIV error bars. In the open region the difference between the surface PIV and the CC method velocities is larger and the calculated velocities are approximately 3 cm/s under the lower surface PIV error bars.

Increasing the window size further results in instabilities at the upper and lower boundary, as can be observed in both figure 6.9c and 6.9d. The calculated surface profile also loses its smoothness and although the window size of 0.0938·0.0938 m^2 is closer to the surface PIV in the open region, the overall likeness of the calculated and measured surface profile is decreased. For the largest windows, the horizontal resolution is decreased because the windows cover regions with large current gradients, and the output velocity is an average of these varying current velocities.

Although Option 2 and Option 3 both analyses the whole length of the spatial domain, the results of Option 2 and Option 3 differs greatly. The difference between the two options is therefore solely caused by the consequences of different resolutions of k_x and k_y. With the square windows in Option 3, the variations across y is captured in greater detail, even though the resolution of the frequency-wavenumber domain for each window is lower than in Option 2. Whereas Option 2 showed little sensitivity to window size, Option 3 clearly shows that there is a balance between having too small windows and not enough surface information and too large windows where the horizontal resolution is smeared out. For all profiles a)-d) with Option 3), the windows of medium size exhibits the best similarity with the shape of the surface PIV.

6.2.4 Root-Mean-Square error

The Root-Mean-Square error (RMS error) was chosen as a means to evaluate the accuracy of the three different options of window placement. The RMS error, ΔU_{RMS} , between the $U_x(y)$ from the CC method and the surface profile over y measured by the surface PIV, $U_{x,surface\,PIV}(y)$ was calculated. The RMS error measures the spread of the calculated current velocities about the «truth» measurements of the PIV and is calculated with the following formula:

$$\Delta U_{RMS} = \sqrt{\frac{\sum_{i=1}^{n}(U_{i,x,PIV} - U_{i,x,CC})^2}{n}}, \tag{6.1}$$

which gives the spanwise-averaged RMS error of the streamwise velocity, $U_x(y)$. A low value of the RMS error indicates that there is a good correlation between the calculated values and the actual values. The RMS error is calculated separately for each window size between 0.0313 · 0.0313 m^2 and 0.1719 · 0.1719 m^2. For each window size there are 47 measuring points evenly spaced between y=0 and y=y_{max} where the current velocity is calculated in each point. However, the surface PIV profile across y is only measured at eleven points, so to be able to calculate the RMS error between the surface PIV and the calculated velocities only the eleven points of the CC velocities that corresponds to the y-locations of the surface PIV was used. This gave a summation over i=1 to n=11 in eq. 6.1. The spanwise-averaged RMS error of the streamwise velocity for each profile was then

plotted against increasing window size, and can be seen in figures 6.10.

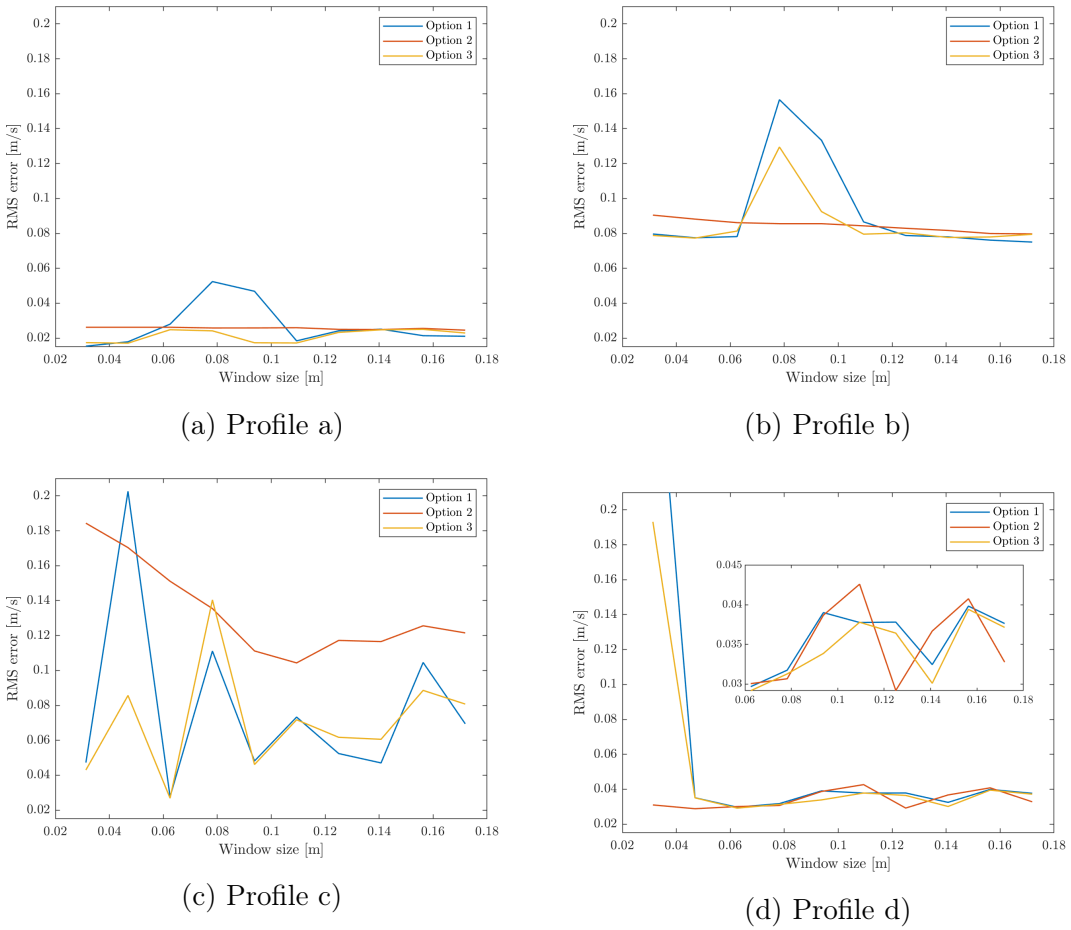

(a) Profile a)

(b) Profile b)

(c) Profile c)

(d) Profile d)

Figure 6.10: Spanwise-averaged RMS error of the streamwise velocity, $Ux(y)$

Option 1

Option 1 is based on a single column of square windows spanning across y at x=0. This option shows a sensitivity to window size, but the relationship between accuracy and window size differ between the profiles. For profile a) and profile b) Option 1 gives good accuracy for the smallest and largest window sizes, but experiences a large increase of the RMS error between windows of 0.06 m and 0.12 m. For profile c) the RMS error is large for the smallest windows and smaller for the larger ones. For profile d) the smallest window size of 0.313 m has a RMS error value of 0.32 m/s before it stabilizes at 0.035 m/s $\pm$0.01 m/s.

Option 2

All three options offer a low RMS error, but Option 2 with its rectangular windows stands out in that it is significantly less sensitive to the window size compared to Option 1 and 3. It is also the option with the highest stable RMS error for profile

a), b) and c). For each of the 47 windows, the same area as in Option 3 is analysed, but in Option 2 the whole area is analysed at once rather than analysing rows of squares in the x-direction and averaging over this. The output velocity is based on an average of the analysed waves of the whole length of the domain, offering a large area in the x-direction to analyse the dispersion. The length of the windows in the x-direction stays constant while the height of the windows in y-direction increases. The constant RMS error indicates that the increase in window height contributes little to the calculated velocity. Although Option 2 shows robustness regarding increasing window size the RMS error value is higher than for Option 1 and 3, giving results that deviates more from the surface PIV velocity for profile a), b) and c). For profile d) Option 3 offers approximately the same accuracy as Option 1 and 3, and for window sizes up to 0.06 m it even offers a much better accuracy.

The highest RMS error for Option 2 is found for profile c), in figure 6.10c. Here the RMS error lies between 0.18 m/s and 0.12 m/s, which is considerable higher than the RMS error for profiles a), b) and d) with Option 2. As mentioned in section 6.2.2 the waves in profile c) can be observed to move diagonally across the domain rather than the well-defined waves propagating in the x-direction that can be observed for the other profiles. For profile c) the rectangular windows in Option 2 does not give the waves a longer area to propagate and disperse in. Although more waves pass through the rectangular window than in a square window of same height, they pass the window across the same area as they would in a square window. These diagonal waves seem to be the cause of uncertainties and instabilities in Option 2 in profile c) as none of the other profiles yields the same type of unstable results and high RMS errors for Option 2.

Option 3

Option 3 yields much the same results as Option 1 and follows the same trends of how the RMS error varies with window size for all four profile, but at slightly lower values. Any local peaks at a x-location that might be present in the measurements at Option 1 is in Option 3 averaged over the whole length. When comparing only the match in shape between the CC method and the PIV surface profile, Option 3 offered the best fit for all four flow profiles. Due to the constant underperformance of the CC method, this likeness is not always reflected by the RMS error, but in figure 6.10, Option 3 is can be seen to offer the lowest RMS for many of the window sizes. Option 3 is the option with the largest numbers of windows, and in section 6.5 the consequence this has on the computational demand is discussed.

Although the RMS errors of Option 1-3 varies between the flow profiles, Option 3 yields the overall lowest result, and can be considered the best option. Option 2 is less sensitive to window size, but gives generally higher RMS errors than Option 1 and 3. Option 1 and Option 3 follows the same trends with regard to window size, but Option 1 have some RMS error peaks due to local variations along x. These variations are smoothed out with Option 3, resulting in lower peak values. Window sizes of 0.0625 m performs well for all Options in terms of the shape of the surface profile matching that of the surface PIV, but this similarity is not easily picked up

by the RMS error due to the constant underperformance of the CC method and the few PIV points over y. This is discussed in detail in the next section.

Shortcomings of the RMS error

There are two shortcomings of basing the RMS error on fewer points than the actual points of the calculated velocities. The first is that the RMS error is not able to pick up the variations of the calculated velocities between these points. As can be seen in figures 6.2, 6.7 and 6.9 there is a large variation of the smoothness of the calculated curves. It varies both with the different window sizes within an option, and more notably it varies between Options 1-3 . The line between the measuring points of the surface PIV is smoot, but there is no information about the actual velocity in these points. A reoccurring trend with the calculated current velocities is that they underperforms compared to the surface PIV, measuring constantly lower velocities. A calculated surface profile that greatly resembles the shape of the surface PIV can have a higher RMS error than an unstable jagged line of higher velocity but with small resemblance to the shape of the actual surface velocity profile.

The other problem arises in the area of high current gradients behind the curved mesh. The velocity is significantly smaller close to y=0 for all profiles a)-d). In this area some of the window sizes have trouble computing a good current velocity fit, and large deviations of $U_x(y)$ where the velocity either significantly increase or decrease can often be seen for small y-values. A curve that follows the overall shape of surface PIV for most measuring points might get a high RMS error if it deviates from the lower surface velocity close to y=0, especially if the calculated velocity increase when the measured velocity decrease.

The problem of unstable velocities for small y-values have two possible explanations. The first one is that the algorithm struggles to perform a good dispersion relation fit when the current gradient is large within the analysed area. The second explanation is related to the handling of the borders, where the windows close to y=0 and y=y_{max} loses its square shape in order to be able to get measuring points close to the edge. At the bottom the velocities are calculated over the whole measuring domain to y=-0.3596 m but the surface PIV spans 4 cm shorter and stops at y=0.3162. If the calculated velocity becomes unstable for large y-values, it will therefore not affect the RMS error. Because the problem of unstable border values mostly arises at the top around y=0 and very seldom at the bottom at y=y_{max}, it is most probable that it is the large current gradient that causes the problem. Ideally the area of the large current gradients should have been located closer to the middle of the measuring domain, so that this could have been investigated closer without having to take into consideration that the windows changes shape.

6.2.5 Spanwise velocity component

The mean flow in the y-direction was expected to be zero, and no surface PIV measurement was done for the spanwise velocity, Uy.

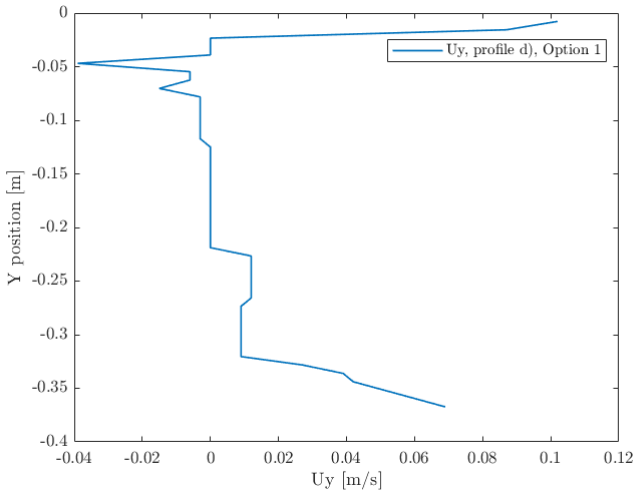

Figure 6.11: Spanwise surface profile of the spanwise velocity, $Uy(y)$.

Results from the CC method yielded Uy values close to 0 m/s, as can be seen in figure 6.11. The figure shows the spanwise velocity profile for Uy for profile d), Option 1 for a window size of $0.0938 \cdot 0.0938$ m^2. The $Uy(y)$ values for the other profiles yielded much the same results. Similarly to the streamwise velocity, the spanwise velocity exhibit a sensitivity to the window size and shape close to the boundaries of the domain, where the velocities peaks. Based on previous analysis of the Ux component, this increase in velocity can be assumed to be due to both the shape and the decreased size of the windows in this areas, and results from this upper and lower boundaries are assumed to not represent the actual current. Ignoring the values affected by the boundaries, the average y-component of the surface velocity was 0 ± 1 cm/s for all flow profiles, and the assumption of no spanwise velocity component holds.

6.3 Identification of effective depth

Although the shape of the spanwise velocity profiles derived with the CC method roughly matches the shape of the surface velocity profile measured by the surface PIV, the derived velocities for all flow profiles a)-d) are lower than the measured surface velocity, as can be seen in figures 6.2, 6.3 and 6.9. The dispersion lines, for example in figure 6.8a, indicates that the dispersion fit of the CC method and the observable dispersion line in the signal matches. This indicates that it might be the observed signal itself that is lower than the surface PIV, and not the CC method that underperforms. The difference between the calculated velocity and the surface PIV velocity varies both between profiles a)-d) and with the window size.

The PIV measurements in Figure 6.12 reveals that there is a significant amount of vertical shear in the flow, both behind the blockage at position 1, and in the open region, position 2. For all profiles, the velocity is highest at the surface and decrease with the depth. The shear in position 1 for all profiles is close to linear, suggesting that the curved wire mesh inserted between the honeycomb structures at this side of the tank successfully manages to distort the streamlines and produce a uniformly sheared flow with a flow profile of peak velocity at the surface, and velocity decreasing with depth. The shear in position 2 is non-linear with a logarithmic shape. In the middle layer of the water column, at 1.5 cm to 3 cm depth the velocities at position 1 and 2 is within the same range. For the upper layer close to the surface the velocities at position 2 experiences a large current gradient with the velocities increasing towards the surface. The vertical shear in the flow might hold the explanation of the constant undercalculations of the CC method velocities.

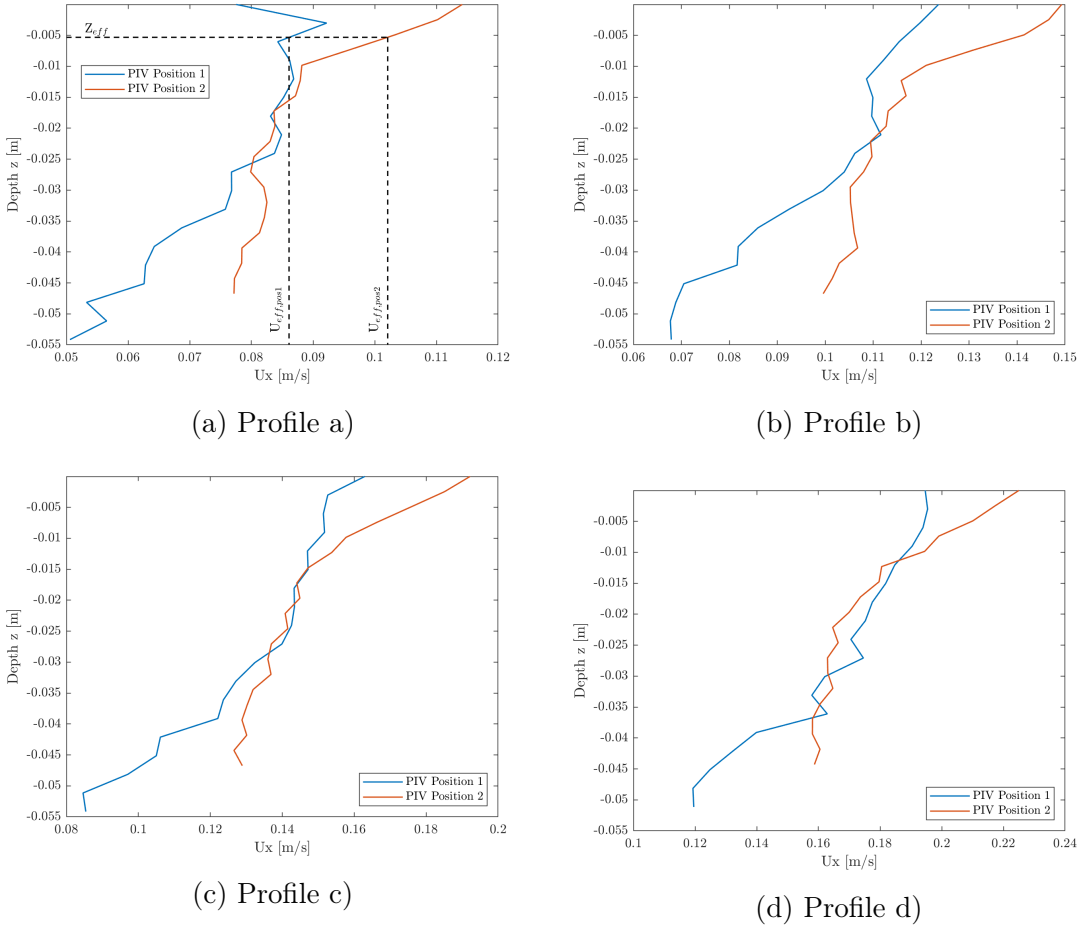

(a) Profile a)

(b) Profile b)

(c) Profile c)

(d) Profile d)

Figure 6.12: PIV measurements at position 1 and 2 for profiles a) to d). All PIV measurements have an uncertainty of ± 1 cm/s. In a) the effective depth, Z_{eff} and the corresponding velocities at the effective depth at position 1 and 2, $Ux_{eff,pos1}$, $Ux_{eff,pos2}$ is included.

The Copter Currents algorithm is based on the assumption that the flow has a uniform depth-profile with no vertical shear and calculates a 'surface velocity'

which in reality is a weighted average of the velocities at different depths, rather than the actual surface velocity. From figure 6.12 it becomes clear that the assumption of a uniform current profile does not hold. Because of the of vertical current shear in the flow, the assumption of a uniform current profile and the linear fit used in the dispersion relation in Eq. 3.10 results in the wavenumber-independent bulk velocity introduced in section 3.3. The underlying currents exert a bulk effect on the waves. This calculated bulk velocity lacks information about vertical shear in the flow, but it is still useful to supply a first-order current estimate. With shear increasing towards the surface, the bulk velocity will necessarily be lower than the actual surface velocity, which explains why the velocities derived with the CC method is consistently lower than the surface PIV.

In order to determine how the calculated CC velocity is related to the depth-profile, the velocity is compared both to the average depth velocity and the velocity at the effective depth. By first taking the un-weighted average over the depth of the PIV measured $U_x(z)$ at position 1 and 2, $Ux_{DepthAve}$, and comparing with the 'surface velocity' from CC at the same locations, there is already a much better match between the average $U_x(z)$ and the calculated surface velocity $U_x(y = position\ 1,\ position\ 2)$. This applies to all four profiles. The depth averaged flowwise velocity at position 1 and 2 can be seen in Figure 6.14 together with the surface PIV and the CC velocity from Option 3 for a window size of 0.0625 m. Beacuse the depth-averaged velocities are derived from the PIV measurements that has an uncertainty of $\pm$ 1 cm/s the depth-averaged velocities are assumed to have the same uncertainty. For profile c) the CC velocity at position 1 and 2 is within the error bars of the depth-averaged velocity. For the other profiles the CC velocity at position 1 is within the depth-averaged velocities error bars. This region around position 1 is also the region where the CC velocities are closest to the surface PIV velocities. All depth averaged streamwise velocities at position 1 and 2 for profiles a)-d) can be seen in Table 6.2.

The next step is to identify the dominant wavenumber in profiles a)-d) and to use this to calculate the effective depth, Z_{eff}. As explained in Section 3.3.1, the measured dominant wavenumber can be used to calculate the effective depth of the flow, which is the depth of the calculated current velocity when using the Stewart and Joy approximation in Eq. 3.11. The effective depth will be the depth that is weighted toward when the weighted average velocity is calculated. For a linear current profile, as it is assumed in CC, the effective depth for each profile can be calculated using the formula for the linear effective depth, Eq. 3.14. The wavemaker creates waves of different wavelength through a Gaussian wave field, and the wavelength that is most often observed corresponds to the dominant wavenumber. This can be identified from figure 6.13 where the dominant wavenumber is located at the highest values of the averaged angular frequency, ω. If there is a range of dominant wavenumbers rather than a single value, the dominant wavenumber is calculated as the average of these values. Figure 6.13 shows both the spanwise and flowwise wavenumbers, k_y and k_x. For calculations of the flowwise velocity and flowwise Effective depth the k_x is to be used. All peak values of ω is located at positive k_x-values, indicating that the x-component of the

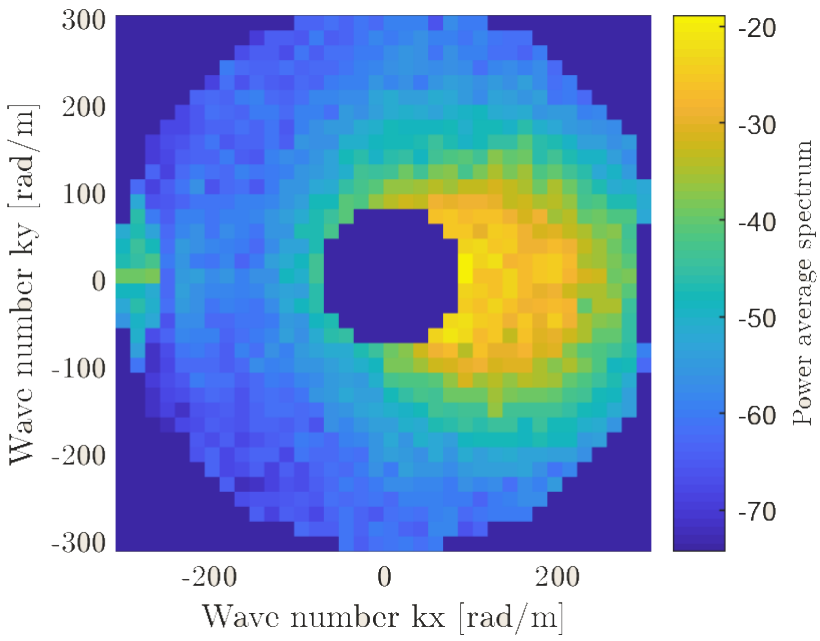

Figure 6.13: The averaged ω, k_x, k_y domain for profile a). The dominant wavenumbers are found in the yellow area with high average power. The dark blue circle in the middle of the domain is values of k_x and k_y that lie outside of the defined wavelenght limits used in the calculation.

waves propagates solely in the positive x-direction. Dominant wavenumbers, corresponding wavelength and effective depth for all profiles can be seen in Table 6.1.

Table 6.1: Dominant wavenumbers and corresponding Linear Effective Depths

Profile	Dominant k_x[rad/m]	Dominant λ [m]	$Z_{eff,lin}$ [mm]
Profile a)	94.22	0.067	-5.31
Profile b)	106.8	0.059	-4.68
Profile c)	81.66	0.077	-6.12
Profile d)	73.38	0.082	-6.81

The effective depth lies between -4.68 mm and -6.81 mm under the surface for the four profiles. The velocities at the effective depth, $Ux_{eff,pos1}$, $Ux_{eff,pos2}$ can be found at depth Z_{eff} in the PIV measurements at position 1 and 2, as shown in figure 6.12a. The effective depth velocities from the PIV can be seen in Table 6.2.

Figure 6.14 shows the surface PIV, the depth-averaged velocities $Ux_{DepthAve,pos1}$, $Ux_{DepthAve,pos2}$ and the effective depth velocities $Ux_{eff,pos1}$, $Ux_{eff,pos2}$ together with the CC velocity from Option 3 for a window size of 0.0625 m. At position 1 all profiles matches the depth-averaged velocity and the CC velocity is closer to the surface PIV than at position 1. The PIV at position 1 in figure 6.12 shows that there is less shear close to the surface due to the linear shear profile created by the curved mesh, thus the difference between the effective depth velocity and the

Table 6.2: Velocity at the effective depth and the depth averaged velocity based on PIV measurement.

Profile	$U_{eff,pos\,1}$[m/s]	$U_{eff,pos\,2}$[m/s]	$U_{depthAve,pos\,1}$[m/s]	$U_{depthAve,pos\,2}$[m/s]
Profile a)	0.0861	0.1021	0.0743	0.0868
Profile b)	0.1173	0.1419	0.0967	0.1154
Profile c)	0.1514	0.1712	0.1298	0.1468
Profile d)	0.1930	0.2016	0.1643	0.1772

surface PIV will be smaller. This might explain why there is a better match between the CC velocity and the surface PIV at position 1 than there is at position 2. At position 2 all profiles except profile a) is within the uncertainty range of the effective depth velocity, $Ux_{eff,pos2}$. Even profile b) which has almost a 50% deviation between the surface PIV and CC velocities shows a good correspondence between velocity at effective depth and the CC velocities at both positions, which supports the theory that the CC velocities corresponds to the velocity at the effective depth.

Due to the strong vertical shear in the flow, the weighting of the velocities towards the effective depth leads to the undercalculation that can be observed for all datasets. The reason for the varying degree between the datasets can be linked to the dominant wavenumbers and the amount of vertical shear in the flow. A small dominant wavnumber corresponds to a deeper effective depth. A larger vertical shear means that the velocity decrease more rapidly with increasing depth than a velocity profile with less shear. The fact that the PIV velocities at the effective depth shows a good correlation to the calculated velocities indicates that the reason for the undercalculation is linked to the large amount of vertical shear and the weighing towards the effective depth, rather than simply being due to an actual undercalculation caused by an rounding error in the CC algorithm. Further investigations to confirm this theory could be done by comparing velocities derived from Copter Currents with a uniform flow profile with no vertical shear and see if there is a better match or to create a shear that increase with depth to see if this leads to a similar overcalculation.

Another point worth noting about the shear in the flow is that there appears to be close to no change in horizontal shear with depth. If the output velocities from Copter Currents is the velocities a small depth beneath the surface, the velocity profile still keeps the same shape as at the surface, only at a slightly lower magnitude.

This section has shown that in flows with large amounts of vertical shear the assumption of an uniform current profile leads to deviations from the surface velocity due to the approximations of Stewart and Joy in Eq. 3.11 that weights the velocity towards the effective depth. To deal with the effect of vertical shear in the flow a depth-dependent inversion method can be applied. Both the PEDM and the EDM can be used to estimate near-surface shear currents and might offer a more accurate estimate of the surface velocity than the CC method.

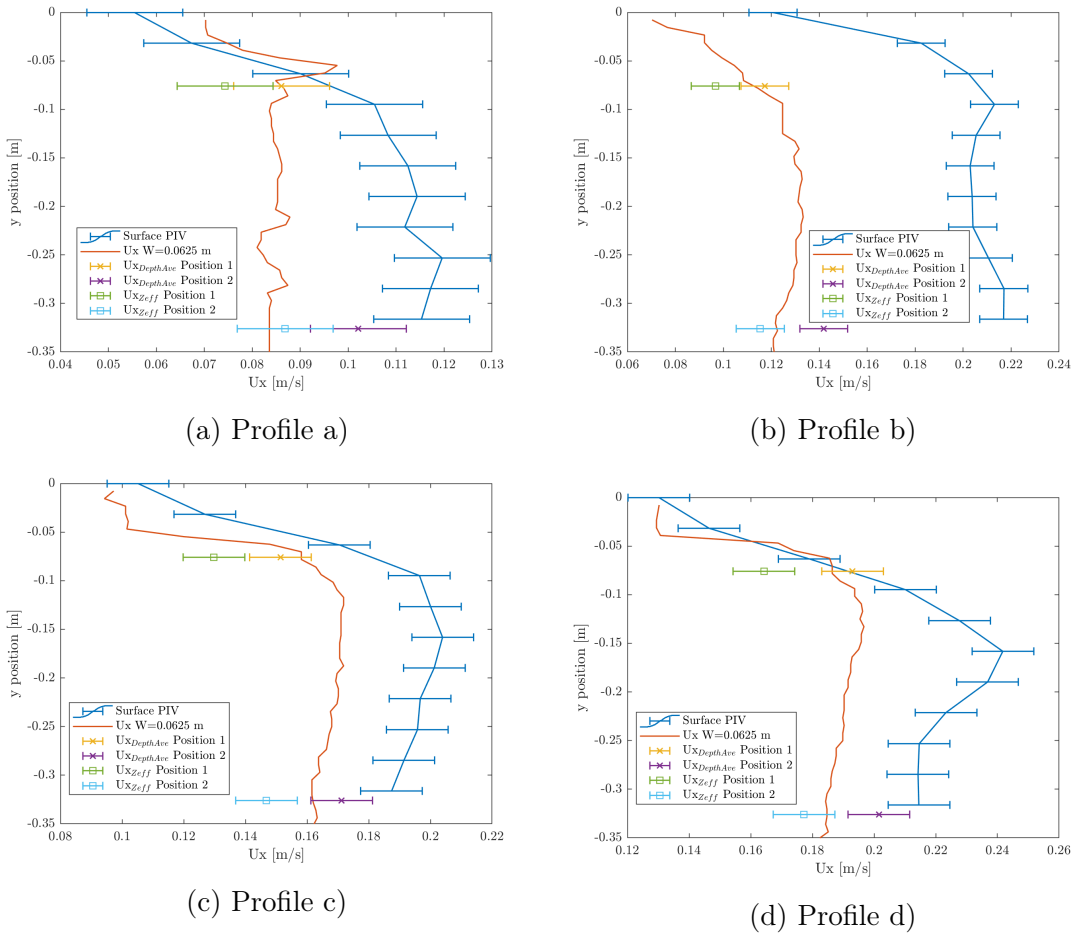

(a) Profile a)

(b) Profile b)

(c) Profile c)

(d) Profile d)

Figure 6.14: Streamwise $Ux(y)$ with the velocity at the effective depth and the depth-averaged velocites at PIV position 1 and position 2 for profiles a)-d), Option 3.

6.4 Surface Velocity, PEDM and EDM$_{lin}$

This section will present and discuss the surface profiles calculated with the PEDM and EDM$_{lin}$ for Option 1, 2 and 3. From section 5.2.1 it became apparent that the PEDM and EDM$_{lin}$ have different requirements for the wavelength limits than the CC method. To better be able to compare the three methods, a second set of velocities for the CC method has been included in this section, run with the same calculation parameters as the PEDM and EDM$_{lin}$ in Table 5.4 . Again, profile c) is representative of the behaviour and trends of all four profiles a)-d), if nothing else is stated. The minimum possible window size for the PEDM and EDM$_{lin}$ is larger than for the CC method, and so the surface profiles plotted for Option 1-3 depicts different window sizes than the ones presented in section 6.2 for the CC method.

6.4.1 Option 1

The results of the surface profile derived with the PEDM, EDM$_{lin}$ and the CC method for four of the window sizes can be seen in figure 6.15.

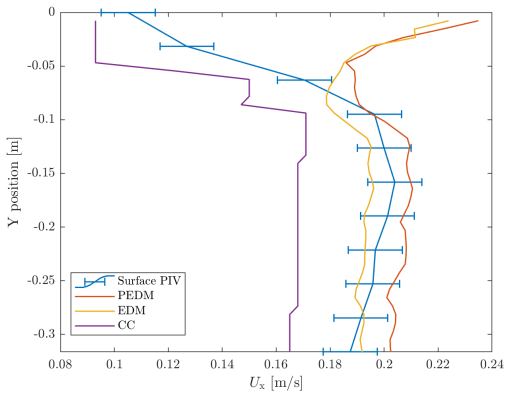

(a) Window size= 0.0625 · 0.0625 m^2.

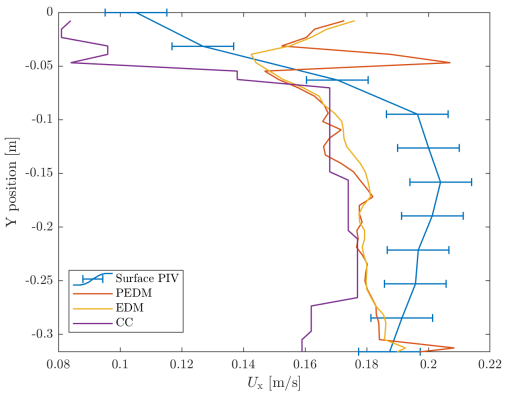

(b) Window size= 0.0938 · 0.0938 m^2.

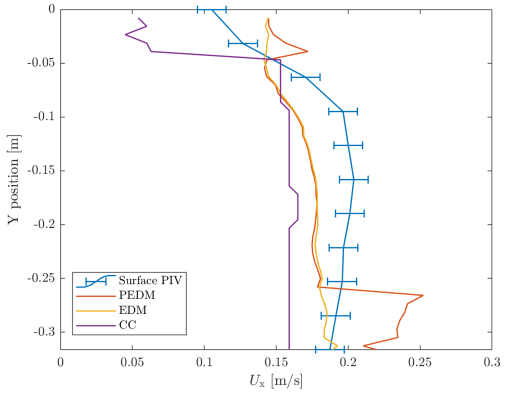

(c) Window size= 0.1250 · 0.1250 m^2.

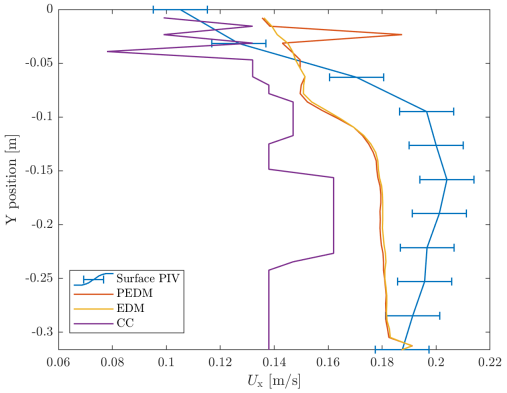

(d) Window size= 0.1563 · 0.1563 m^2.

Figure 6.15: Option 1, profile c). $Ux(y)$, the spanwise surface profile of the streamwise velocity.

In figure 6.15a both the EDM$_{lin}$ and PEDM gives results that are within the surface PIVs errorbars for most of the domain. The exception to this is from y=-0.05 m, where both methods deviate from the surface PIV with velocities increasing towards y=0 m. The points where the velocities increase all belongs to windows affected by the boundary, where the window shape becomes rectangular rather than square. The velocity from the CC method manages to capture the large current gradient that takes place between y=0 m and y=-0.15 m, even in the windows affected by the boundaries. Although the current gradient is captured, the CC velocities are significantly smaller than the surface PIV, and there is a lack of detail to the surface profile compared to the surface PIV and the PEDM and EDM.

In figure 6.15b the performance of the PEDM and EDM$_{lin}$ is less accurate. The velocities underperform for most of the domain and the similarity in shape with the surface PIV is reduced. With increasing window size, a larger part of the domain is affected by the upper and lower boundary. This is observed both for small y-values close to zero and close to y=-0.3 m.

The SNR density map of PEDM and EDM$_{lin}$ for profile c) for wavenumber 100

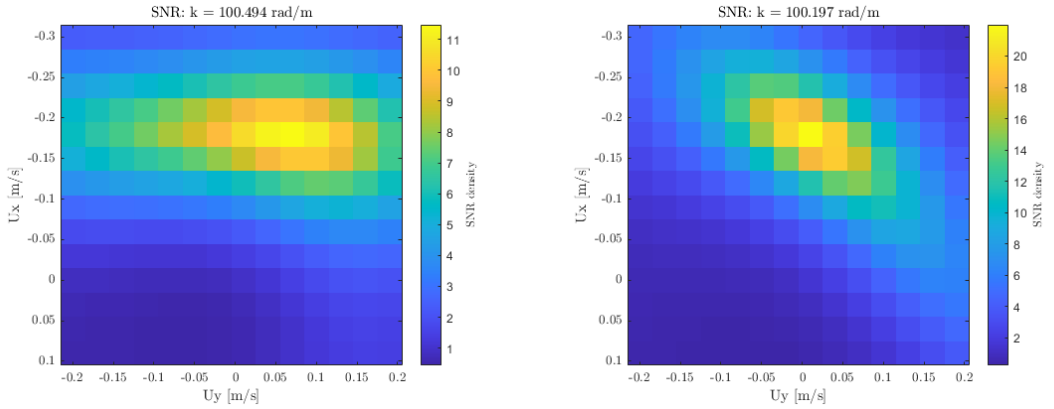

(a) Window size= $0.0625 \cdot 0.0625$ m^2 (b) Window size= $0.1563 \cdot 0.1563$ m^2.

Figure 6.16: SNR density map for wavenumber 100 rad/m for a window size of $0.0625 \cdot 0.0625$ m^2 and of $0.1563 \cdot 0.1563$ m^2. The SNR density is higher for the largest window.

rad/m for a window size of $0.0625 \cdot 0.0625$ m^2 and $0.1563 \cdot 0.1563$ m^2 can be seen in figure 6.16. The level of noise can be seen to decrease with increasing window size, resulting in higher SNR density for the largest window. Even though the signal strength is higher for the largest window, the accuracy of the surface profile is lower for this window size. While the SNR is a measure of precision and a clear signal is desirable, it does not necessarily contribute to better accuracy. The SNR density map of the PEDM and EDM$_{lin}$ corresponds to the signal of a single wavenumber, whereas the SNR density map of the CC method corresponds to a signal averaged over all wavenumbers. With strong vertical shear towards the surface, the SNR density peak of the PEDM and EDM$_{lin}$ will move as the velocity increases with increasing wavenumbers.

6.4.2 Option 2

When running Option 2 with the rectangular windows spanning the whole length of the domain with the PEDM and EDM$_{lin}$ included in the Copter Currents toolbox, a problem of low SNR density arose for profile c) and d). While profile a) and b) ran without problems with the simulation parameters in Table 5.4, profile c) and d) would not compute. For the smallest window size of 0.0469 m one additional peak of high SNR density was observed in the lower left corner of the SNR density, Ux, Uy plot, even though the SNR density was above the set SNR density threshold of 2. As the wavenumber increased, the main peak stared to spread out and form a diagonal line, as can be seen in figure 6.18. The small peak in the lower left corner and the diagonal line with constant high SNR density values resulted in ambiguous Doppler shift velocities covering several solutions of the best fit of $[Ux, Uy]$. This gave a non-unique polynomial with a degree larger than the number of data points, and no curve fit could be executed.

By increasing the minimum window size to 0.0625 m for profile c) and d) the algorithm would run, and a well-defined peak with a high SNR density value could

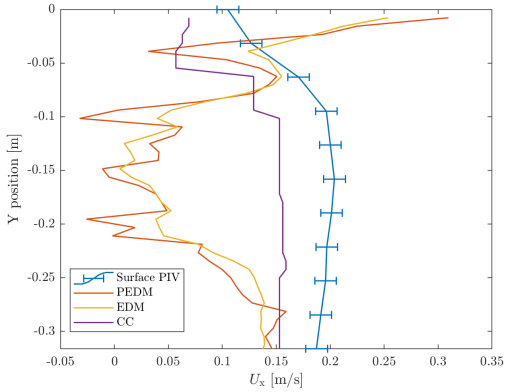

(a) Window size=$0.5 \cdot 0.0625$ m^2.

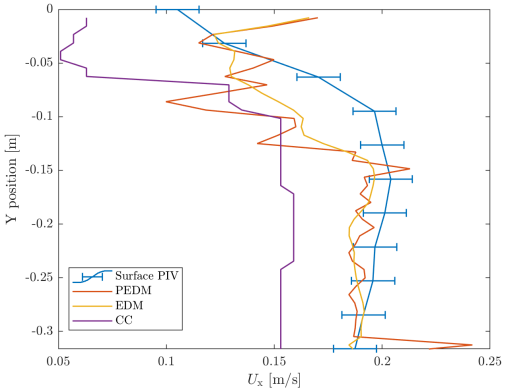

(b) Window size=$0.5 \cdot 0.0938$ m^2.

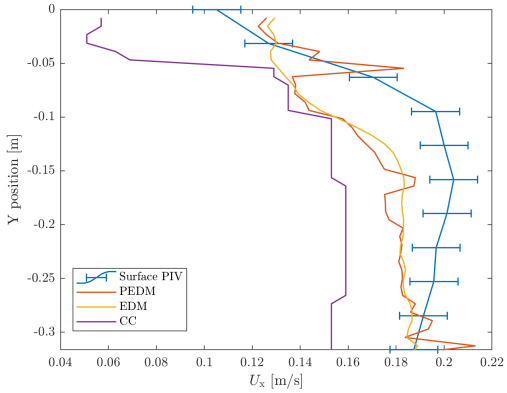

(c) Window size=$0.5 \cdot 0.1250$ m^2.

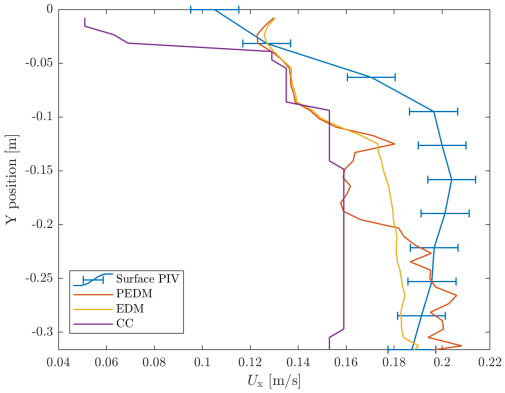

(d) Window size=$0.5 \cdot 0.1563$ m^2.

Figure 6.17: Option 2, profile c). $Ux(y)$, the spanwise surface profile of the streamwise velocity.

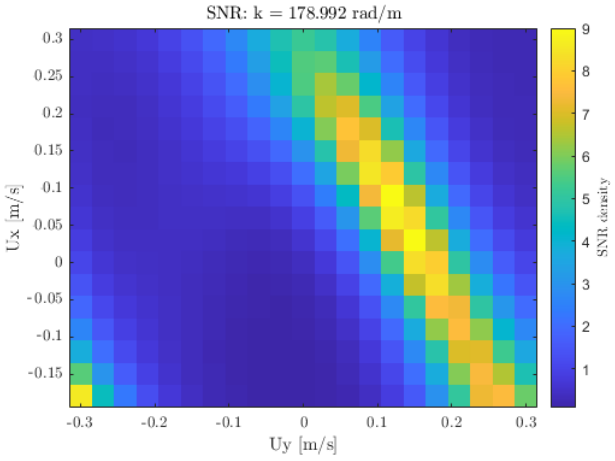

Figure 6.18: SNR density map for Option 2, wavenumber 178 rad/m. A peak of noise is observed in the lower left corner, and the velocities are placed somewhere along the diagonal SNR peak.

be observed for the lowest wavenumbers. The resulting surface velocities can be

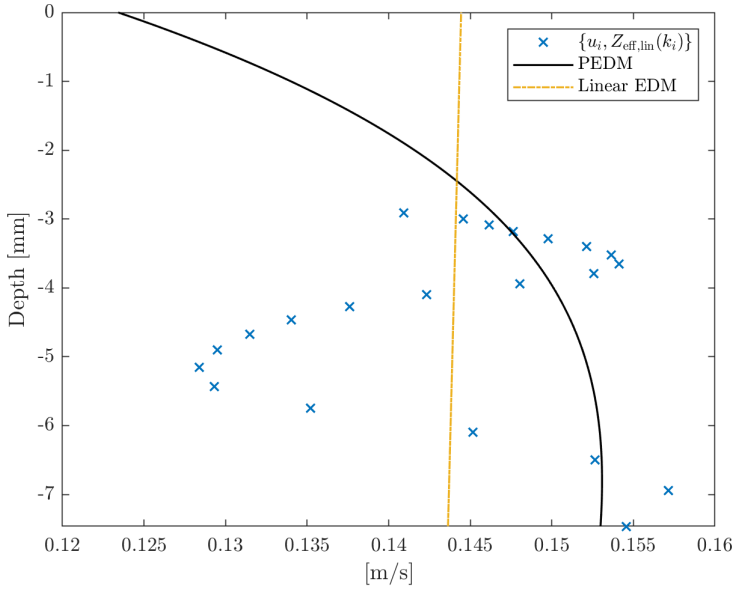

Figure 6.19: The mapped Doppler shift velocities, derived from a SNR density map with a long, diagonal peak, can be seen to vary greatly with depth. The linear curve of the EDM$_{lin}$ is fitted in the middle of these points whereas the PEDM tries to do a polynomial fit based on the Doppler shift velocities.

seen in figure 6.17. However, as the algorithm analyzed higher ks, the SNR density decreased, and the peak started to spread out. This was especially notable in profile c), where the peak once again spread out to form a diagonal line similar to that in figure 6.18, and a peak in the lower left corner would appear. The reason that the algorithm would run with the larger window size even though the same disturbances were observed in the SNR density, Ux, Uy plot might be that the well-defined single peak that appeared for low wavenumbers were enough to secure a unique polynomial fit, even with the disturbances for the high wavenumbers. Profile c) was also the profile that experienced the worst fit with of the surface profile $Ux(y)$ with Option 2 for the CC method, but the CC method was still able to compute the velocity vector with a SNR density above the SNR density threshold.

Figure 6.19 shows the mapped Doppler shift velocities,$\{\tilde{c}, Z_{eff,lin}(k)\}$, for a window size of 0.0938 m for profile c). This gives the velocities of the PEDM and EDM$_{lin}$ located at y=-0.1m in figure 6.17b. The Doppler shift velocities span a wide range of velocities rather than fitting along a defined current profile. The reason for the great variation of velocity between the depths might be SNR density map. For Option 2 and profile c), the peak in the SNR density map becomes a long diagonal line, as seen in figure 6.18. If the Doppler shift velocities derived from this plot is placed at a different location along this diagonal SNR-peak for each wavenumber, it might result in something similar to figure 6.19. When the EDM$_{lin}$ makes a linear fit based on these points, the resulting surface velocity is approximately in the middle of the range of the Doppler shifts velocities. The PEDM on the other hand tries to find a polynomial fit based on the points, and ends up with a much lower surface velocity than the EDM.

6.4.3 Option 3

The surface profile for Option 3, profile c), can be seen in figure 6.20. Similarly to Option 1, the best result of the four plotted window sizes is achieved for the window size of $0.0625 \cdot 0.0625$ m^2. The PEDM and EDM$_{lin}$ is both within the PIV error bars for most of the cross section, the only exception is in the region around y=0 m where the window shapes are affected by the upper boundary. The lower boundary is outside of the y-range of the surface PIV and does therefore not affect the lower windows for the smallest window sizes. The surface profile for the PEDM and EDM$_{lin}$ is very similar for Option 1 and Option 3, and offers little to no improvement, whereas Option 3 contributes to a smoother and more detailed surface profile for the CC method, as is discussed is section 6.2.3. The surface profile from the CC method manages to successfully capture the exact shape of the surface PIV, even the large velocity gradient between y=-0.1 m and y=0 m, but with overall lower velocities.

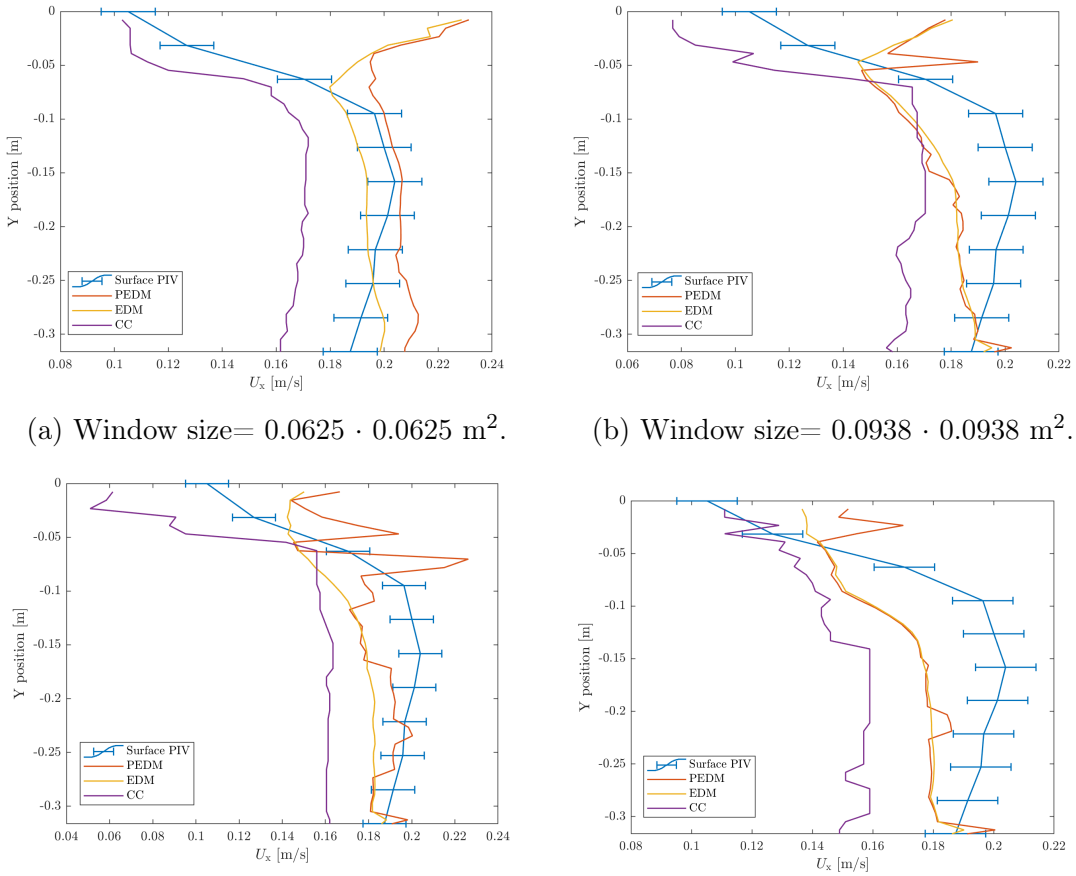

(a) Window size= $0.0625 \cdot 0.0625$ m^2.

(b) Window size= $0.0938 \cdot 0.0938$ m^2.

(c) Window size= $0.1250 \cdot 0.1250$ m^2.

(d) Window size= $0.1563 \cdot 0.1563$ m^2.

Figure 6.20: Option 3, profile c). $Ux(y)$, the spanwise surface profile of the streamwise velocity.

When the window size is increased, the PEDM and EDM$_{lin}$ surface profiles start

to deviate from the surface PIV, with lower velocities. The curve of the EDM$_{lin}$ remains smooth whereas the PEDM curve loses its smoothness in figure 6.20b and 6.20c. These large changes in velocities for adjacent y-values are not present in Option 1, where the PEDM and EDM$_{lin}$ followed the same line for all window sizes. In figure 6.20d the curve of the PEDM is smooth again, and matches up with the EDM. The surface profile of the CC method gradually loses its resemblance to the surface PIV profile when the window size increases.

6.4.4 Root-Mean-Square error

The spanwise averaged RMS error was calculated for all four profiles using Eq. 6.1. Due to the unsteady nature of the windows at the borders, these windows were omitted from the calculation of the RMS-error. The RMS error for all three inversion methods for profile c) with Option 1-3 can be seen in figure 6.21.

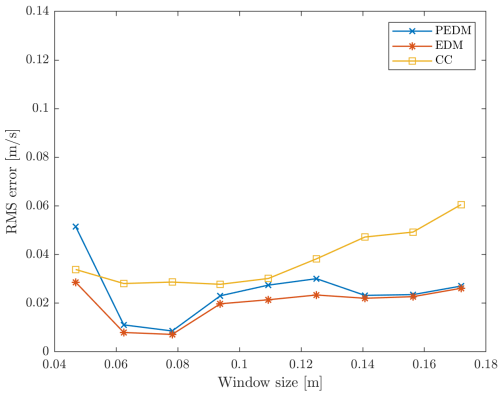

(a) Option 1

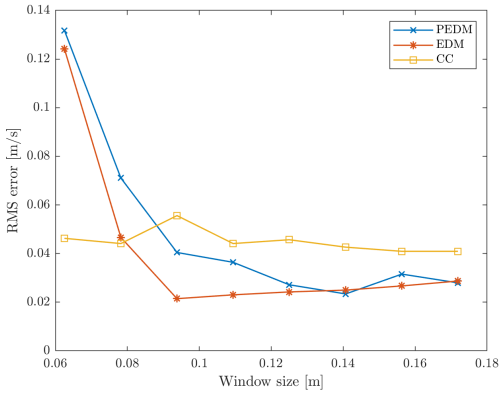

(b) Option 2

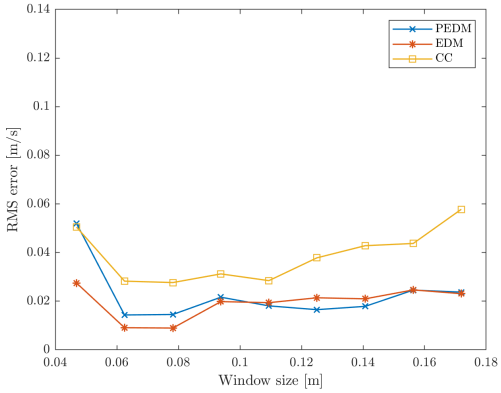

(c) Option 3

Figure 6.21: Spanwise-averaged RMS error of the streamwise velocity, $Ux(y)$ for profile c).

The RMS error for Option 1, profile c), can be seen in figure 6.21a. The RMS-error of the PEDM and EDM$_{lin}$ follows the same trend for all window sizes, with the EDM$_{lin}$ lying between 0.001-0.007 m/s lower than the PEDM. For both the PEDM

and the EDM_{lin} the highest RMS value is reached at the smallest window size of $0.0469 \cdot 0.0469$ m^2. After this the RMS drops and reaches its minimum value of 0.008 m/s and 0.007 m/s for the PEDM and EDM_{lin} respectively, at a window size of $0.0782 \cdot 0.0782$ m^2. Increasing the window size further leads to an increase in the RMS-error for both methods. The CC method run with the same calculation parameters as the PEDM and EDM_{lin} exhibits the same trends with the RMS-error, with increasing inaccuracy with increasing window size.

The RMS error for Option 2, profile c), is depicted in figure 6.21b. The rectangular windows result in overall higher RMS errors, but the results are less sensitive to changing window sizes. Again, the PEDM and EDM_{lin} follows the same trend, starting with high RMS errors for small windows. After the initial decrease of RMS, the RMS error stabilizes, with only small changes as the window size increase. The minimum RMS error is 0.023 m/s for the PEDM, 0.021 m/s for the EDM_{lin} and 0.040 m/s for the CC method. The result of the CC method is less sensitive to the small window sizes, even though it has a higher RMS error, the result is closer to the PEDM and EDM_{lin} than for Option 1. This might be linked to the rectangular windows. For Option 1, the windows where the shape was affected by the boundaries proved to cause large instabilities for the PEDM and EDM, but not for the CC method. Option 2 where all windows are rectangular therefore yields worse results for the PEDM and EDM_{lin} than Option 1. The CC method on the other hand is more accurate for the larger window sizes with Option 2 than with Option 1.

The RMS error of Option 3, profile c), is shown in figure 6.21c. The RMS error of Option 1 and Option 3 are very similar for all three inversion methods. The minimum RMS error is reached for a window size of $0.0782 \cdot 0.0782$ m^2 for all three methods. Here the RMS error is 0.014 m/s and 0.009 m/s for the PEDM and EDM_{lin} respectively, and 0.28 m/s for the CC method.

There are two reason for the high RMS errors that occur at the smallest window size. The first one is that the window is too small to retrieve a clear surface signal of the wave dispersion. With an unclear signal the Doppler shift velocities that are mapped to different depths might be uncertain and deviate from the actual current velocity. Basing a fit on these points with either the PEDM or EDM_{lin} will also be inaccurate, even if the fit itself is accurate. The accuracy of the inversion methods never becomes more accurate than the data they are based on. The second reason is that only small wavelengths are observed. With the PEDM and EDM_{lin} this results in few Doppler shift velocities, and they are mapped to shallow depths. The small windows therefore give few points to base the polynomial and linear fit on, which might result in inaccurate fits. Increasing the window size gives information of a wider range of wavelengths, yielding Doppler shift velocities at greater depth, as of Eq. 3.14. With Doppler shift velocities based on a clear signal that spans over a wide depth-range, the accuracy of the polynomial and linear fit increases, and the RMS error decrease.

However, increasing the window size to achieve a clear signal and a wider depth-range in a region of strong current gradients only works up to a certain

point. Further increase in window size will start to observe regions with fast velocity and regions with slower velocity within the same window. In the fast region, the dispersion will be more prominent than in the slow region. The signal based on the surface observation will be an average of these varying currents, which in turn will yield velocities that doesn't match the current velocity in the centre of the window. This might explain why the calculated velocities of the PEDM and EDM$_{lin}$ are too low in the top part of the window, where the surface PIV reveals a strong decrease of current velocity. However, the surface velocities of the PEDM and EDM$_{lin}$ are constantly lower than the surface PIV for the large window sizes, even in the lower region where the surface PIV experiences minor current gradients. This trend occurred for the other flow profiles a)-d) as well. for The reason for this underperformance of the PEDM and EDM$_{lin}$ for large window sizes are not known. Because the PEDM and EDM is calculated all the way up to the surface, this underperformance can not be linked to the effective depth as the CC method could.

The current derived with the CC method defines the Ux and Uy velocities to go in the same x-and y-directions that define the surface. The PEDM and EDM, on the other hand, is implemented such that the direction of the dominant velocity is defined to be the Ux velocity, independent of the defined x- and y-direction of the surface. The Uy velocity is defined to be perpendicular to Ux. The pump driving the flow in the laboratory is driving the flow in the x-direction, but local variations to the current direction could arise due to the partial blockage or when the water exits the pump. This would cause the velocities derived with the PEDM and EDM$_{lin}$ to deviate both from the CC Method velocities and the PIV surface profile. The direction of Ux in relation to the x-direction of the surface is calculated with the parameter ϕ. The deviation between Ux and the x-direction was found to be no more than 3 degrees for all flow profiles and at all locations of the flow. This is value was deemed small enough to assume that the velocities of the PEDM and EDM$_{lin}$ was derived in the same direction as the CC method and the surface PIV.

6.5 Computational time

The computational time for a single window of the depth uniform CC method and the PEDM and EDM$_{lin}$ can be seen in Figure 6.22. For the CC methods the increase in computational time is linear with increasing window size, whereas the increase in computational time for the PEDM and EDM$_{lin}$method is largest for the smaller windows before flattening out for the larger ones. While the computational time of the CC method experiences an insignificantly increase whith the window size, the computational time of the PEDM and EDM$_{lin}$ increases drastically. It is important to note that the EDM$_{lin}$ is computed as a part of the PEDM, so the graph for the computational time of PEDM and EDM$_{lin}$ is not the combined time of two separate methods, but the final computational time of the PEDM.

Increasing the window size leads to two important factors that affects the inversion methods: A larger surface area needs to be analysed in the algorithm and waves of

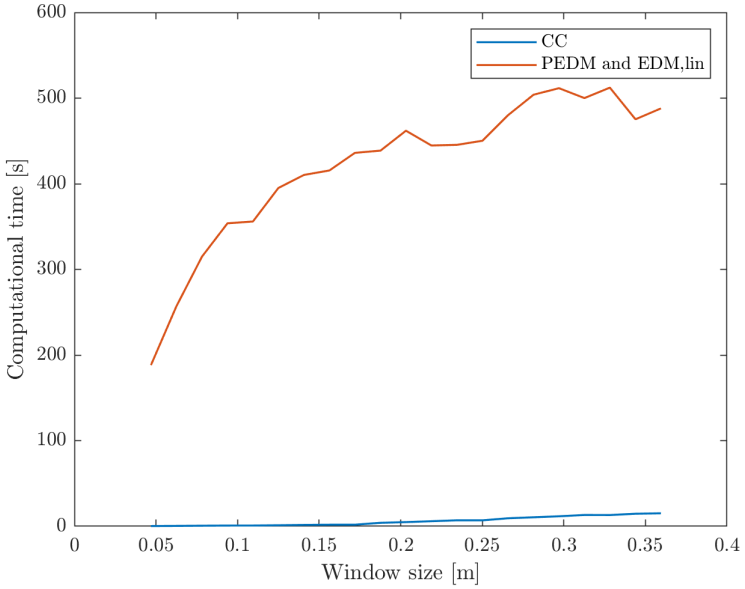

Figure 6.22: Computational time of a single window for the CC algorithm and the PEDM and EDM$_{lin}$for profile a).

larger wavelengths can be observed.

Regarding the CC method, the larger surface area is more important than the observance of larger wavelengths.The CC method is interested in retrieving the near-surface current velocity, which through the Stewart and Joy approximation in Eq. 3.11 is shown to be linked to small wavelengths. These wavelengths can be observed even in small areas, as long as the resolution in k-space is large enough. The CC algorithm gives a near-surface velocity that is weighted toward the surface, meaning that the larger wavenumbers is of small consequence. Increasing the window size only increase the computational time slightly as the algorithm needs to analyse a larger area.

With the PEDM and EDM$_{lin}$ method on the other hand, increasing the window size leads to a much larger computational time. This is because these methods go through a range of wavenumbers connected to the current velocity at different depths. The factor of the presence of larger wavelengths in the analysing area becomes important. For small window sizes only small wavenumbers are present, corresponding to velocities close to the surface. This gives a smaller range of wavenumber to go through, resulting in a short computational time and in a lack of depth-data. Increasing the window size gives both a larger surface area to analyse, and a larger range of wavenumbers to analyse, giving data of the current velocity at greater depths. In figure 6.25a this can be observed. For the smallest window sizes only the top 3.5 mm under the surface is analysed, while for the largest window size one gets information about the depth down to 13 mm. This dependency of large wavenumbers and depth explains why the computational time of the PEDM and EDM$_{lin}$ method increase much more with increasing window size than the CC method.

Due to the lack of large wavelenghts, the maximum effective depth of all four flow profiles is between 12 and 14 mm. Looking at Figure 6.25a, this depth is reached for windows of approximately $0.2 \cdot 0.2$ m^2, and increasing the window size further does not result in larger effective depths. Comparing this with Figure 6.22 the window size of $0.2 \cdot 0.2$ m^2 is where the increase in computational time for the PEDM and EDM$_{lin}$ method starts to flatten out. An explanation for this can be that increasing the window size further from 0.2 m does not give a larger range of wavenumbers to analyse as the upper wavelength limit of λ_{max}=0.2 m is reached. The increase in computational time from window sizes up from this size might solely be caused by the increased size of the surface area that needs to be analysed. This avoids the increase in computational time caused by a larger wavenumber-vector caused by a larger span of wavelengths. If there was more of the longer waves lengths present, the increase in computational time for the PEDM and EDM$_{lin}$ method could be expected to be more constant with increasing window sizes.

The larger gap in computational time between the inversion methods will lead to drastically different computational cost for the three optimization options. The computational time for the CC method is low, and a grid-refinement by adding more windows in certain areas to increase accuracy and resolution can be done with little consequence to the computational cost. The depth dependent methods on the other hand will have increasingly high computational time which will be highly dependent on the numbers of windows involved in the refinement. The computational time for the CC method and the PEDM and EDM$_{lin}$ for option 1, 2 and 3 can be seen in Figure 6.23 and 6.24 respectively.

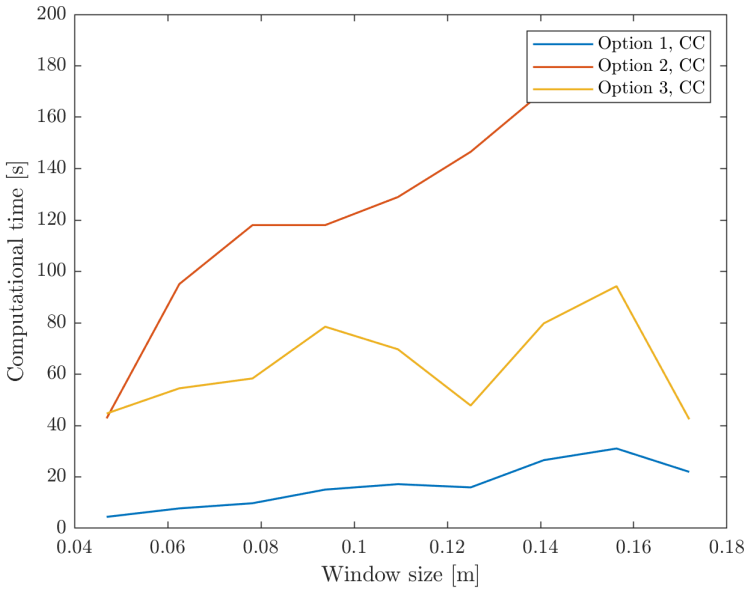

Figure 6.23: The computational time for Option 1-3 for the CC method.

The computational time of Option 1 for the CC method shows much the same trend as the computational time for a single window with a slight increase of the slope as the window size increase, with the longest computational time being just

above 20 seconds. A more surprising element is the large difference in computational time between Option 2 and Option 3, which covers approximately the same area. Option 2 analyses the whole length of the domain in long rectangular windows, while Option 3 analyses the same area but in smaller squares that are later averaged row for row along the x-direction. Starting out with the same computational time for the smallest window size, Option 2 soon requires more than double the amount of time than Option 3. The reason Option 2 requires so much more computational power is not known, but a possible explanation might be that Copter Currents is not designed to handle non-square areas. The rectangular window leads to different resolution between k_x and k_y in the k_x, k_y ω-space, which might cause unforeseen complications or problems in the algorithm.

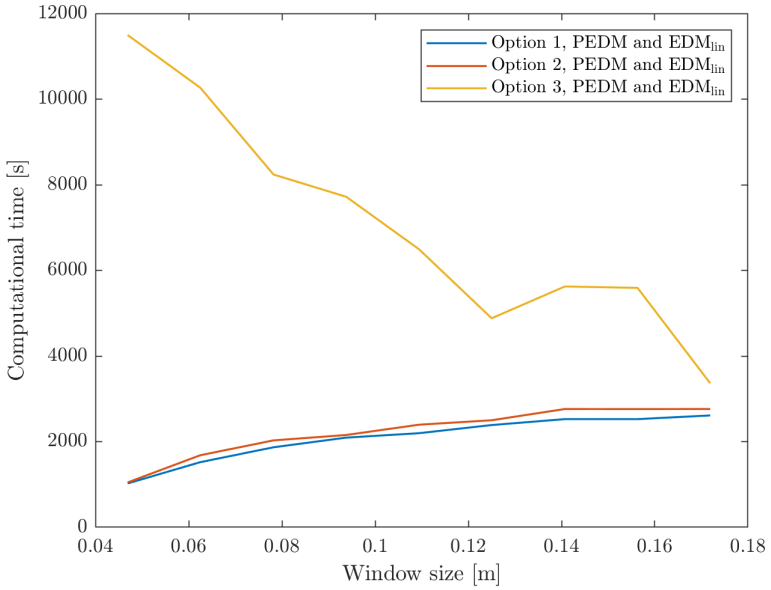

Figure 6.24: The computational time for Option 1-3 for the PEDM method.

The unsteadiness of the computational time for Option 3 for the largest window sizes in figure 6.23 is due to the change of number of windows fitted in the x-direction. Whilst the number of windows in the y-direction is constantly 47 for all window sizes, the number of columns there is room for in the x-direction decrease with increasing window size. In order to maintain a square and constant shape of the windows, some window sizes leave a small gap at the far left of the domain. This is the reason for the dip in the computational time for the window size of 0.1250 m. For the previous window size four columns were analysed, covering almost the whole the length in x-direction, but for 0.1250 m there were only room for three rows of square windows. A fourth column would have lost its square shape, and to avoid the effects of non-square windows described previously, the far right side of the domain was left un-analysed. The size of this un-analysed area decrease as the window size increase further, as can be observed as increasing computational time. The time increases up to the point where there is only space for two whole columns which is for the window size of $0.1719 \cdot 0.1719$ m^2, where the computational time decreases again.

The decreasing number of columns fitted in the x-direction of the domain as the window size decreases is also the reason that the computational time of Option 3 for the PEDM decreases with increasing window size, but here this trend is much more prominent. While increasing the number of windows is unproblematic in regards of computational time for the CC method, this approach for increasing the resolution of the current profile gives high computational cost for the PEDM method. The window size of $0.0469 \cdot 0.0469$ m^2 used in the PEDM has 10 columns to average over, and the computational time is 11469 seconds, or 3.18 hours. The computational time for the same number and size of windows for the CC method is 54 seconds.

Option 1 and 2 for the PEDM is also time consuming, but much less so than Option 3. Both options increase their computational time with window size, with a minimum computational time of 1000 s for the smallest windows and increasing up to 2760 s for Option 2 and up to 2530 s for Option 1. Comparing the RMS errors of Option 1-3 of the PEDM and EDM$_{lin}$ with the computational time, Option 1 stands out as the most reasonable alternative. Here good accuracy is achieved with minimal computational cost.

Based on the computational time the CC method is much less demanding and sensitive to the number of window sizes. This makes it possible to adjust the shape, the size and the number of windows in order to find the option that is best suited to find the current in a given area. Without problems the window size can be decreased and the number of windows increased, or the number of windows can be increased by overlapping the windows in either x- or y-direction while keeping the size constant in certain areas without leading to too high an increase of the computational cost. This makes both Option 1, 2 and 3 viable options for the CC method.

6.6 Depth profile, PEDM and EDM$_{lin}$

This section will present the results of the depth-analysis of the PEDM and EDM$_{lin}$. First the depth-range as a function of window size is discussed. Then the depth-profiles derived with the PEDM and EDM$_{lin}$ are compared with the profile measured by PIV.

6.6.1 Depth range

The depth-range as a function of window size for profile a)-d) is depicted in figure 6.25. For all four profiles the depth decrease almost linearly as the window size goes from its minimum and up to approximately 0.2 m. This is as expected as the increased window size allows for observations of gradually larger waves to be analyzed. The larger wavelengths corresponds to smaller wavenumbers, as of Eq. 3.2 and these decreasing wavenumber-values leads to larger maximum effective depth, as calculated in Eq. 3.14. The maximum effective depth is -11.4 mm for profile a), -12.0 mm for profile b) and -14.7 mm for profile c) and d) which

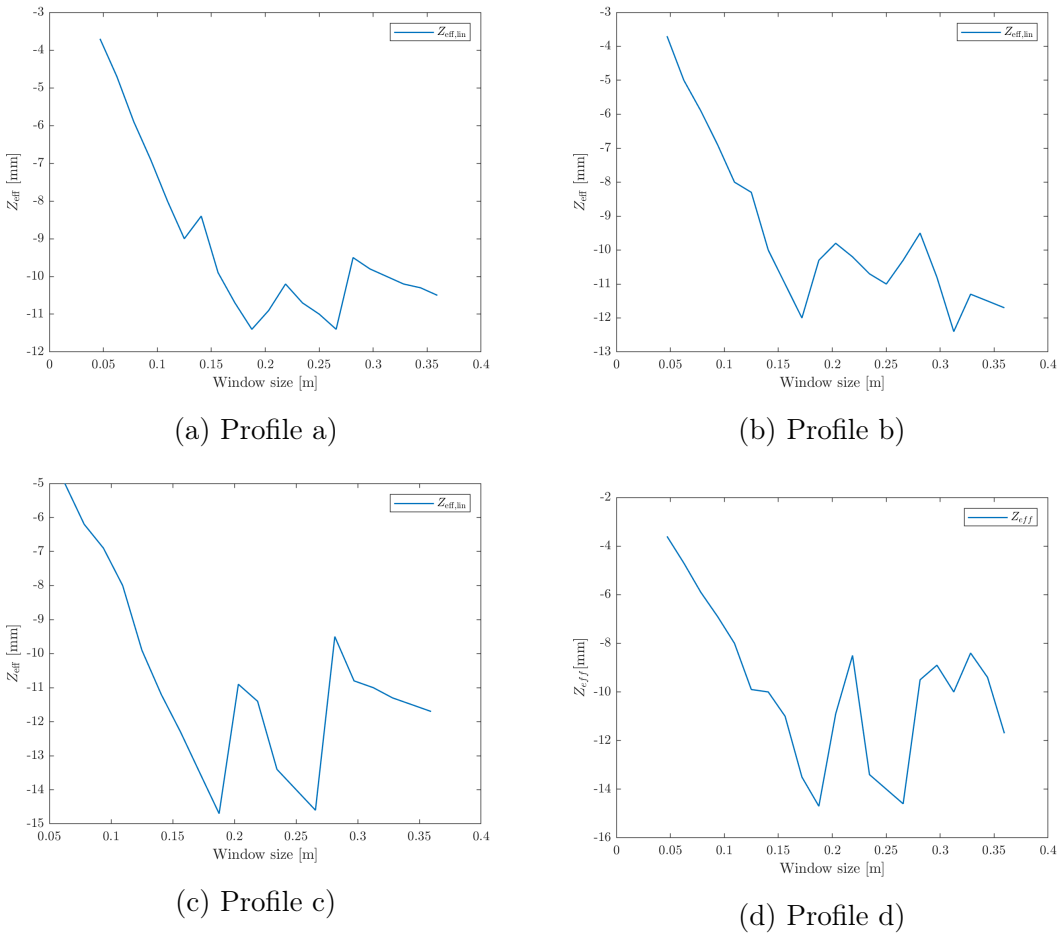

(a) Profile a)

(b) Profile b)

(c) Profile c)

(d) Profile d)

Figure 6.25: Change of the maximum effective depth as the window size increases.

corresponds to wavelengths between 0.14 m and 0.18 m.

Instead of a continued linear decrease of Z_{eff} for further increase in window size, the maximum effective depth varies from window sizes of 0.2 m and up. This suggests that the maximum present wavelength is already reached and observed and increasing the window size further does not result in larger effective depths. That the maximum depth is found at wavelengths between 0.14 m to 0.18 m corresponds to the findings in section 5.2.1 that defined the upper wavelength limit of 0.2 m is reasonable, allowing all present wavelengths to be observed.

The dependence on the presence of varying wavelengths can be a limiting factor for the depth-resolution of depth-resolving inversion methods such as the PEDM and EDM$_{lin}$. With small spatial windows the methods require short wavelengths such that the wave dispersion is observable within the area. The short wavelengths leads to very limited information about the depth profile, with few Doppler shift velocities and a shallow maximum depth, as can be seen in figure 6.26a. As discussed in section 5.2.1, the minimum depth it is possible to retrieve mapped Doppler shift velocities from lies between -2.5 and -3 mm, giving points for the curve fit over a depth range of 1 mm in figure 6.26a. The curve is extrapolated from -2.5 mm and up to the surface at z=0 mm.

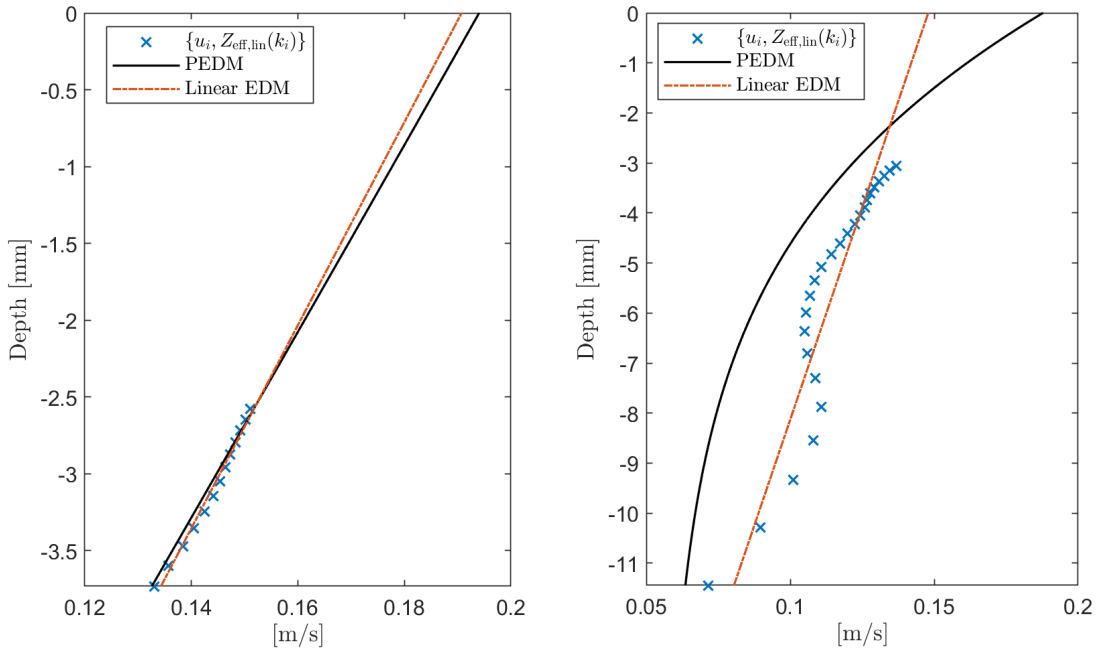

(a) Minimum depth

(b) Maximum depth

Figure 6.26: Depth profile for minimum and maximum depth for profile a).

With large spatial windows the depth-dependent inversion methods requires waves of varying lengths, to allow for Doppler shift velocities evenly over the depth. With only short waves present increasing the window size will not lead to a better resolved depth profile. Similarly, with only large wavelengths presents there will be no information about the current profile near the surface. At the largest observable depth the range of mapped Doppler shift velocities is larger, giving more points for the curve fit, as can be seen in figure 6.26b. This indicates a good distribution of wavelengths in the input data.

The offset between the mapped Doppler shift velocities and the polynomial curve of the PEDM method can be observed in both a) and b) in figure 6.26. This is the difference of n! due to the assumption of the functional form of the current profile. The EDM_{lin} method that is based on the assumption of a linear current profile is fitted to the Doppler shift velocities, while the PEDM is scaled by 1/n! to account for the difference between the assumed shape of the current profile and the actual current profile, causing the gap between the line of the PEDM and the mapped Doppler shift velocities. In 6.26a the Doppler shift velocities is almost linear, and in this linear case the result of the PEDM and EDM_{lin} is almost equal. In 6.26b the Doppler shift velocities are curved with depth, causing a larger difference between the PEDM and EDM_{lin}. The difference between the Doppler shift velocities and the PEDM curve increase with depth, as seen in figure 6.26b. This is because the difference of n! between the actual current profile and the curve derived by linear assumption increases with depth.

6.6.2 Depth profile

Looking at the upper 9 mm close to the surface in figure 6.12, the PIV measurements are close to linear for almost all window sizes and current profiles. While the PEDM profile is linear for some window sizes, as in figure 6.26a, other are strongly curved with high velocities close to the surface, as in figure 6.26b. In the latter cases, the compliance between the PEDM and the PIV starts to decrease from depths of -4 mm and up to the surface due to the strong curvature of the PEDM profile. As seen in section 5.2.1, -3 mm is the smallest depth it is possible to map Doppler shift velocities at. Increasing the maximum wavenumber above 200 rad/m will not give data points at smaller depths but lead to Doppler shift velocities with increasing velocities converging towards a depth of -3mm. In the cases of strongly curved PEDM-profiles the maximum wavenumber might be set too high, causing these converging Doppler shift velocities, and causing the PEDM close to the surface to yield too high velocities compared to the PIV. On the other hand, the results from the surface velocity of the PEDM for in the previous sections have shown a good compliance with the surface PIV. Comparing the surface velocity from the surface PIV and the PIV at position 1 and 2 in Table 6.3, shows that the surface velocity of the PIV measurements at the surface and the surface PIV matches with ± 2 cm/s for all profiles except for profile b). For profile b) the surface PIV is 8 cm/s and 7 cm/s faster than the PIV at position 1 and 2 respectively. This might be linked to the large gap between the surface PIV and the surface velocity profiles derived by the CC and the EDM_{lin} for profile b) in section. 6.4.

Table 6.3: Surface velocity at PIV(z=0) and surface PIV at pos. 1 and pos. 2

Profile	PIV_{pos1} [m/s]	surf.PIV_{pos1} [m/s]	PIV_{pos2} [m/s]	surf.PIV_{pos2} [m/s]
Profile a)	0.0775	0.0963	0.1141	0.1153
Profile b)	0.1236	0.2065	0.1493	0.2168
Profile c)	0.1629	0.1810	0.1922	0.1874
Profile d)	0.1946	0.1915	0.2250	0.2146

6.6.3 RMS-error between the derived depth profile and the PIV measurements

The RMS-error between the PIV profile and the derived depth profile of the PEDM and the EDM_{lin} can be calculated in the same way as for the surface profile, using Eq. 6.1. The depth-dependence of the streamwise velocity, $Ux(z)$ and the PIV(z) are used, summing up over the depth range rather than in the spanwise direction.

To decrease the curvature of the PEDM profile that appears at large window sizes, the maximum wavenumber of k_{max}=200 rad/m was reduced. The reduction in maximum wavenumber decreased the curvature of the PEDM profile for the larger windows. The improvement is measured in percentage of decrease in the RMS-error, and the improvement-rate between the PIV and the PEDM was best for the largest window sizes. Figure 6.27 shows how the decrease from of k_{max}=200 rad/m to of k_{max}=125 rad/m changes the shape of the curve for profile a) for the

window size of $0.1407 \cdot 0.1407$ m^2. For the smaller windows the curve was already linear, and the improvement in accuracy was smaller. The improvement for the smallest window sizes was also less sensitive to the value of k_{max}, with a similar improvement rate for the three different k-values. As the window size increase the improvement is more sensitive to the wavenumber, and best accuracy is achieved with a maximum wavenumber of 125 rad/m. The improvement rate from calculations run with k_{max}=175 rad/m, 150 rad/m and 125 rad/m can be seen in Table 6.4 and 6.5.

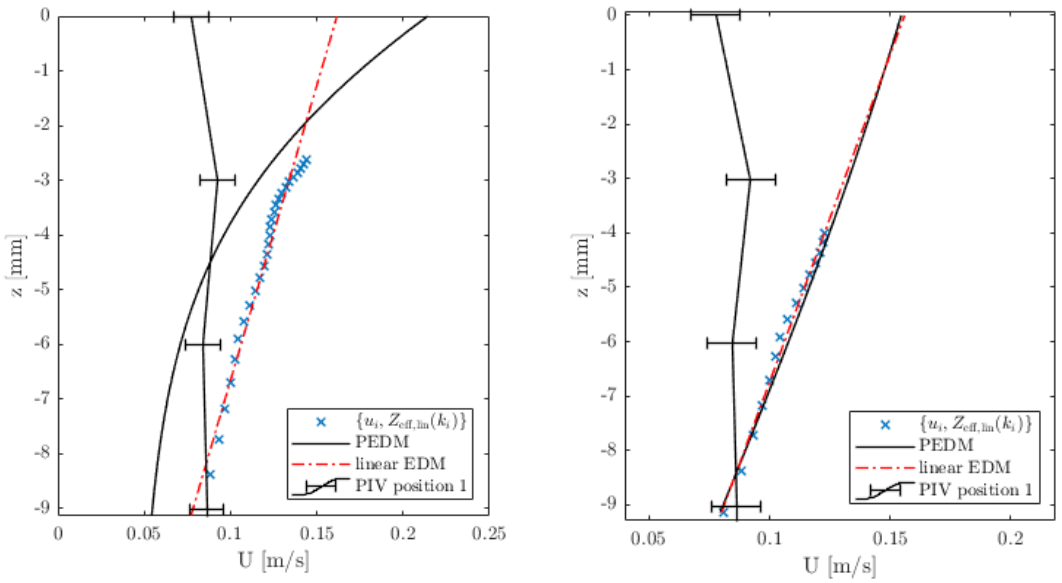

(a) $k_{x,max}$=200 rad/m

(b) $k_{x,max}$=125 rad/m

Figure 6.27: Change of curvature for the fitted PEDM line for a window size of $0.1407 \cdot 0.1407$ m^2, profile a), by decreasing the maximum wavenumber from 200 rad/m to 125 rad/m.

The decrease in maximum wavenumber lead to a larger RMS-error for the EDM$_{lin}$ at position 1 for profile a). This was unique for profile a), and for the other profiles reducing the wavenumber usually lead to smaller variations of the RMS error, such as the ones observed at position 2 in Table 6.5. For the smallest windows the reduced k-value often led to larger RMS-errors, but for the larger windows it lead to lower RMS-errors.

The RMS-error between the PIV and depth profile for profile a) for $k_{x,max}$=200 rad/m can be viewed in figure 6.28a and for $k_{x,max}$=125 rad/m in figure 6.28b. In figure 6.28a the RMS-error can be seen to decrease from the minimum window size and up to a window size of 0.0782 m for both the PEDM and the EDM$_{lin}$, and the two methods yields close to equal results. After this point, the RMS-error of the EDM$_{lin}$ continues to decrease steadily at both position 1 and 2 reaching a minimum RMS at maximum window size, whereas the RMS-error of the PEDM becomes larger. For the PEDM the RMS-error is biggest at position 2, reaching a maximum at 0.87 m/s at a window size of 0.1250 m. Comparing the RMS-error

Table 6.4: Percentage of improved RMS-error of the depth profile for different values of k_{max} for increasing window sizes at position 1, profile a).

Decrease in RMS error [%]							
Window size [m]		0.0625	0.0782	0.0938	0.1094	0.1250	0.1407
k_{max}	Method						
175	PEDM	4.95	-2.51	22.00	1.17	28.15	24.05
175	EDM_{lin}	-33.55	-47.26	-28.47	-32.06	-28.38	-26.49
150	PEDM	4.25	-13.97	20.73	5.37	30.45	37.99
150	EDM_{lin}	-35.78	-66.58	-33.79	-25.65	-26.46	-21.86
125	PEDM	5.21	-45.54	25.57	19.26	35.12	37.10
125	EDM_{lin}	-44.47	-84.06	-50.93	-26.11	-20.87	-23.25

Table 6.5: Percentage of improved RMS-error of the depth profile for different values of k_{max} for increasing window sizes at position 2, profile a).

Decrease in RMS error [%]							
Window size [m]		0.0625	0.0782	0.0938	0.1094	0.1250	0.1407
k_{max}	Method						
175	PEDM	-3.45	-1.13	20.30	32.85	42.67	-1.41
175	EDM_{lin}	-4.87	3.54	14.86	12.452	14.00	4.55
150	PEDM	-7.50	-0.54	54.15	27.86	57.59	33.16
150	EDM_{lin}	-15.03	-15.70	24.83	23.58	20.19	13.46
125	PEDM	18.66	14.48	65.59	46.19	52.88	64.94
125	EDM_{lin}	-32.07	-43.48	5.78	26.97	30.66	17.78

with the velocity profiles, the profiles corresponding to the region where the RMS decreased for the smallest window sizes are close to linear for the PEDM method. For the smallest window sizes the Doppler shift velocities are close to linear, resulting in a current profile that is also linear for the PEDM. As the window size increases, the profile of the PEDM loses its linear shape, as can be seen in figure 6.26, and when this happens, the RMS-error increases. The EDM_{lin} fit that is always linear proves a better match with the PIV from this point on. As the window size is increased Doppler shift velocities at greater depths are included along a linear line, giving the EDM_{lin} method an increasingly better match with the PIV.

In figure 6.28b the maximum wavenumber is decreased down to $k_{x,max}$=125 rad/m, and the RMS-error of both the PEDM and the EDM_{lin} can be seen to decrease with increasing window size, the PEDM and EDM_{lin} following the same trend. The RMS-error for the PEDM at position decrease steeply for the first part before it flattens out at a window size of 0.0938 m, continuing to very gradually decrease up to the largest window size. The RMS-error of the PEDM at position 2 decrease linearly from 0.064 m/s down to 0.021 m/s at a window size of 0.0938 m. From this point the RMS-error increase slightly before ending up at 0.03 m/s for the largest window size. The EDM_{lin} at position 2 follows roughly the same trend, decreasing before flatting out at the end, but with slightly higher RMS-error. This RMS-error is more in line with the theory, that predicts a better depth-resolution

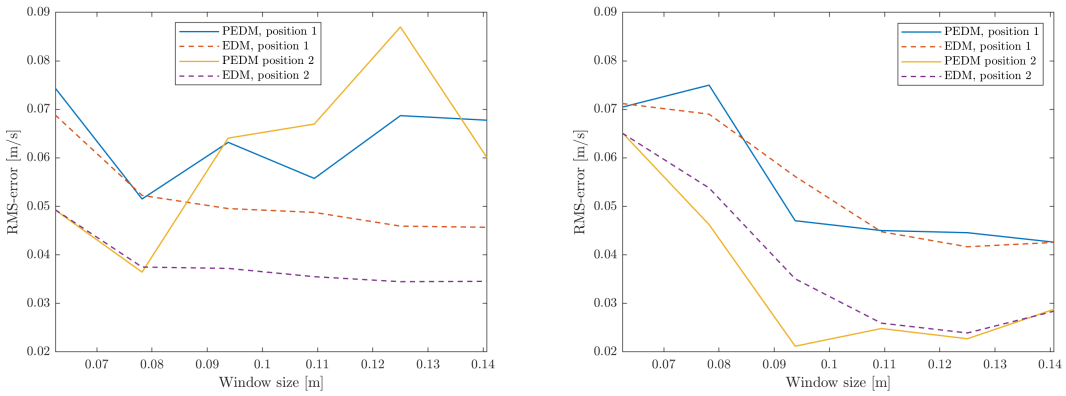

(a) $k_{x,max}$=200 rad/m (b) $k_{x,max}$=125 rad /m

Figure 6.28: RMS error for the current depth profile from the PEDM and EDM$_{lin}$ with maximum wavenumber of 200 rad/m and 125 rad/m, profile a).

that is proportional with the window size.

That the EDM$_{lin}$ and PEDM yielded similar results in terms of accuracy for this reduced wavenumber can be explained by figure 6.27b. The mapped Doppler shifts velocities are close to linear due to reduced value of k, which results in the polynomial fit of the PEDM to also be linear. In the case of a linear current profile, the EDM$_{lin}$ and PEDM will yield similar results, and the offset on n! between the PEDM and the EDM$_{lin}$ when the profile is not linear, as can be observed in figure 6.27a, disappears. Although the EDM$_{lin}$ offered good accuracy for both k-values, the reduction in k down to 125 rad/m improved the fit, as the linear curve became steeper and better matched with the PIV profile when the top Doppler shift velocities was removed.

For both the velocities derived with $k_{x,max}$=200 rad/m and $k_{x,max}$=125 rad/m the RMS-error is highest at position 1. This can be linked position 1 being behind the partially blocked part of the current, resulting in an area with larger current gradients than position 2. The window covering position 1 will therefore be based on an average of the current that increases in the y-direction within the window, whereas the PIV is only based on data from a single place in the x-direction that is not affected by the variations over y. At position 2 the velocity is close to constant within the window, with small to no variations with y, resulting in better correspondence between the PIV and the results of the PEDM and EDM$_{lin}$.

The range and spacing used in the wavenumber vector have proved to affect the results negatively in two ways. The first problem is the spacing of the Doppler shift velocities, the second problem is the horizontal convergence of the mapped Doppler shift velocities towards Z$_{eff}$=-3 mm. Due to the inverse relationship between the depth and k, the number of Doppler shift velocities increases closer to the surface, as can be seen in figure 3.3. In combination with the maximum wavenumber being set too high causing the Doppler shift velocities to increase towards Z=-3 mm, this leads to the strong curvature of the PEDM close to the surface. The fit of the polynomial curve is performed based on these points, and

closely spaced Doppler shift velocities weighs the fit of the curve towards this depth.Decreasing the wavenumber range by decreasing the maximum wavenumber, as done above, addresses the second problem, but the increased frequency of mapped Doppler shift velocities between -5 and -3 mm means that the polynomial fit still is weighted towards the surface.

The curvature of the PEDM might also be caused by overfitting. This is a phenomenon that occurs when the order of the performed fit is too high compared to the order of the data, causing the method to fit to noise. In figure 6.27a the Doppler shifts velocities are located along a nearly linear line up to -4 mm depth, with no outliers or variation, which is a strong indication that this is the actual shape of the current profile. Even though the data is close to linear, the few points at the top that deviates from the linear curve causes the PEDM to look for a non-linear fit. Overfitting can be avoided by implementing measures in the algorithm that makes sure the order of the fit is not higher than the order of the data.

6.7 Wavenumber sensitivity

The CC method has proven to be less sensitive to the available range of wavenumbers than the PEDM and EDM$_{lin}$. The CC method performed without problems both for the upper wavelenght limit of 0.8 m used in section 6.2 and the limit of 0.2 m used in section 6.4. The underperformance of the CC method was proved to be caused by the strong vertical shear, not wavenumber sensitivity. As seen in section 6.3 the derived velocities seems to be weighted towards the effective depth defined by the dominant wavelength, but method is less sensitive to the upper and lower wavelength limits. The vertical shear, in combination with an inversion method that assumed a uniform profile, resulted in the bulk velocity.

The PEDM on the other hand showed a strong dependency on the wavelength range, both for the surface velocity and for the depth velocity. Because the surface velocity derived with the EDM and PEDM is based on a fit of Doppler shift velocities mapped at varying depths, the methods requires wavenumbers over a wide range, also for calculations of the surface velocity. The upper wavelength limit of λ_{max}=0.08 m that were deemed reasonable for the CC method and used in the calculations of the surface velocity in section 6.2 limited the depth-range of the PEDM method, and λ_{max} needed to be changed to 0.2 m for the calculations of the surface profile in section 6.4. The lower wavelengths, corresponding to high wavenumbers affected the resulting surface velocity to an even larger extent, as can be seen in figures 5.3, 6.27 and Table 6.4, where the high wavenumbers result in increasing Doppler shift velocities for the PEDM. Although the upper wavenumber limit of $k_{x,max}$=200 rad/m was deemed reasonable when calculating the surface velocity, when comparing the PEDM depth-profile with the PIV in section 6.6 it was discovered that reducing the upper wavenumber down to 125 led to a $\sim$ 25-60% improvement of the RMS-error for certain window sizes.

The EDM$_{lin}$ proved less sensitive to the wavenumber range than the PEDM, due

to the linear fit to the Doppler shift velocities, but the accuracy of the EDM_{lin} compared to the PIV still improved for most of the flow profiles when the maximum wavenumber was decreased.

6.8 Horizontal and vertical resolution

The RMS errors for the surface velocities in figure 6.10 was shown to increasing with the window size whereas the RMS error for the depth-dependent velocities in figure 6.21 decreased with the window size. To find the balance between horizontal and vertical resolution the RMS errors of the horizontal and vertical profiles must be evaluated together. The region where the RMS error of both methods meet will yield the window size where both the horizontal and vertical resolution is balanced. This will be a trade-off point, where neither the optimal horizontal or vertical window size is used. Instead it will offer a window size that can resolve the velocities in both x-, y- and z- direction with similar accuracy.

In section 6.2 and section 6.4 the surface velocity for all three inversion methods appeared to be most accurate for window sizes between 0.06 m and 0.08 m. This trend was not always picked up by the RMS error used to evaluate the accuracy due to undercalculations and unsteady border values, but it was clearly visible by observation of the surface profiles for all four flow profile a)-d). Windows smaller than 0.06 m this did not succeed in an accurate surface velocity due to the windows being too small to extract a clear surface signal of the wave dispersion. For larger windows the accuracy also decreased, partially due to large current gradients within each window which reduced the horizontal resolution. While the window shape in Option 2 resulted in a higher resolution of k_x in the frequency-wavenumber than Option 1 and 3, none of the three inversion methods managed to utilize this increased resolution into accurate current profiles, and Option 2 was deemed the worst of the options of window placement. Option 1 and Option 3 yielded similar results for the PEDM and EDM_{lin} method, while Option 3 yielded best results for the CC method.

For the depth-profile derived with the PEDM and EDM_{lin} in section 6.6, figure 6.21, the RMS error decreased with increasing window sizes. For both the PEDM and EDM_{lin} the decrease was largest for the smallest window sizes and flattened out as the window size increased. This indicates that the largest windows yields the best vertical resolution, but that the gain in increasing the windows is largest for the smallest windows. The RMS error is highest at position 1 because this is an area with large current gradients. An interesting point to note is that the window size that gave the most accurate surface velocity with the PEDM and EDM_{lin} yielded poor accuracy when the full depth was derived. This means that for the small windows the compliance between the PIV and the PEDM was more accurate near the surface. However, when the full depth profile was resolved, these small windows yielded poorer accuracy than the larger windows. This might be caused by the extrapolation down to larger depth for the smallest windows that was applied in the investigation of the depth-accuracy in section 6.6. Here there the Doppler points was located close to the surface, and the polynomial was

extrapolated down to -9 mm. Although the Doppler shift velocities might indicate the shape of the current profile at this depth, the shape of the current profile might change further down, and this change will not be taken into account when the curve fit is extrapolated. In the investigation of the surface velocity in section 6.4, the velocities were only extrapolated upwards to z=0, not down to -9 mm. In this case the match between the surface PIV and the surface velocity of the PEDM was best for relatively small window sizes. Increasing of the window size in this section resulted in a fit based on greater depths, but it yielded lower accuracy of the surface velocity.

The conflicting need for small windows to achieve horizontal resolution and large windows to achieve vertical resolution can be seen in figure 6.29 for the EDM$_{lin}$, figure 6.30 for PEDM and figure 6.31 for the CC method. Here the RMS errors for the surface profile and the vertical profile is plotted together for profile c). Of the different window placements only Option 1 and Option 3 is included, as these were the options that best captured the surface profiles.

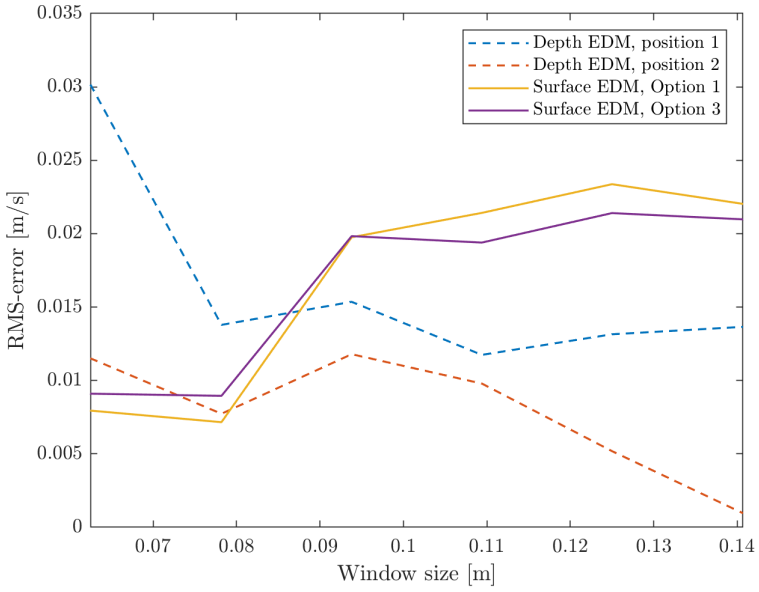

Figure 6.29: The RMS errors of the depth profiles at position 1 and 2 and the surface profiles for the EDM derived with Option 1 and 3, profile c).

The opposite trends of the RMS error for horizontal and vertical resolution is most prominent for the EDM$_{lin}$. At the minimum window size in figure 6.29 the RMS error from the surface profile is at its lowest and the RMS error of the depth profile is at its highest. Choosing a window size in this range will offer the best possible horizontal resolution and the worst depth-resolution. Because the decrease of the depth-RMS is largest for the smallest window sizes, a small increase in window size will result in a large improvement of the vertical resolution. The decrease of the depth-RMS flattens out from window sizes of 0.08 m and up. Here an increase in window size will only lead to minor improvements of the vertical resolution. In this region the RMS errors of the surface and the depth intersect. This is the region that balances the horizontal and vertical resolution, and choosing windows of this

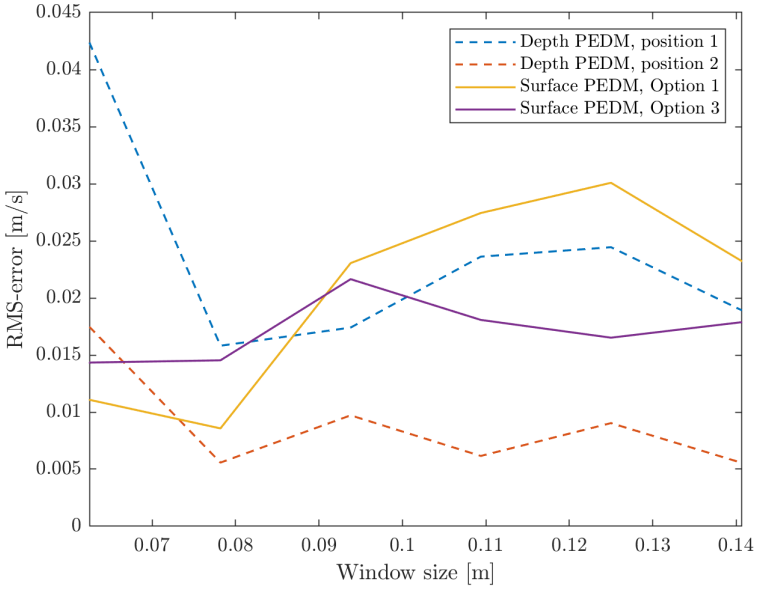

Figure 6.30: The RMS errors of the depth profiles at position 1 and 2 and the surface profiles for the PEDM derived with Option 1 and 3, profile c).

size will yield surface profiles and depth profiles of equal accuracy.

The depth-RMS error of the PEDM for profile c) deviates from profile a), b) and d) in that the decrease in RMS error stops at the window size of 0.08 m, rather than continuing to decrease as for profile a) in figure 6.27b. The depth-RMS error reaches its lowest value at windows of 0.08 m. After this point, the depth-RMS error shows minor variations at position 2 and is unstable for position 1. The surface-RMS error is close to constant up to windows of 0.08 m, and in this case the optimum balance between horizontal and vertical resolution coincides with the lowest RMS error for both the surface- and depth-profile.

In figure 6.31 the RMS error of the depth EDM_{lin} and PEDM at position 2 and the RMS error of the surface profile with Option 1 and 3 from CC is presented. The CC method is less sensitive to increase in window size, resulting in a close to constant value of the RMS error up to windows of 0.011 m. Because of this, the best balance between horizontal and vertical resolution is not found at the intersection between the depth- and surface-RMS at window size 0.07 m. It is possible to increase the window size to reduce the depth-RMS without increasing the surface-RMS. For window sizes between 0.08 m and 0.11 m both the horizontal and vertical resolution is optimized.

The minimum window size for inferring a surface profile is 0.0469 m, and 0.0625 m for the depth profile. Neither the horizontal nor the vertical current profiles are successfully inferred for their smallest windows. In these cases, both a poor surface signal and a small available range of wavenumbers limits the usability of all three inversion methods. For the medium sized windows, the resolution of both the surface profile and the depth profile is high for all three inversion methods. Based on the RMS errors of the horizontal and vertical current profiles, it is possible to

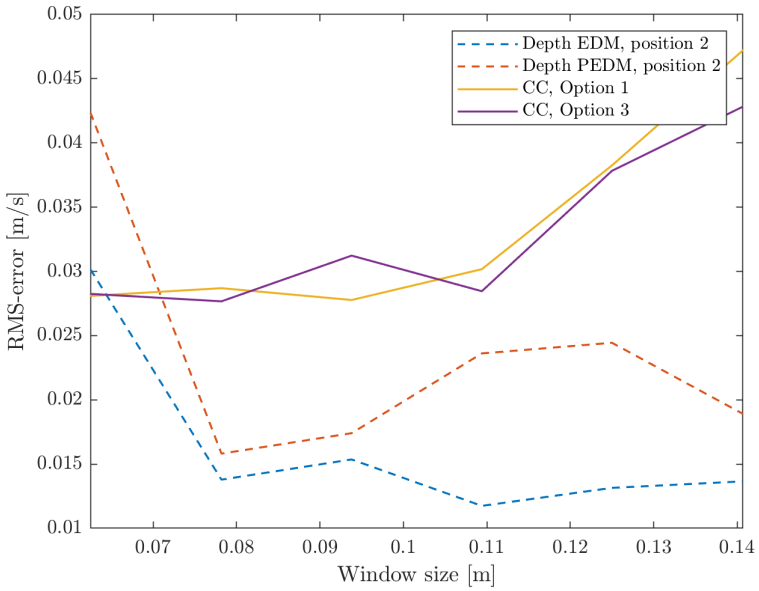

Figure 6.31: The RMS error of the depth profiles of PEDM and EDM$_{lin}$ at position 2 and the RMS error of the surface profile derived with the CC method for Option 1 and 3, profile c)

achieve a good balance between these, and the best balance is found for windows of medium size, between 0.08 m -0.1 m for all three inversion methods.

There is no universal optimum window size for maintaining horizontal and vertical resolution. The optimum window size is dependent on local parameters such as wavelengths, current velocities, current gradients etc. Comparing the optimal window size identified for this data set with the dominant wavelengths in Table 6.1, it looks like the balance is reached for window sizes that are just large enough to observe the dominant wavelength of $\sim$ 6-8 cm. Setting the window size such that the main part of the wavelengths are measured will ensure a good resolution of the $\omega - k$ space where the dispersion relation is visible, which provides a good basis both for the horizontal and the depth resolution.

An alternative approach to the different demands for window size for the horizontal and vertical resolution is to operate with two sets of window sizes in the same region, where the surface velocity is derived from small windows and the depth velocity is derived with larger windows.

6.9 Error sources and limitations

This section will present and discuss possible error sources in the experiment. There are several possible sources of error, linked to the retrieving of the experimental data, the PIV and to the tools used in the data analysis.

6.9.1 Systematic error

A reoccurring result from all three inversion methods was the underperformance of the surface velocities, pointing in the direction of a systematic error linked to the solver algorithms. The underperformance of the CC method was linked to the assumption of a uniform current profile, but no good explanation was found for the underperformance of the PEMD and EDM_{lin}that took place for large window sizes.

6.9.2 Signal strength

Another source of error is the occasional high levels of noise in the signal. This was especially prominent when profile c) was combined rectangular windows in Option 2. With no clear peak in the SNR density map, the uncertainties related to the validity of the results increased. As discussed in section 6.4.2, a good fit based on inaccurate data will yield incorrect results. Several measures were implemented into Copter Currents to avoid errors linked to poor measurements, and in most cases, these were sufficient to avoid these situations.

6.9.3 PIV

The lack of compliance between the PIV measurements of the depth-profile and the retrieved Doppler shift velocities presented in section 6.6 indicates that the uncertainty of the PIV is greater than expected. The Doppler shifts mapped to depth form a linear line with no outliers, indicating a clear and consistent signal of the current velocity at these depths. However, the PIV does not match up with these points. A short investigation of the image processing of the PIV measurements revealed a sensitivity to the area of the laser light sheet. The edges of the light sheet are darker and less suited to image processing, as the particles becomes too dark to track. This applies both to the sides and to the top. During the image processing the dark regions are cropped out manually. A small change in the cropping limits turned out to affect the derived PIV velocities. This was change especially prominent close to the surface, which is the region where the PEDM and PIV was compared in section 6.6. The discontinuity between the surface PIV and the PIV at the surface in Table 6.3 is larger than the expected uncertainty of $\pm$ 1 cm/s, which supports the indicators that there is an error linked to the PIV.

6.9.4 Limitations

Only data from four flow profiles with the same wave-conditions were analysed. To support the results, more flow profiles with different levels of horizontal and vertical shear, varying wavespectrum characteristics and different scales could be analysed to see if they showed the same trends.

One limitation of this project is linked to the small scale. This experiment has been carried out in a small scale laboratory setup, and the identified optimum window sizes are linked to the scale of the lab and the characteristics of the wavespectrum. To make the results applicable on a larger scale, a

non-dimensionalization of the parameters cold have been implemented. However, that horizontal resolution requires closely spaced measuring points and windows of a relatively small size, and that vertical resolution requires a larger size can be assumed to be applicable on all scales.

The CC method has already been used in large-scale field work by Horstmann et al. [2017*b*] and Horstmann et al. [2017*a*], and the EDM is the state-of-the-art method to use in large-scale measurements of currents. The PEDM is the only one of the methods that is not yet tested on a large scale, but it is is assumed that the method is scalable. One of the effects that doesn't scale up is the surface tension σ. The scale of measured wavelengths in this experiment makes the surface tension negligible, and the waves are surface gravity waves. An earlier lab-testing of the PEDM, in the same scale and wave-tank as this experiment, showed that Bond numbers $\rho g\lambda/\sigma \leq \mathcal{O}(1)$ were observed for the shortest wave lengths, indicating that the shortest waves were dominated by surface tension. In these cases, the surface tension coefficient, σ, must be known and taken into account in the dispersion relation in Eq. 3.4. However, the majority of the waves analysed with the PEDM lay within the gravity wave regime, making it physically comparable to a larger scale.

Chapter 7

Conclusion

7.1 Summaries

This work has presented a comparative study of three inversion methods: the newly developed PEDM, the state-of the-art EDM_{lin} and the CC method. The CC method infers the near-surface velocity, whereas the PEDM infers a polynomial and the EDM_{lin} a linear depth-dependent velocity. The inversion methods were applied on flows with strong vertical and horizontal shear, and current velocities were derived from FS-SS surface measurements of the wave dispersion. In order to capture the horizontal current gradients, the surface was divided into smaller sub-sections, referred to as windows, where the dispersion relation was applied separately. Three options exploring different window placements, window numbers and window shapes were examined, and the accuracy of the PEDM, EDM_{lin} and CC method were evaluated by using surface PIV as "truth" measurements. For each option the window sizes were gradually increased and the effect this had on the horizontal resolution was evaluated. The PEDM and EDM_{lin} were used to infer the depth-profiles, and again the effect of gradually increasing the window sizes were explored. PIV measurements of the same flow profiles was used to evaluate the accuracy of the calculated depth-profiles. Based on the results from the horizontal and vertical current analysis, the combination of window parameters that would balance the accuracy of both horizontal and vertical accuracy was identified.

7.2 Goal Evaluation

The accuracy of the methods was measured in terms of the RMS error between calculated current profiles and PIV measurements of the depth profile and the surface profile. Three research questions were answered:

> **Research Question 1** What is an optimal spatial window size and window placement for capturing horizontal surface current gradients?

Three different options for window placement, size and numbers were explored in order to find the alternative that offered the best accuracy of the surface profile.

For all three options the smallest analysable window sizes yielded poor results. This was linked to the poor resolution in k_x space caused by a small spatial area, and the lack of short wavelength in the experimental data set. The best horizontal resolution was achieved for windows of $0.0625 \cdot 0.0625$ m^2 for all three inversion methods.

The PEDM and EDM$_{lin}$ performed well with Option 1, where the surface profile was derived from a single column of windows across the domain, and with Option 3, where the velocities was averaged along the x-direction of the domain.

Option 3 yielded the best result for the CC method, but the CC method underperformed compared to the surface PIV for all options and all window sizes. The reason for the constant underperformance of the CC method was successfully linked to the strong vertical shear in the flow. The CC method assumes a uniform current profile and calculates a velocity that is weighted towards the effective depth. The effective depth is determined by the dominant wavenumber in the flow, where large wavelengths results in a deep effective depth and small wavelengths results in shallow effective depth. When there is strong vertical shear in the flow, the velocity at the effective depth will not reflect the velocity at the surface. Without knowledge of the amount of shear in the flow it is difficult to compensate for this effect.

In terms of computational costs, the CC method was proved to be much less cost demanding than the PEDM and EDM$_{lin}$. This makes the CC more flexible when it comes to increasing the numbers of windows in areas that requires greater spatial resolution, but a limiting factor of this method is that it does not resolve the depth velocity. Option 1 and 3 yielded similar accuracy for the PEDM and EDM$_{lin}$, but due to the high increase in computational cost for Option 3, Option 1 was deemed the best alternative.

Research Question 2 What is an optimal spatial window size for capturing vertical current gradients?

Vertical current gradients were proved to achieve better accuracy for large spatial windows. By increasing the window size, the PEDM and EDM$_{lin}$ methods was able to resolve for the currents at larger depths, due to the inverse relationship between the mapped Doppler shift velocity and the wavenumber. The smallest windows resulted in limited depth information, resulting in profiles that only covered the upper ~ 4 mm of the water column. The attempt at resolving currents at larger depth for small windows by means of extrapolation resulted in large RMS errors due to no information of the local shear in the extrapolated areas. The greatest depths resolved with the PEDM and EDM$_{lin}$ is limited by the largest observable wavelength in the experimental data set, which in this case gave an maximum depth of ~ 14 mm. In this case this corresponded to window sizes of $0.2 \cdot 0.2$ m^2. Increasing the window size further from this point does not contribute to any new data of the depth velocity.

The accuracy of the PEDM and EDM_{lin} was lower in areas covering large horizontal current gradients than in areas of more spatially uniform current. However, even when the velocity changed within the window, the accuracy of the PEDM and EDM_{lin} was increased by increasing the window size.

The PEDM proved to be more sensitive to the range of measured wavenumbers than the EDM_{lin} and CC method. If the calculation parameters used a wavenumber range that exceeded the measured wavenumbers, a converging effect of the mapped Doppler shift velocities appeared near the surface. This caused the polynomial fit to converge as well, resulting in a current profile with large shear close to the surface. The EDM_{lin} was also affected by this, but to a lesser degree due to the linear fit. This effect was most prominent in large windows. Reducing the wavenumber range in the calculation parameters resulted in better accuracy for the large windows, the RMS error of the largest windows decreased by $\sim$ 25-60% for the PEDM.

> **Research Question 3** Is there an optimal window size that will resolve both horizontal and vertical current gradients?

The study has shown that it is possible to resolve both horizontal and vertical current gradients with relatively good accuracy. With the results derived from answering the first and second research question, the region of medium sized windows proved to yield a balance where both the surface and depth resolution could be derived with relatively low RMS errors. The size of the window can be determined from the measured range of wavelengths. The identified optimum window size lies between 0.08 -0.1 m, and comparison with the dominant wavelengths indicates that the optimum window size might be in the region where these wavelength are the largest observable waves in the window. It is also possible to derive information of the surface velocity and depth velocity in the same region with two sets of window sizes, the horizontal surface profile can be derived with smaller size windows, and the depth profile can be derived with a second set of larger windows.

7.3 Contributions

Although this project was performed in a small-scale laboratory settings, the results can be assumed to be applicable no measurements of larger real-field waterbodies such as rivers, along coastlines and the ocean. The findings indicates that a good resolution in areas of horizontal current gradients is achieved by increasing the number of measuring points and decreasing the window size. The vertical resolution achieves best results with large windows, both in terms of accuracy and in terms of the resolved depth. However, when measuring areas with both large horizontal and vertical shear, these conflicting demands can be overcome by choosing a medium window size that observes the dominant wavelength of the surface. This will be a trade-off point where neither the horizontal or vertical resolution is optimized, but the accuracy of both directions are balanced.

7.4 Further work

Further work in this area could include an exploration of the relationship between the surface waves and the PEDM. In order to gain a better understanding of the effects the length and direction of the waves has on the accuracy and depth-range of the PEDM algorithm, the PEDM could be tested with a set of synthetic data that would make it possible to control and adjust the parameters of the waves. Furthermore, this study has proved that increasing the number of measuring points and decreasing the window sizes in areas of large horizontal current gradients can improve the horizontal resolution. When measuring large water surfaces that includes both areas of uniform current velocities and inhomogeneous velocities, this knowledge can be utilize by implementing a measure that automatically adjust the spacing and sizes of the windows in areas with large current gradients. Based on the experimental testing and research that has been done on the PEDM up until this point, the method shows great potential for resolving near-surface shear profiles with high accuracy. With the overall goal of using the PEDM on field measurements, the next step in the process is to apply and test the PEDM on large scale field measurements on currents with strong vertical shear near the surface.

Bibliography

Campana, J., Terrill, E., J. and Paolo, T. [2016], 'The development of an inversion technique to extract vertical current profiles from X-band radar observations', *Journal of Atmospheric and Oceanic Technology* **33**, 2015–2028.

Campana, J., Terrill, E., J. and Paolo, T. [2017], 'A New Inversion Method to Obtain Upper-Ocean Current-Depth Profiles Using X-band Observations of Deep-Water Waves', *Journal of Atmospheric and Oceanic Technology* **34**, 957–970.

Cengel, Y. A. and Cimbala, Y. M. [2010], *Fluid Mechanics, Fundamentals and Applications*, Second edition in SI units edn, McGraw-Hill Education.

Ha, E. C. [1979], 'Remote sensing of ocean surface current and current shear by HF backscatter radar', *Tech. Rep. D415-1* .
URL: *https://apps.dtic.mil/dtic/tr/fulltext/u2/a078834.pdf*

Horstmann, J., Stresser, M. and R., C. [2017*a*], 'Surface Currents Retrieved from Airborne Drone', *OCEANS 2017 Aberdeen* pp. 1–4.

Horstmann, J., Stresser, M. and R., C. [2017*b*], 'Video-Based Estimation of Surface Currents Using a Low-Cost Quadcopter', *Geoscience and remtote sensing letters* **14**(11), 2027–2031.

Kirby, J. T. and Chen, T.-M. [1989], 'Surface waves on vertically sheared flows: approximate dispersion relations', *Journal of Geophysical Research* **96**, 1013—-1027.

Laxague, N., Haus, B., Ortiz.Suslow, D., Smith, C., Novelli, G., Dai, H., Özgökmen, T. and Graber, H. [2017*a*], 'Observations of near-surface currenr shear help describe oceanic oil and plastic transport', *Geophysical Research Letters* **45**(1), 245–249.

Laxague, N., Haus, B., Ortiz.Suslow, D., Smith, C., Novelli, G., Dai, H., Özgökmen, T. and Graber, H. [2017*b*], 'Passive Optical Sensing of the Near-Surface Wind-Driven Current Profile', *Journal of Atmospheric and Oceanic Technology* **34**(5), 1097–1111.

Lund, B., Graber, H. C., Tamura, H., C. C. O. and Varlamov, S. M. [2015], 'A new technique for the retrieval of near-surface vertical current shear from marine X-band radar images', *Journal of Geophysical Research: Oceans* **120**, 8466–8486.

Lund, B. and Haus, B. [2018], 'Near-surface Current Mapping by Shipboard Marine X-band Radar: A Validation ', *Journal of atmospheric and oceanic technology* **35**, 1077–1090.

Moisy, F., Rabaud, M. and Salsac, K. [2009], 'A synthetich Schlieren method for the measurement of the topography of a liquid interface', *Experiments in Fluids* **46**, 1021–1036.

Rubio, A., Mader, J., Mantovano, C., Griffa, A., Novellino, A., Quention, C., Wyatt, L., Schulz-Stellenfleth, J., Horstmann, J., Lorente, P., Zambianchi, E., Hartnett, M., Fernandes, C., Zervakis, V., Gorringe, P., Melet, A. and Puillat, I. [2017], 'HF Radar Activity in Eorupean Costal Seas: Next step toward a Pan-European HF Radaar Network', *Frontiers in Marine Science* **4**(8).

Settles, S. [2001], *Schlieren and Shadowgraph Techniques*, Springer, Berlin, Heidelberg.

Skop, R. A. [1987], 'Approximate Dispersion Relation for Wave-Current Interactions', *Journal of Waterway, Port, Coastal, and Ocean Engineering* **113**, 187–195.

Smeltzer, B. K., Gundersen, I. S. and Ellingsen, S. [2021], 'Calculating sub-surface flow from surface wave measurements', *14th WCCM, ECCOMAS Congress 2020* .

Smeltzer, B. K., Æsøy, E., Ådnøy, A. and Å., E. S. [2019], 'An improved method for determining near-surface currents form wave dispersion measurements', pp. 1–24. **URL:** *https://arxiv.org/abs/1904.11575*

Stewart, R. and Joy, J. [1974], 'HR radio measurements of surface currents', *Deep Sea Research* **21**, 1039–1049.

Teague, C. C., Vescky, J. F. and Hallock, Z. R. [2001], 'A comparison of multifrequency HF radar and ADCP measurements of near-surface currents during COPE-3', *IEEE Journal of Oceanic Engineering* **26**, 399–405.

Wu, T. [1963], 'Dispersion of Water Waves', *Journal of Geophysical Research* **68**(4), 1195–1197.

Young, I. R. and Rosenthal, W. [1985], 'A three-dimensional analysis of marine radar images for the determination of ocean wave directionality and surface currents', *Journal of Geophysical research* **90**, 1049–1059.

Zappa, C., Banner, M., Schultz, H., Corrada-Emmanuel, A., Wolff, L. B. and Yalcin, J. [2008], 'Retrieval of short ocean wave slope using polarimetric imaging', *Measurement Science and Technology* **19**(5), pp 13.

Appendices

.1 Project description

.2 Risk assessment

Master thesis

Ida Seip Gundersen

Autumn 2020

Optimisation of inversion methods for near-surface current measurements in regions with strong horizontal shear

Project description

The project aims to perform an analysis of experimental data to find the optimal spatial window size for computation of current velocity in regions of large current gradients in a spatially inhomogenous shear flow. A suitable measure of optimality for a given data set will be identified. This requires finding the best possible balance between the conflicting needs for accurately capturing horizontal vs vertical velocity gradients; the former requires finer horizontal spatial resolution, i.e., smaller windows, the latter requires resolution of longer wavelengths i.e. larger window size

The data set consists of Free Surface-Synthetic Schlieren measurements performed in the small wave-current laboratory in the Fluid Mechanics building of flows of different horizontal and vertical current profiles"

The following three inversion methods for calculating the current velocity will be compared and contrasted: the Copter Currents method which assumes a uniform depth-profile of the current velocity, and the Effective Depth Method and Polynomial Effective Depth Method which both gives a depth-dependent current velocity. The error statistics of the methods will be analysed using Particle Image Velocimetry as truth measurements.

The full list of tasks is ambitious within the allotted time frame, and any unforeseen delays might necessitate a reduction of scope within those mentioned, to be agreed upon with supervisors and clearly described and motivated in the thesis text.

Supervisor: Simen Andreas Ådnøy Ellingsen

Co-supervisor: Benjamin K. Smeltzer

NTNU HSE	Hazardous activity identification process	Prepared by	Number	Date	
		HSE section	HMSRV2601E	09.01.2013	
		Approved by		Replaces	
		The Rector		01.12.2006	

Unit: *Department of Energy and Process Engineering* **Date: 11.02.2021**

Line manager: Therese Løvås

Participants in the identification process (including their function)**:**

Short description of the main activity/main process: Master project for student *Ida Seip Gundersen*.

Project title: *Optimisation of inversion methods for near-surface current measurements in regions with strong horizontal shear*

Is the project work purely theoretical? (YES/NO): NO *Answer "YES" implies that supervisor is assured that no activities requiring risk assessment are involved in the work. If YES, briefly describe the activities below. The risk assessment form need not be filled out.*

Signatures: *Responsible supervisor: Simen Ellingsen* *Student: Ida Seip Gundersen*

ID nr.	Activity/process	Responsible person	Existing documentation	Existing safety measures	Laws, regulations etc.	Comment
1	PIV measurements	Ida Seip Gundersen				
2	Wave-tank measurements	Ida Seip Gundersen				

NTNU	Risk assessment	Prepared by	Number	Date
		HSE section	HMSRV2603E	04.02.2011
		Approved by		Replaces
HSE/KS		The Rector		01.12.2006

Unit: *(Department)* **Date:**

Line manager:

Participants in the identification process (including their function)**:**

Short description of the main activity/main process: Master project for student *Ida Seip Gundersen*.

Project title: *Optimisation of inversion methods for near-surface current measurements in regions with strong horizontal shear*

Signatures: *Responsible supervisor:* *Simen Ellingsen* *Student: Ida Seip Gundersen*

Activity from the identification process form	**Potential undesirable incident/strain**	**Likelihood:**	**Consequence:**			**Risk Value (human)**	**Comments/status Suggested measures**
		Likelihood (1-5)	Human (A-E)	Environment (A-E)	Economy/ material (A-E)		
1	Microplastic contamination	1	A	A	A	A1	
2	Water damage	1	A	A	A	A1	

Likelihood, e.g.:
1. Minimal

Consequence, e.g.:
A. Safe

Risk value (each one to be estimated separately):
Human = Likelihood x Human Consequence

2. *Low*
3. *Medium*
4. *High*
5. *Very high*

B. *Relatively safe*
C. *Dangerous*
D. *Critical*
E. *Very critical*

Environmental = Likelihood x Environmental consequence
Financial/material = Likelihood x Consequence for Economy/materiel

Potential undesirable incident/strain

Identify possible incidents and conditions that may lead to situations that pose a hazard to people, the environment and any materiel/equipment involved.

Criteria for the assessment of likelihood and consequence in relation to fieldwork

Each activity is assessed according to a worst-case scenario. Likelihood and consequence are to be assessed separately for each potential undesirable incident. Before starting on the quantification, the participants should agree what they understand by the assessment criteria:

Likelihood

Minimal 1	Low 2	Medium 3	High 4	Very high 5
Once every 50 years or less	Once every 10 years or less	Once a year or less	Once a month or less	Once a week

Consequence

Grading	Human	Environment	Financial/material
E Very critical	May produce fatality/ies	Very prolonged, non-reversible damage	Shutdown of work >1 year.
D Critical	Permanent injury, may produce serious serious health damage/sickness	Prolonged damage. Long recovery time.	Shutdown of work 0.5-1 year.
C Dangerous	Serious personal injury	Minor damage. Long recovery time	Shutdown of work < 1 month
B Relatively safe	Injury that requires medical treatment	Minor damage. Short recovery time	Shutdown of work < 1week
A Safe	Injury that requires first aid	Insignificant damage. Short recovery time	Shutdown of work < 1day

The unit makes its own decision as to whether opting to fill in or not consequences for economy/materiel, for example if the unit is going to use particularly valuable equipment. It is up to the individual unit to choose the assessment criteria for this column.

Risk = Likelihood x Consequence

Please calculate the risk value for “Human”, “Environment” and, if chosen, “Economy/materiel”, separately.

About the column ”Comments/status, suggested preventative and corrective measures”:
Measures can impact on both likelihood and consequences. Prioritise measures that can prevent the incident from occurring; in other words, likelihood-reducing measures are to be prioritised above greater emergency preparedness, i.e. consequence-reducing measures.

MATRIX FOR RISK ASSESSMENTS at NTNU

CONSEQUENCE						
	Extremely serious	E1	E2	E3	E4	E5
	Serious	D1	D2	D3	D4	D5
	Moderate	C1	C2	C3	C4	C5
	Minor	B1	B2	B3	B4	B5
	Not significant	A1	A2	A3	A4	A5
		Very low	Low	Medium	High	Very high
		LIKELIHOOD				

Principle for acceptance criteria. Explanation of the colours used in the risk matrix.

Colour		Description
Red		Unacceptable risk. Measures must be taken to reduce the risk.
Yellow		Assessment range. Measures must be considered.
Green		Acceptable risk Measures can be considered based on other considerations.